THEORETICAL & EXPERIMENTAL ANALYSIS OF PEC REDOX FLOW BATTERY KINETICS

Richard FAASSE

Student ID 4378830

Master Thesis
Applied Physics
MECS group, Applied Science
TU DELFT
17/09/2019

Supervisors:
dr. Dowon BAE,
assoc. prof. dr. Wilson A. SMITH,

Comittee members:
prof. Bernard DAM,
prof. Fokko MULDER,
dr. David A. VERMAAS,

Content

Nomenclature

Greek Symbols

α	Symmetry factor in the butler-volmer equation
$\alpha(\lambda)$	Absorption spectrum as a function of wavelength
λ	Photon-wavelength
λ_g	Photon-wavelength corresponding to the bandgap energy (E_g)
ν	Electromagnetic frequency
Ω_{sh}	Shunt resistance
Ω_s	Series resistance
ϕ_b	Schottky barrier height
ρ	Density
σ	Stefan Boltzmann constant

Latin Symbols

$[c]$	Electrolyte concentration
ΔE^0_{redox}	Difference between the redox potentials (cell voltage) at 50% SOC
A_{ph}	Emission area of photo-absorber relative to the absorbing area
C_O	Concentration of oxidized species
$C_p(z)$	Charge collection probability as function of depth
C_R	Concentration of reduced species
c_v	specific heat
C_{auger}	Auger coefficient
C_{SC}	Capacity of the space-charge region.
d	Electrolyte thickness
E_a	Activation energy, associated with kinetic barriers at the electrode
E_g	Semi-conductor bandgap energy
$E_{dev,loss}$	Device losses, due to series resistances, reflection etc
$E_{redox,ox/red}$	Redox potential of the oxidator/reductor
Eff	PV-efficiency
$G(z)$	Charge generation distribution as function of depth
$h_{x\leftrightarrow y}$	Heat transfer coefficient between component x and y
j_0	Dark saturation current of the photo-diode
j_D	Current density through the diode
$j_{0,bv}$	Exchange current density in the butler-volmer equation
$j_{0,ref}$	Exchange current density at reference temperature
$j_{max,ph}$	Photo-current limit
$j_{mtl,c/a}$	Mass transfer limit of the current density at the cathode/anode
$j_{op,exp}$	Operating current of the SRFB (experimentally determined)
j_{tunnel}	Limiting tunnel-current
k	Boltzmann constant
L	Photo-absorber thickness
m_{eff}	Effective mass
n	Ideality factor, used for photo-voltaic semiconductors

$N(\lambda)$	Incoming photon-density
n_2	Number of electrons involved in a redox reaction
n_3	(Complex) Index of refraction for optical materials
N_D	Semi-conductor donor density
n_i	Intrinsic carrier concentration
P_{in}	Input power due to solar radiation
P_{out}	Output power
q	Charge
$Q_{battery}$	Charge capacity of the RFB
R_x	Reflection coefficient (Fresnel) of material x
T	Photo-absorber temperature
T_x	Optic transmission of material x
V_D	Voltage across the diode
V_{cell}	Cell voltage
V_{oc}	Open circuit voltage
V_{on}	Onset potential
v_{th}	Thermal carrier velocity
W_b	Schottky-barrier width

Abbreviations

(S)RFB	(Solar) redox flow battery
AR	Anti-reflective
B(/F)PA	Back(/Front)side photo-anode
B(/F)PC	Back(/Front)side photo-cathode
CV	Cyclic voltammetry
IV-curve	Current-voltage curve
LSV	Linear scanning voltammetry
MS	Mott Schottky
NHE	Normal Hydrogen Electrode
PEC	Photo-electrochemical
PV	Photovoltaic
SOC	State of charge
STC	Solar to chemical

Physical constants

ϵ_0	Vacuum permittivity
c	Speed of light in a vacuum inertial frame
e	Elementary charge
F	Faraday's constant
h	Planck constant
k	Boltzmann constant
N_A	Avogadro's number
R	Gas constant

Subscripts

abs	Photo-absorber
air	Ambient air
el	Electrolyte
fb	flat-band

Abstract

The transition from stable fossil fuel energy production to intermittent renewable sources poses a huge challenge to our generation. The mismatch between electricity supply and demand will become an increasingly pressing problem, due to the growing share of renewable energy production and the electrification of the automotive industry.

The upcoming field of Solar Redox Flow Batteries (SRFB) proposes a possible solution in the search for feasible energy storage. Integrating a photovoltaic module with a redox flow battery results in a highly reversible storage system, which has both the advantage of flexibility in capacity and charge/discharge power, as well as the direct and efficient coupling to solar energy generation. However, due to its early stage in development, the SRFB has several challenges to overcome, like low charging efficiencies and energy densities. To improve SRFB efficiency, this work provides a performance estimation model, to identify general sensitivities of SRFB efficiency with respect to the loss mechanisms associated with the device, such as (but not limited to) kinetic overpotentials and resistances, to establish device design principles. This model is also extended to simulate realistic environments, using real (daily/seasonally dependent) solar radiation and ambient temperature data. Moreover, a fit tool is realized to identify losses in a specific system, by varying parameters and mimicking experimental linear scan voltammetry data.

Experimentally, several conducting layers are tested for their kinetics and conductivity and impact on device performance. A thin film of platinum is found to result in the best kinetics and lowest resistance. However, carbon-coated electrodes also show promising results and could be a feasible and cheaper alternative to platinum, when applying layer-optimization.

Based on the design principles derived from the modeled and experimental results, a single-junction silicon-based SRFB is developed, based on a ferri-/ferrocyanide electrolyte, coupled with $Cu^{2+/+}$, yielding high solar-to-chemical charging efficiency of 9.4%. This efficiency is close to the simulated efficiency, while multiple other SRFB photo-charging experiments follow modeled trends, validating the model.

Chapter 1

Introduction

1.1 The challenge of the energy transition

One of the most pressing and complex problems of our current generation is the need for an energy transition from fossil fuels to sustainable sources. The severity of climate change and global warming has led to policies aimed towards mitigating it: "The EU is committed to reducing greenhouse gas emissions to 80–95% below 1990 levels by 2050".[1] More recently the Paris agreement prompted all partaking countries to respond to the threat of climate change by "Holding the increase in the global average temperature to well below 2 °C above pre-industrial levels".[2]

Several approaches in tackling this problem include electrochemical CO_2 reduction [3] (recycling CO_2 to produce fuels such as methane) and reducing CO_2 emissions. However, CO_2 reduction faces problems concerning selectivity, as mitigating parasitic hydrogen production is a pressing problem in CO_2 reduction setups. [] Reducing emissions is mostly done by transitioning from fossil fuel energy production to renewable electricity sources, combined with the electrification of energy consumption (e.g. in the automotive industry). In 2017 the contribution from renewable sources to the electricity production in OECD countries totaled 23.7%, of which 26.9% was from solar energy.[4] However, due to the inherent intermittency of solar energy and the daily/seasonal variation of its power production, which does not follow the trend of electricity usage, there is a mismatch between energy supply and demand, as shown in figure 1.1.

Two approaches in mitigating this mismatch can be distinguished. Firstly, efforts are made into smart and dynamic electricity grid management, to shape the demand to fit the supply. [6] The second approach is the storage of energy, using various technologies. Lithium-ion batteries are widely used for energy storage and could be used for large-scale storage, as a possible solution. However, there is no consensus on the resource depletion for these batteries.[7] Although it is not expected lithium availability will obstruct its usage in the booming electric vehicle market, utilization for large-scale storage is questionable. Moreover, thermal runaway makes a Li-Ion system prone to overheating [8], making large-scale storage facilities unsafe.

1.2 Photo-electrochemical energy conversion

One of the other ways to store a surplus of electricity is to produce hydrogen via electrolysis. Various upcoming technologies focus on hydrogen production. The battolyser, for example, is a novel system, which functions as an electrochemical battery until it is fully charged and starts producing hydrogen from thereon [9].

Moreover, efforts have been made to introduce photo-electrochemical water-splitting, in which electrolysis of water is performed in one integrated system, converting incoming solar radiation into hydrogen, using a photo-voltaic module, combined with a photo-electrochemical cell [10, 11].

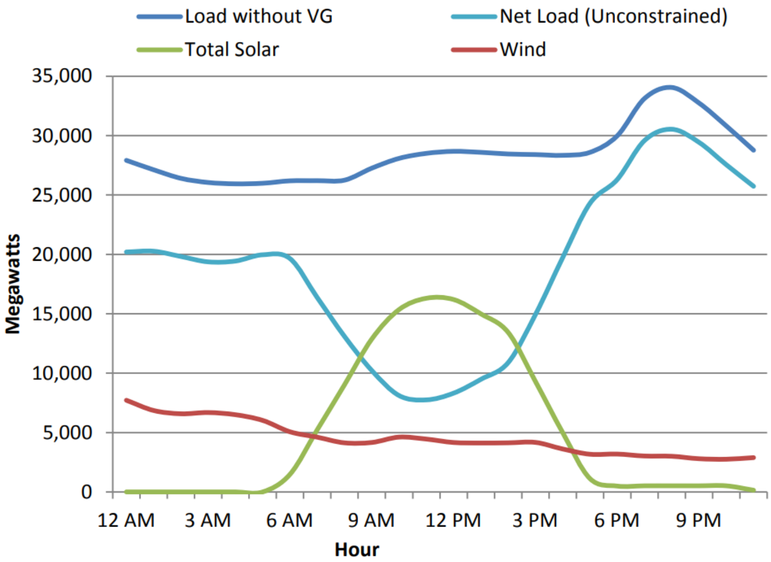

Figure 1.1: The energy supply (wind and solar), as well as the energy demand without variable generation (VG) and the net load on the grid in California [5]. It is seen that the light blue curve of the net load (defined as the demand minus the variable generation), is highly variable, with a steep and problematic increase around 3PM. This net load curve is known as the "duck-curve" due to its distinct shape.

This approach has two major disadvantages, regarding device design. Water splitting requires a theoretical voltage of 1.23V, but due to sluggish kinetics, this extends to 1.7-1.8V in practice.[12] This requires a photo-absorber, which provides a photo-voltage of 1.23V at the very least. The lack of flexibility in photo-absorber optimization and cell voltage, combined with the sluggish reaction kinetics [13] suggest a different approach.

1.3 Fundamentals of a Solar Redox Flow battery

A field that has attracted a significant amount of attention relatively recently, is the field of solar redox flow batteries (SRFB). In short, the photo-electrochemical redox flow battery (schematically displayed in figure 1.2, finds its foundation in two major concepts. The first is the photovoltaic cell, while the second is the electrochemical cell. By analogy, the redox flow battery (RFB) acts as a reservoir of electrons for two different energies. In turn, the photovoltaic cell can be seen as the pump, when it is put into contact with the liquid electrolyte. It is able to drive electrons from the reservoir with lower-energy electrons, to states with higher energy.
In a physical system, this means that the redox flow battery consists of two volumes of electrolytes, with different energy levels for the electrons, which are stored in separate tanks. When an illuminated photo-absorber comes into contact with an electrolyte, it is able to remove electrons from the energetically lower state and transport them via an external circuit, to store them in the higher energy states by means of redox reactions (figure 1.2a). These electrons can release their stored energy later, due to the reversible nature of the reactions (figure 1.2b), thus creating a solar-powered battery, which is able to mitigate (part of the) mismatch between intermittent solar supply and energy demand.

One of the major advantages of RFBs as a storage unit is the decoupling of capacity and power.[15] Since the capacity is simply determined by the volume of the electrolyte (thus, the size of the storage tanks) and the charge/discharge power can be manipulated separately by changing the active area/number of electrodes, the device can be adapted to the specific needs of its various applications.
Moreover, there is a wide variety of suitable redox couples available, necessary to tune the cell voltage to the bandgap of the photo-absorber as well as aligning the bands of the photo-absorber with the energy

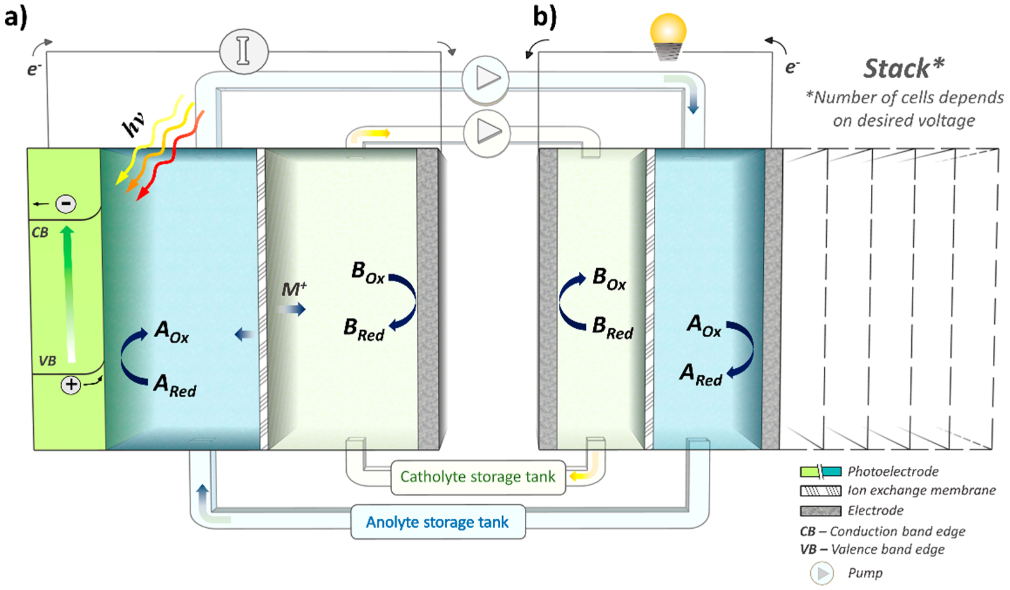

Figure 1.2: Schematic representation of a solar redox flow battery, in which a) and b) depict the charging and discharging part of the battery respectively. The photons in a) (denoted with $h\nu$) are absorbed by the photo-electrode, which in turn drives the redox reactions A and B. In b) it is seen that there is freedom in output voltage and current, by stacking multiple discharge cells. [14]

levels of the redox couples in the electrolytes. This flexibility in cell design gives SRFB an advantage over photo-assisted water splitting, which has a fixed cell voltage of 1.23V. The recent trend of using organic, highly tunable redox couples exploits this variety even further.[16, 17]

1.4 The state of the SRFB field

The first implementation of photo-electrochemical cells as a battery was reported by Hodes et al [18]. After this, several papers on the device were published in the 80s. However, these devices were not commercialized and research stagnated, due to the high costs of efficient photo-absorbers and membranes, used in these works, as concluded by Sharon et al in a review in 1991.[19]

However, since 2016, renewed interest in the SRFB arose, due to developments in the redox-flow-battery field (e.g. organic redox couples) and quite possibly the pressing societal need for electrical storage. The two major parameters in single-junction SRFBs are the thermodynamic potential (the difference in energy between the two active redox couples) and the band-gap of the solar absorber, which is in general proportional to the voltage the PV module is able to provide under illumination.[12] These two parameters need to be properly matched to achieve high efficiencies. In figure 1.3, an overview of single-junction solar-to-chemical (STC) efficiencies is shown, as found in literature, as a function of thermodynamic potential and photo-absorber bandgap energy.

Recently, several high-performance SRFBs were developed using state-of-the-art PV-modules and optimized redox flow batteries, resulting in 14.1 [21] and 10.5% [22] solar-to-electricity efficiencies. These results are significant steps towards viable solar energy storage via SRFBs. However, the triple-junction solar cells used in these works are expensive and complex. To achieve commercialization and avoid the pitfall of the high-cost devices, which caused the stagnation of SRFBs in the 1980s, simplicity, and cost-effectiveness should be prioritized. Therefore this work focuses on SRFBs, consisting of single-junction cells. Moreover, the well established, but expensive catalytic use of platinum is compared to cheaper alternatives, like carbon.

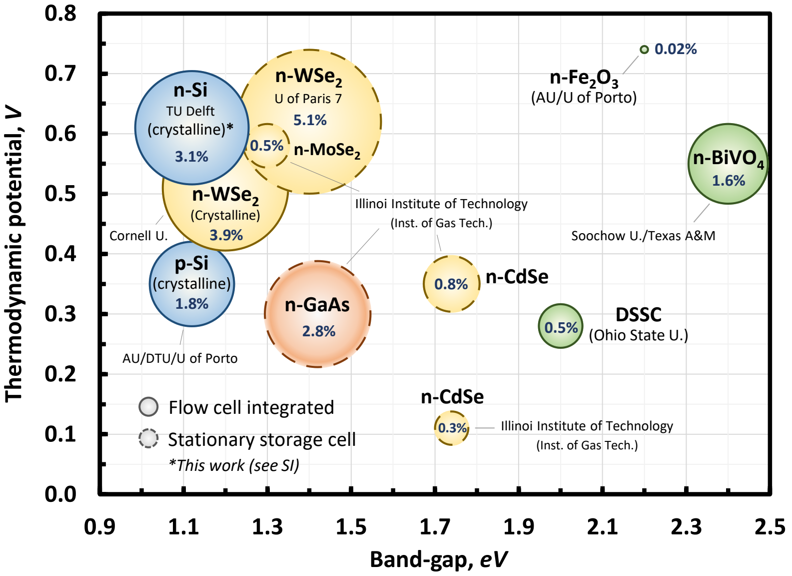

Figure 1.3: Experimental Solar-To-Chemical efficiency of several unbiased single photo-absorber cells is shown with different combinations of the photo-absorber band-gap and thermodynamic potential (defined as the difference between the redox potential of the respective oxidation and reduction couples). For clarity, Si-based materials are colored in blue; chalco-genides in yellow; III–V in orange; and metal-oxides in green. Detailed working conditions and citation information for the references for the chart can be found in the ESI of the original paper published as a part of this work [20]

1.5 Research question and approach

In short, solar redox flow batteries are a promising solution in mitigating the mismatch between renewable energy supply and demand. However, this technology is still at an early stage in its development. Therefore, device optimization and design principles are needed in order to push SRFBs towards feasible implementation. In this work, the single-junction PEC redox flow battery will be assessed both experimentally as well as through mathematical modeling. Through these methods, design principles are derived for optimizing a photo-electrochemical redox flow battery, which in turn are used to test a high-efficiency SRFB.
The approach of this work is as follows:

1. Firstly, a performance estimating model is developed (in python) to create a benchmark for the device's efficiency, depending on the loss mechanisms in the system (e.g. parasitic optical loss, internal resistances, and kinetic barriers) and find the general loss-sensitivity trends.

2. Using the modeled trends, experiments are done on PEC-flow batteries, in which one electrolyte is fixed to be ferri-/ferro-cyanide, to establish the real performance and create the high-efficiency PEC-flow battery, depending on varying redox-couples and conducting layers.

3. Moreover, a fitting tool is developed to relate modeled characteristics to experimental data. This tool varies several parameters, associated with device losses, to identify these losses and validate the model. The modeled loss-sensitivities can then be used to find which loss-reduction would have the most impact.

4. Lastly, the model is extended to include temperature and seasonal dependence, to predict practical SRFB performance (beyond sterile lab conditions). Due to significant modeled temperature-dependence effects and discrepancies between practical and 'lab-based' performance, this work provides motivation for further research in this area.

Using this approach, the following research question is addressed:

Which conducting catalysts, redox couples and design principles result in optimal kinetics of reactions and performance for an iron-based PEC redox flow battery?

1.6 Thesis Outline

In the following chapters, these research questions are addressed. In chapter 2, the background theory, the composition of the model and the experimental methods are discussed. Chapter 3 consists of the experimental and modeling results and the comparison between the two. The discussion of the results with respect to the research question is found in chapter 4 and the conclusions follow in chapter 5, followed by the bibliography and the appendix, consisting of detailed derivations, additional supporting experimental/modeling information, and the python code.

This work includes two original works, one of which has been published and one of which is still under submission:

1. Dowon Bae, Gerrit M. Faasse, Gerasimos Kanellos, and Wilson A. Smith. Unravelling the practical solar charging performance limits of redox flow battery based on the single photon device system. *Sustainable Energy & Fuels*, 3:2399–2408, 2019
2. Dowon Bae, Gerasimos Kanellos, Gerrit M. Faasse, Emil. Drazevic, Anirudh. Venugopal, and Wilson A. Smith. Design principles for efficient photoelectrodes in solar rechargeable redox flow battery applications. *Under submission*

Therefore, part of the result section follows the flow of these articles closely.

Chapter 2

Theory & Experimental Methods

In this chapter, the two concepts of photovoltaics and electrochemical energy conversion (the building blocks of the SRFB) will be explored in depth. After this, they are put together to discuss the complete PEC redox flow battery, with all its possible advantages and challenges. Moreover, the design of a model for performance estimation is discussed with the underlying assumptions, applicability, and limitations. Lastly, the experimental setup and characterization methods used to verify and underpin the modeling results are discussed.

2.1 Photo-voltaics

The component which actually converts incoming solar radiation to electrical power needed to charge the integrated storage system is the photovoltaic cell. In this work, the focus will be on a single junction device, consisting of a semi-conductor pn-junction.

2.1.1 Fundamentals of Photo-voltaics

A semi-conductor is a selective conductor, which has a Fermi level between two bands. The bottom band, also called the valence band, is therefore completely filled, while the top (or conduction) band is completely empty (we are neglecting thermal excitations at the moment). At the bottom band, the electrons are packed, so there is no possibility to move around, making the semi-conductor insulating. There is an energy gap between these two bands, from now on referred to as the bandgap or E_g. When a photon with an energy larger than the bandgap enters this material, it can be absorbed by an electron in the valence band, which gains energy ($E_{ph} = hc/\lambda$) and jumps from the valence band to the conduction band. In figure 2.1, the AM15 solar spectrum is plotted as incoming solar power (W/m^2/nm) versus the respective photon wavelength (nm). The number of photons absorbed, and thus the number of electrons moved from valence to the conduction band, is proportional to the area under the curve. In other words, if all the absorbed photons result in conducting electrons, the maximum photo-current density (A/m^2) produced is given by equation 2.1

$$j_{max,ph} = e \int_0^{\lambda_g} N(\lambda) d\lambda, \tag{2.1}$$

in which e is the elementary charge, λ_g is the photon-wavelength corresponding to the band-gap energy of the photon-absorber and $N(\lambda)$ is the incoming photon density (#/m^2/nm/s). Note that all relevant parameters are scaled by the area of the photo-absorber, to eliminate area-dependence. The view on photon-absorption, sketched here, turns out to be too simplistic, as seen in section 2.1.3.5, but it suffices for the physical understanding of photo-voltaics.

In figure 2.1, the wavelength corresponding to the silicon bandgap of 1.12 eV is shown as the vertical dashed line, which results in the shaded area being available for absorption, resulting in electrons being excited

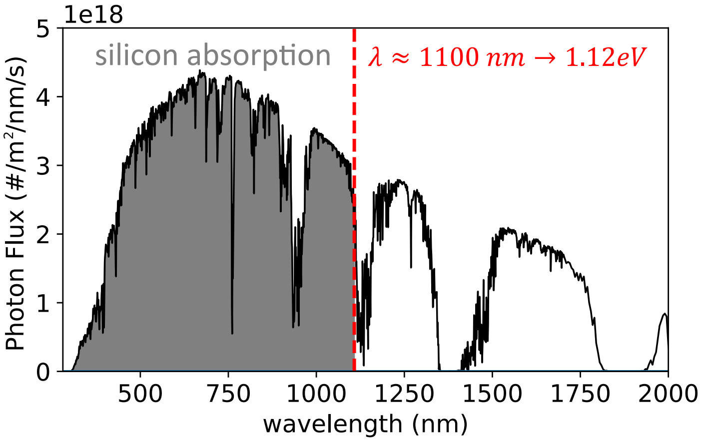

Figure 2.1: Incoming solar flux ($\#/\text{m}^2/\text{nm}$) versus wavelength, plotted for the AM1.5 benchmark spectrum. The dashed line represents the wavelength corresponding to a silicon bandgap of 1.12 eV, such that the absorbed fraction of the incoming spectrum is seen as the grey area under the curve.

into the conduction band. These electrons can freely flow in the empty conduction band and since they have higher energy than before, a voltage difference arises and could be exploited to make the electrons flow around and therefore create electrical power. However, since there is no preferred direction for the electrons and holes to go, the electrons will not create a net current and will stay within the semi-conductor too long, allowing them to recombine, generating a photon. To understand why this does not happen in solar cells, it is necessary to consider its crystalline structure.

For concreteness, let us consider a silicon semi-conductor, which is widely used due to its favorable bandgap (as seen in figure 2.1) and its abundance on earth. Crystalline silicon forms a lattice, in which each silicon atom has 4 valence electrons. When doping this silicon, some atoms in the lattice are replaced by e.g. boron or phosphorus atoms (the dopants), which have five and three valence electrons respectively. Because of this different number of valence electrons, the dopants introduce extra electrons or vacancies, which is why the dopants are called donors and acceptors. respectively. In case of crystalline silicon being doped with donors,

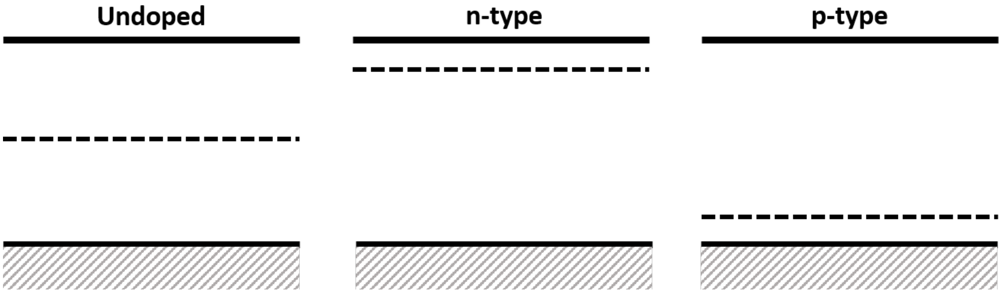

Figure 2.2: Schematic representation of the band structure of undoped, n-type and p-type semi-conductors respectively. The valence band is mostly filled, while the conduction band is largely empty. In the undoped case, the fermi-level, depicted by the dashed line, is situated in the middle of the band-gap. For the n-type and p-type semiconductors, the Fermi-level shifts towards the conduction/valence band respectively.

also called n-type silicon, the Fermi-level shifts towards the conduction band, due to the extra energy levels introduced by the donors. In case of the p-type silicon (doped with acceptors), there are extra energy levels for holes, resulting in a lower fermi-level as seen in figure 2.2. When a p-type and n-type are put into contact, the fermi-levels equilibrate (when there is no external forcing, like illumination). However, due to the doping level, the position of the fermi-level in the bulk has to stay the same relative to the conduction/valence band. To satisfy these two physical principles, a natural phenomenon called band-bending arises. This is depicted in figure 2.3a).

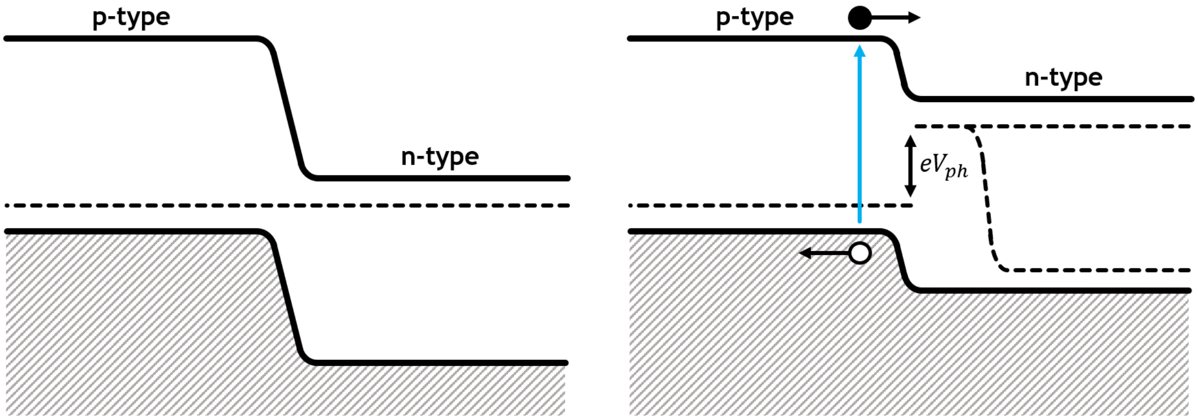

Figure 2.3: Schematic depiction of a pn-junction in the dark (left) and under illumination (right)

This pn-junction results in an electric field close to the contact plane also called the depletion layer. Upon illumination, photons with an energy larger than the bandgap are absorbed, exciting electrons from the valence band into the conduction band, which leaves an empty spot, or 'hole' in the valence band. Due to the internal electric field, these electron-hole pairs are separated, sweeping the negatively charged electrons to the n-type and the positively charged holes towards the p-type silicon.

When analyzing a photovoltaic cell, the current-voltage curve (referred to as IV-curve from hereinafter) is a crucial characteristic. To find the current as a function of the voltage, the cell is considered as an electrical circuit, consisting of the pn-junction, acting as a diode and a current source, caused by photo-absorption as discussed before. The circuit is displayed in figure 2.4b. In the ideal case, the resistances R_{series} and R_{shunt} (which will be discussed in section 2.1.4) are 0 and ∞ respectively.

The current through a diode is found using the diode-equation:

$$j_D = j_0 \cdot \left[\exp\left(\frac{qV_D}{k_b T}\right) - 1 \right] \tag{2.2}$$

in which j_0 is the dark saturation current, V_D is the voltage across the diode, k_b is the Boltzmann constant and T is the diode temperature (naturally equal to the photo-absorber temperature). Analyzing the circuit in figure 2.4b) using Kirchoff's law, results in equation 2.3.

$$j = j_{max,ph} - j_D = j_{max,ph} - j_0 \cdot \left[\exp\left(\frac{qV}{kT}\right) - 1 \right] \tag{2.3}$$

in which the dark saturation current is determined using blackbody emission theory (as found in the book by Martin Green [24]):

$$j_0 = qA_{ph}\frac{2\pi kT}{h^3 c^2} \cdot [E_g^2 + 2kTE_g + 2(kT)^2] \cdot \exp\left(-\frac{E_g}{kT}\right) \tag{2.4}$$

Equations 2.4 and 2.3 result in the IV-curves, displayed in figure 2.4a for both a silicon ($E_g = 1.12$ eV) and a GaP photo-absorber ($E_g = 2.26$ eV).

On the y-axis, the current density is shown, while the x-axis depicts the voltage. Note that again units of current density, as opposed to current, are used, to eliminate the area-dependence of the current, due to the

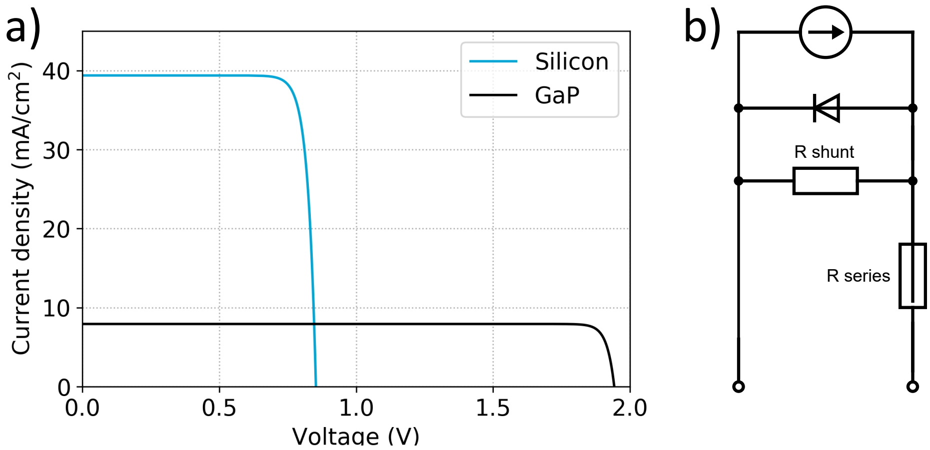

Figure 2.4: The ideal current-voltage characteristics of a silicon and Gallium Phosphide (GaP) photo-absorber in a. Since the bandgap of GaP is larger than silicon, it has a higher photo-voltage, but a lower $j_{max,ph}$, due to lower photo-absorption (as a lower portion of the incoming radiation has an energy larger than the required E_g).

absorbed solar radiation being dependent on the area of the photo-absorber.
The short-circuit current (often estimated to be equal to $j_{max,ph}$) is the current at $V = 0$, while the open-circuit voltage (V_{oc}) is the voltage at $j = 0$, which can be interpreted as the maximum voltage at which the photovoltaic cell can still induce photo-current.

Note that the ideality factor is assumed to be unity throughout this work. However, this is not per se the case when looking at real-life semi-conductors. More insight is needed in the precise influence of the ideality factor on the IV curve of the dry photovoltaics. Just filling in n in the equations gives non-physical results (as seen in the appendix), since it increases the open-circuit voltage, however this is certainly not the case and the precise influence of the phenomenological constant is not found in literature.

2.1.2 Performance interpretation

It is seen in figure 2.4 that a larger bandgap results in a higher open-circuit voltage, but a lower short circuit current (j_{sc}) due to the lower fraction of the solar spectrum which can be absorbed. The performance of a photovoltaic cell is measured in terms of the efficiency, defined as:

$$Eff = \frac{P_{out}}{P_{in}} = \frac{jV}{P_{in}} \tag{2.5}$$

in which the j and V are the current and voltage, found using the IV-curve and P_{in} is the area normalized input power, corresponding to the incoming solar radiation ($\approx$ 90mW/cm^2 in case of the benchmark AM15 spectrum). As seen in figure 2.5, the maximum efficiency depending on the bandgap.
In the next sections, several loss mechanisms will be discussed, which change the characteristic IV-curve and in turn reduce the efficiency.

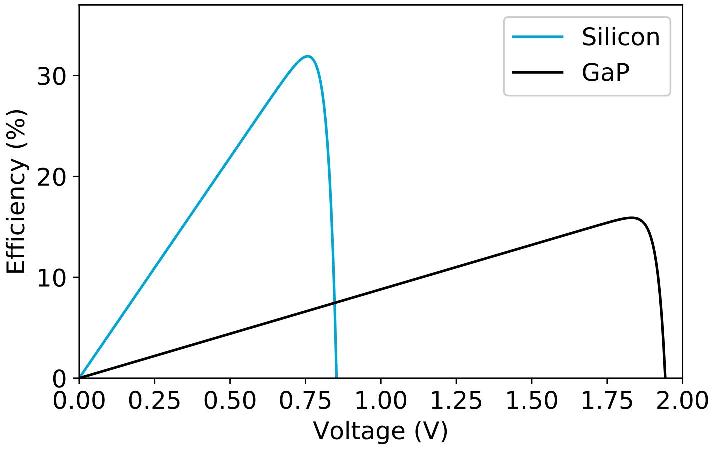

Figure 2.5: The efficiency plotted as a function of voltage for an ideal silicon/GaP semiconductor respectively. It is seen that the maximum efficiency and voltage at which the efficiency is maximum depend on the bandgap of the photo-absorber.

2.1.3 Fundamental limitations

The first fundamental loss mechanism in photovoltaics is recombination, which is the event of an electron and a hole recombining (in this case an electron, photo-excited into the conduction band, somehow ends up in the valence band again). There are several recombination mechanisms, which will be discussed in the following sections. After the discussion on the recombination mechanisms, the concepts of collection probability and charge generation rate and their influence on the maximum photo-current ($j_{max,ph}$) are considered in relation to these recombination mechanisms. Figure 2.6 shows the four recombination mechanisms schematically.

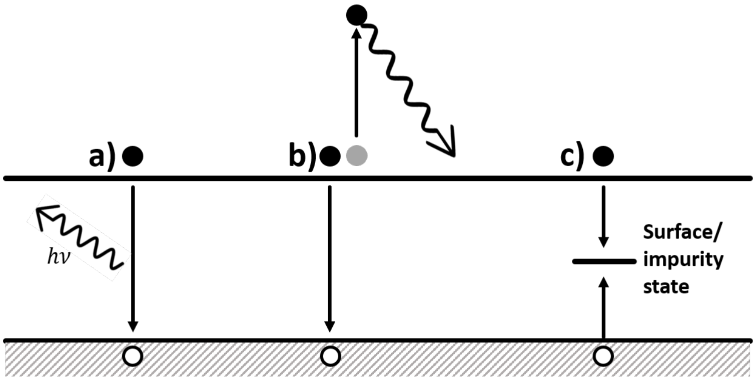

Figure 2.6: Schematic representation of the discussed recombination mechanisms: a) radiative recombination, b) Auger recombination, c) Surface/Shockley-Read-Hall recombination

2.1.3.1 Radiative recombination

The most intuitive mechanism is radiative (or band-to-band) recombination. In this case, an electron from the conduction band falls back into the valence band, and in the process emits a photon with an energy comparable to the band-gap (the opposite process of photon-absorption). However, in indirect bandgap semiconductors (e.g. silicon), which dominate the PV industry this effect is negligible with respect to the other recombination processes, discussed in the following sections. Therefore, the dark saturation current in equation 2.4, based on band-to-band recombination, is a very idealized case and can be seen as the intrinsic lower limit of the recombination rate. Other mechanisms, such as Auger recombination result in a higher intrinsic minimum of the recombination rate [25].

2.1.3.2 Auger Recombination

An electron in the conduction band is also able to transfer its energy to another electron in the conduction band, thereby losing its energy and falling back to the valence band. The electron in the conduction band which received the extra energy loses its energy due to thermal relaxation. Tiedje and Yablonovic derived the following equation for the IV-curve, including this effect[26]:

$$j = j_{max,ph} - j_0 \exp \frac{eV}{k_b T} - eLC_{auger} n_i^3 \exp \frac{3eV}{2k_b T} \tag{2.6}$$

in which C_{auger} is the Auger coefficient, n_i is the intrinsic carrier concentration and L is the photo-absorber thickness.

2.1.3.3 Shockley-Read-Hall recombination

As seen in previous sections, dopants add a donor/acceptor level to the semi-conductor, and in the same way, defects in the crystal lattice add extra levels into the band-structure. If these are situated within the bandgap, they could facilitate recombination. Recombination via these mid-gap states, or 'traps', is discussed statistically by Shockley and Read [27] after Hall found experimentally [28] that the electron lifetime in germanium depends on the impurity concentration. The electrons or holes are trapped in the impurities, via photon emission or thermal relaxation processes.

2.1.3.4 Surface recombination

In the same way defects result in trap states, the surface of a photo-absorber has different properties than the bulk in general, due to the asymmetry in the lattice. Therefore, trap-states could arise at the surface, when having an energy within the bandgap-region and thereby assisting recombination. The extent of this effect is captured in surface recombination velocity, S and manifests itself in the charge collection probability, discussed in the following section.

2.1.3.5 Charge generation and charge collection probability

As seen in previous sections, several recombination mechanisms and their effect on the open-circuit voltage are discussed. However, the maximum current density also needs a more rigorous approach. In this section, the notion of spatially distributed electron-hole generation and charge collection probability are introduced to further increase theoretical accuracy. Since semi-conductor photon-absorption is a statistical process, the charge is not generated uniformly across the depth of an absorber. In general a material with absorption coefficient $\alpha(\lambda)$ has a charge generation distribution as a function of depth (z) as given in equation 2.7:

$$G(z) = \int_0^{\lambda_g} \alpha(\lambda) N(\lambda) e^{-\alpha(\lambda) z} d\lambda \tag{2.7}$$

in which λ is the photon wavelength and $I_0(z)$ is the incoming radiation. Furthermore, the electron-hole pairs generated according to equation 2.7 only contribute to the net photo-current when separated by the pn-junction before recombination. Simply put, the pn-junction needs to be within a charge carrier diffusion length to separate electron-hole pairs effectively. Mathematically, this is described by solving the steady state continuity equation to acquire the depth-dependent charge collection probability $(C_p(z))$[10], which is found in the appendix, equation A.2. $C_p(z)$ and $G(z)$ are plotted in figure 2.7. It is seen that $C_p(z)$ is unity at the pn-junction (since at that location electron-hole pairs are separated immediately) and decreases with increasing distance as the probability of diffusing pairs reaching the junction reduces. Furthermore, surface recombination influences $C_p(z)$, as a higher surface recombination velocity decreases the collection probability at the surface (as shown in figure A.3 in the appendix).

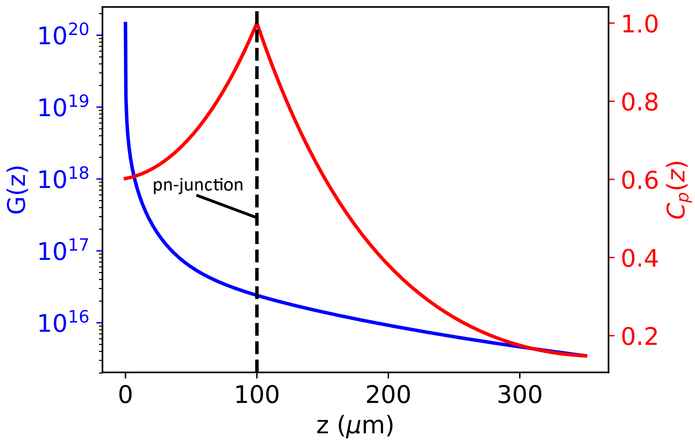

Figure 2.7: Plots of the electron-hole generation rate ($G(z)$) and the charge collection probability ($C_p(z)$) as a function of photo-absorber depth with the pn-junction situated 100 μm from the left surface. The maximum photo-current is proportional to the integral of the product of these two functions. Note that the generation rate is plotted in log-scale, accentuating the steep decline of the function.

The maximum photo-current can be found by integrating the product of the two probabilities, as only the pairs that are generated, as well as collected contribute:

$$j_{max,ph} = q \int_0^L G(z) C_p(z) dz \tag{2.8}$$

To maximize the product of $G(z)C_p(z)$, the pn-junction is placed close to the illumination side in general. Therefore, the placement of the pn-junction in figure 2.7 is not to scale, but it serves the illustrative purpose. Because of to the very high depth-resolution needed, due to the thin n or p layer to maximize $j_{max,ph}$, this method is fairly slow. For large simulations, a more convenient analytic solution, based on the absorption spectrum ($\alpha(\lambda)$) is used:

$$j_{max,ph} = e \int_0^\infty N(\lambda) \cdot (1 - \exp(-\alpha(\lambda)L) d\lambda, \tag{2.9}$$

in which L is the photo-absorber thickness. The absorbance of silicon is calculated using $Abs = (1 - \exp(-\alpha(\lambda)L)$ as seen in equation 2.9).

2.1.4 Series resistance and Shunt paths

Next to the fundamental limitations, the PV-module exhibits losses due to imperfections, resulting in series resistance and shunt paths. They are best understood when depicting the photo-absorber as an electrical circuit, as seen in figure 2.4b. Ideally, the shunt resistance is infinite, allowing no current loss through shunt paths. However, in practice photovoltaic devices do have a finite shunt resistance, allowing for some electrons to take this route and dissipate energy, resulting in loss.

$$j = j_{max,ph} - j_0 \cdot \left[\exp \frac{q(V + j\Omega_s)}{nkT} - 1 \right] - \frac{V + j\Omega_s}{\Omega_{sh}} \tag{2.10}$$

The effects of finite series and shunt resistance are depicted graphically in figure 2.8. Both losses have a significant effect on the output power via a reduced photo-current, as explained in section 2.1.2.

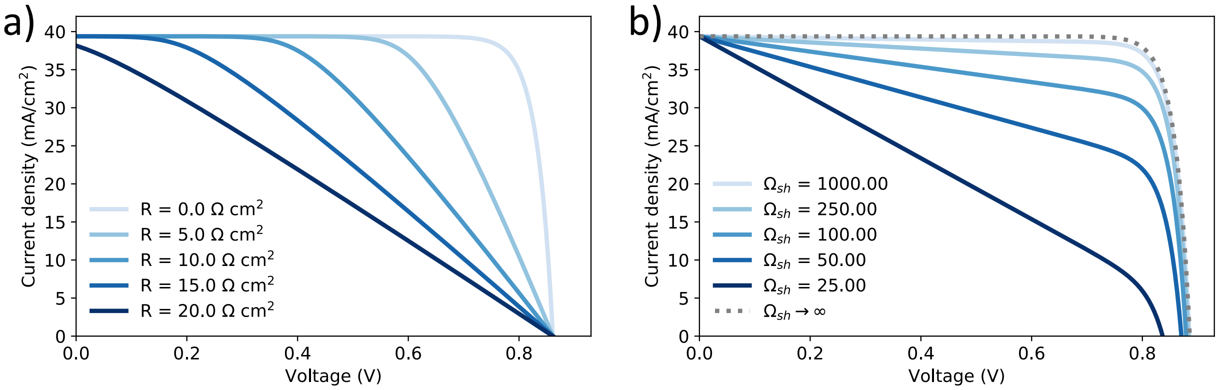

Figure 2.8: IV-curves of a photo-voltaic cell, while varying the series resistance (a) and the shunt resistance (b) respectively. Note that for high shunt-path/series resistance losses, the curves become harder to distinguish.

2.2 The electrochemical cell

In short, the concept of the electrochemical cell is the separation of two redox reactions. Since different ions have different redox-potentials, an energy difference can be realized between electrons in the separated chambers. This means by oxidizing the anolyte (taking electrons out of that solution at an energy of $E = E_{redox,red}$) and reducing the catholyte (placing electrons into that solution at $E = E_{redox,ox}$), the energy of the electrons is increased, creating a voltage difference across the cell. In this example, ferri-/ferrocyanide and $\mathrm{Cu}^{2+/+}$ redox couples are used, resulting in the following reactions

$$[\mathrm{Fe(CN)}_6]^{4-} \xrightleftharpoons[\text{discharging}]{\text{charging}} [\mathrm{Fe(CN)}_6]^{3-} + \mathrm{e}^- \qquad 0.48\mathrm{V\ vs\ NHE} \tag{2.11}$$

$$\mathrm{Cu}^{2+} + \mathrm{e}^- \xrightleftharpoons[\text{discharging}]{\text{charging}} \mathrm{Cu}^{+} \qquad 0.08\mathrm{V\ vs\ NHE} \tag{2.12}$$

Schematically, this is displayed in figure 2.9 for an electrochemical cell with $\mathrm{Fe(CN)}_6^{3/4-}$ as redox couples in the catholyte and $\mathrm{Cu}^{2+/+}$ in the anolyte at 50% state of charge (for a detailed analysis on state of charge effects, see section 2.2.3). In general, a highly conductive supporting electrolyte is added to the reversible couples to minimize electrolyte resistance losses.

As seen in the schematic in figure 2.9, the $\mathrm{Cu}^{2+}/\mathrm{Cu}^{+}$ and $\mathrm{Fe(CN)}_6^{3/4-}$ redox potentials are 0.08V and 0.475V versus NHE. This means, that in an ideal electrochemical cell (neglecting the losses), a voltage supply of $\sim$0.4V is needed to transfer the electrons from the anolyte to the catholyte, increasing their energy. Conversely, discharging the cell (so transferring the electrons from the catholyte to the anolyte) ideally provides a voltage of $\sim$0.4V.

Note that this implies that the fermi-levels of the conductive electrodes equilibrate and align with their respective redox potentials. As found in the book by Bard and Faulkner [29], the effect of this equilibration process on the solution is negligible, as "compared to the total charge that could be transferred to or from ferri- and ferrocyanide in a typical system, only a tiny charge is needed to establish the equilibrium at Pt; consequently, the net chemical effects on the solution are unnoticeable. By this mechanism, the metal adapts to the solution and reflects its composition."

However, kinetic overpotentials (as seen in section 2.2.1) result in a discrepancy between the fermi-level of the electrode and the redox potential of the active species. [29, 30]

The dashed line in the schematic in figure 2.9 represents the selective membrane used. In this work, this is an (an)ion-exchange membrane, but recent developments also show the current scientific interest in the

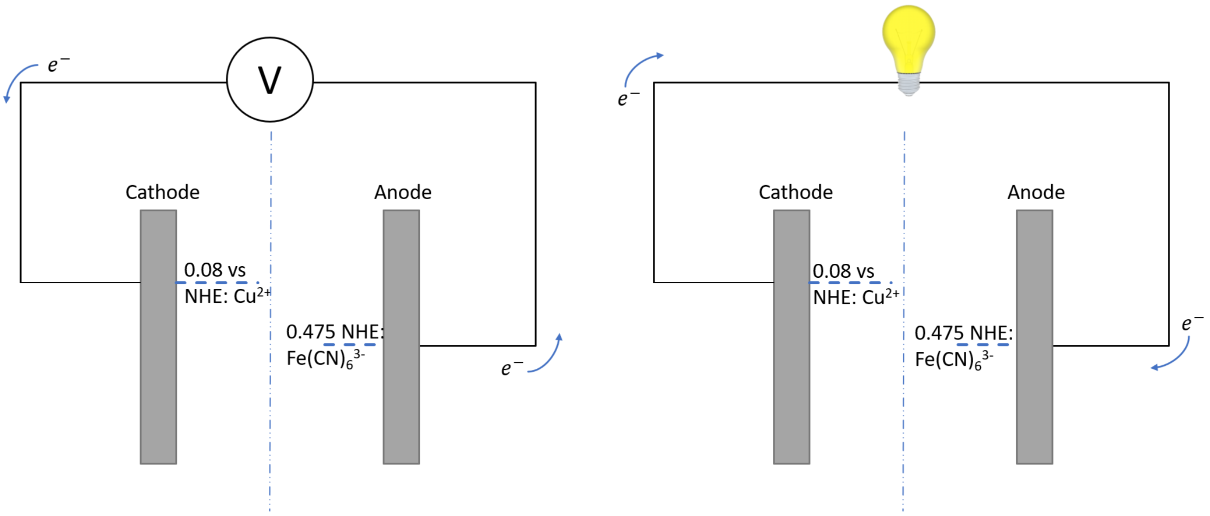

Figure 2.9: Schematic depiction of an electrochemical cell during charging (a), using a bias voltage and discharging (b), generating a current. Note that the redox potentials are determined at 50% SOC, while they change with varying SOC as discussed in section 2.2.3

field of bipolar or microporous membranes for this purpose. The membrane separates the two electrolytes, preventing spontaneous discharging, while still allowing certain charge carriers (e.g. protons or $NH3^+$) to pass through, in order to preserve the charge balance in the system.

In the next sections, several losses and deviations are discussed. First of all, the effects of kinetic overpotentials and mass-transfer limits are discussed as the two main losses associated specifically with the charging and discharging of an electrochemical cell. After this, the effect of a variable state-of-charge (SOC) is discussed and finally, ion-crossover is briefly considered as a mechanism that reduces the cell's capacity.

2.2.1 Kinetic overpotentials

The first imperfection in the electrochemical cell arises due to the reaction kinetics at the surface of the electrodes. In most cases, there is a free energy barrier between the reactant and the product. As derived in [29], this results in the Butler-Volmer equation (equation 2.13), in which mass transfer limitations are neglected for now:

$$j = j_{0,bv}\left[\exp\left(\frac{-\alpha nq(E-E_0)}{k_bT}\right) - \exp\left(\frac{(1-\alpha)nq(E-E_0)}{k_bT}\right)\right] \tag{2.13}$$

in which $j_{0,bv}$ is the exchange current density, α is the transfer coefficient, which accounts for the symmetry of the kinetic overpotential losses, as the kinetics for the oxidation and reduction reaction of the same species are not identical in general. In figure 2.10, the current-voltage curves are shown for varying $j_{0,bv}$ (a) and α (b).
Furthermore, since $j_{0,bv}$ is a function of temperature, since the probability of a reaction occurring despite the kinetic overpotential barrier decreases with increasing temperature [31]:

$$j_{0,bv} = j_{0,ref}e^{-\frac{E_a}{k_bT}} \tag{2.14}$$

in which $j_{0,ref}$ is the exchange current density at a reference temperature, while E_a is the activation energy, which is typically determined experimentally. Note that the activation energy depends on the electrode and the reaction kinetics of the redox species involved, which makes it difficult to predict its value in a specific case.

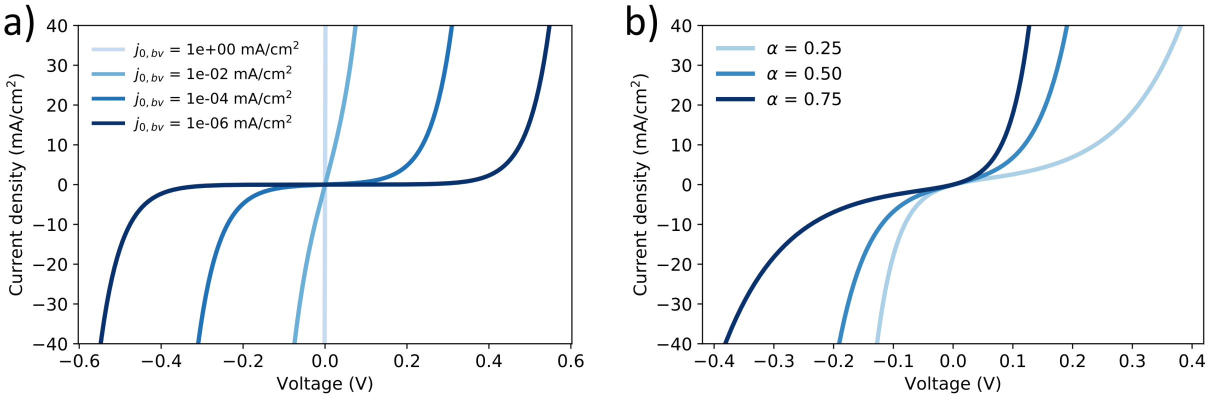

Figure 2.10: IV-curves for different values of $j_{0,bv}$ (a) and α (b), to show the IV-curve-dependence on these kinetic overpotential-parameters

2.2.2 Mass-transfer limits

In realistic cases, the current density is not allowed to diverge to infinity as seen in figure 2.10. To include mass transfer limitations, which account for the finite average time it takes for convertable redox species to reach the electrode, the Butler-Volmer equation is adapted as seen in equation 2.15.

$$\frac{j}{j_{0,bv}} = \left(1 - \frac{j}{j_{mtl,c}}\right) \exp\left(\frac{-\alpha n q(E - E_0)}{k_b T}\right) - \left(1 - \frac{j}{j_{mtl,a}}\right) \exp\left(\frac{(1-\alpha) n q(E - E_0)}{k_b T}\right) \tag{2.15}$$

where $j_{mtl,c}$ and $j_{mtl,a}$ are the mass transfer limited maximum current densities for the cathode and anode respectively. This effect is graphically depicted in figure 2.11. Mass-transfer limitations are improved by more effective stirring of the electrolyte (or higher flow rates) and higher concentration of the electrolyte, such that species can be converted at the active sites of the electrode at a more rapid succession, thus increasing $j_{mtl,c/a}$.

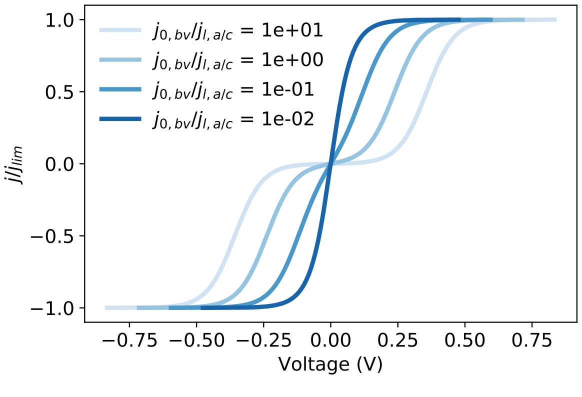

Figure 2.11: Plot of current density relative to the mass-transfer limit versus voltage for different values of $j_{0,bv}$ relative to the mass-transfer limited current.

Note that figure 2.11 as well as equation 2.15 both show that at low current densities ($|j| << |j_{l,a/c}|$) mass transport limitations can be neglected, as they have no significant impact on the current-voltage curve in that region.

2.2.3 State of Charge

One of the major differences between using an electrochemical cell to produce hydrogen or perform CO_2 reduction, as opposed to driving reversible redox reactions, is that there is no state-of-charge (SOC) effect. In hydrogen production, for example, the process continuous and steady-state, meaning the electrolyte ideally does not change over time. However in the case of using the electrochemical cell drive redox reactions, the concentrations of the redox species change over time, as they are reduced/oxidized (i.e. as the battery increases its SOC). Intuitively, this would mean that it gets progressively harder to charge the battery since the concentration of 'chargeable' species decreases. In electrochemistry, this state-of-charge effect is described by the Nernst equation [29]:

$$E_{redox} = E^0_{redox} + \frac{RT}{nF} \ln \frac{C_O}{C_R} \tag{2.16}$$

in which E_{redox} is the concentration-dependent redox potential, E^0_{redox} is the standard redox potential, defined at 50% SOC and C_O and C_R are the concentrations of the oxidative and reductive species respectively. Rewriting this in terms of the SOC for single-electron reactions gives [17]:

$$V_{cell} = \Delta E^0_{redox} + \frac{RT}{F} \ln \left(\frac{SOC^2}{(1 - SOC)^2} \right) \tag{2.17}$$

in which ΔE^0_{redox} is the difference in voltage between the two standard redox potentials of the active species and SOC is the state of charge (between 0 and 1). When plotting the cell voltage in equation 2.17 as a function of the SOC, as seen in figure 2.12, it is clear that higher SOCs result in higher cell voltages, which means higher voltages are needed to keep charging beyond 50%.

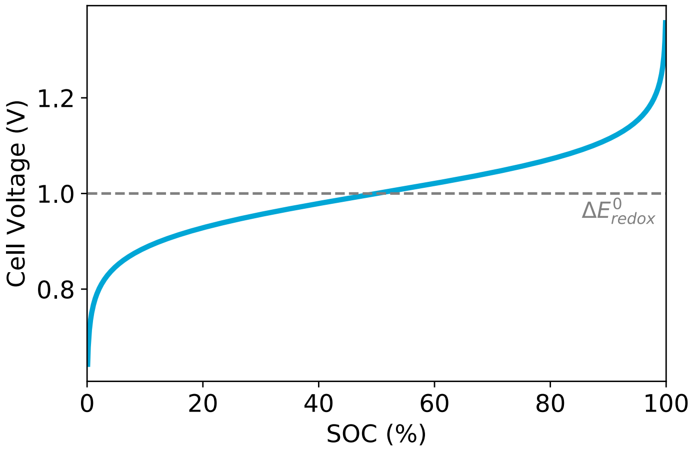

Figure 2.12: Cell voltage plotted versus state-of-charge, for a cell with a $\Delta E^0_{redox} = 1V$. Note that the cell voltage is 1V at 50% SOC.

Note that figure 2.12 and equation 2.17 show that the cell voltage is equal to ΔE^0_{redox} at 50% SOC.

2.2.4 Ion-crossover

The membrane of an electrochemical cell is never perfect and there are bound to be redox species crossing over from the anolyte to the catholyte and vice versa. This decreases the total capacity of the battery since crossed species cannot be charged anymore. On top of that, minor spontaneous discharge will occur, decreasing the capacity even further. Although this issue touches on the long-term stability of the battery, which is crucial in practical applications, this work will focus on optimizing the charging efficiency and will not consider cross-over and other membrane-related losses in detail.

2.2.5 Internal resistances

Further losses are induced by the finite conductivity of the electrolyte, as well as the selective membrane. Since the electrolyte resistance differs with respect to the used redox species and supporting electrolyte, the situation-specific resistances are not used to establish the general modeling trends. However, in the case-specific predictions, experimental values for electrolyte resistances are used. Since this work focuses on the charging efficiency, the selective membrane is not considered in detail, but rather its resistance is estimated as a constant value throughout this work.

2.3 The photo-electrochemical redox flow battery

Combining both the photovoltaics and electrochemistry discussed in the previous sections results in a photo-electrochemical redox flow battery. The coupling and interactions between these two fields coming together in this device are discussed in this section, starting with the schematic representation, shown in figure 2.13. In short, a PEC flow battery converts light into charged redox couples. It does so by absorbing incoming photons with an energy larger than E_g. Due to the electric field caused by the pn-junction (as seen in section 2.1), the electrons will flow towards the catholyte, to reduce it. The holes will travel through the wire and carbon electrode to the anolyte to oxidize the redox-species there. This means the photo-voltaic component acts as the voltage source (or more precisely: the current source) in figure 2.9.

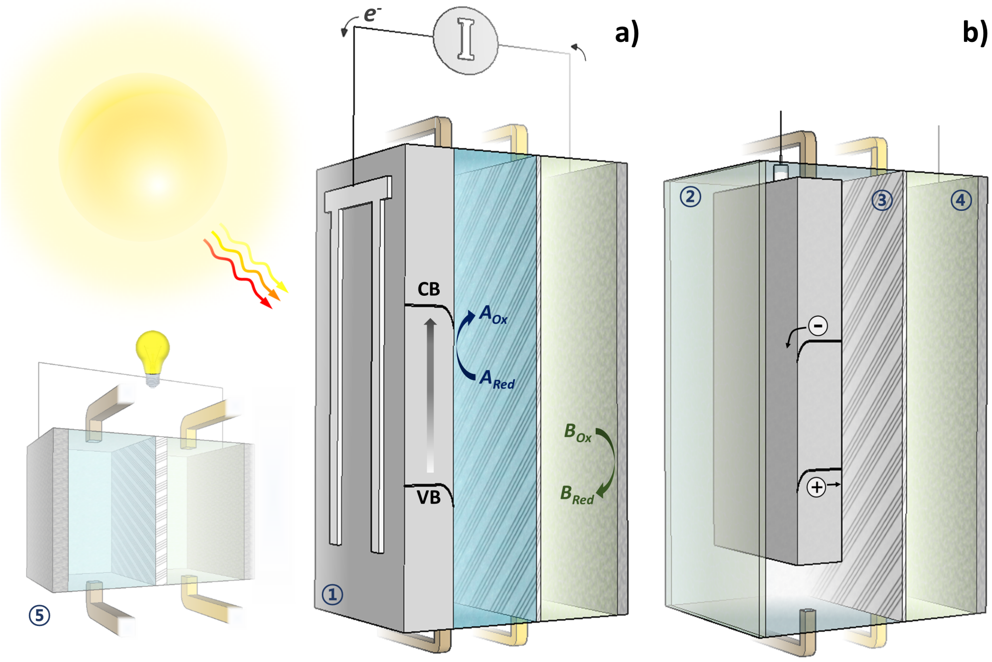

Figure 2.13: Schematic of solar charging compartments for the SRFB system. (a) Charging cell with a back-side illuminated device and (b) cell with front-side illuminated device (i.e., illuminated through the window (2) and the electrolyte). Photocathode (1) in the catholyte (with redox couple A) and a polarizable counter electrode (4) in the anolyte (with redox couple B) are separated by an ion-exchange membrane (3). In practical applications, RFB stack (5) is connected in series with storage tanks and pumps (not shown) for discharging the solar-charged electrolytes. Subscripts (Ox and Red) denote the oxidized form and reduced form of the redox couples. CB and VB correspond to the conduction and valence band edges of the semiconductor, respectively. Note that the illustration is not to scale.

Other key-components in this setup are the conducting layer and the selective membrane, which was already discussed in section 2.2. The conducting layer has a protective as well as a catalytic role, which will be discussed in section 2.3.2.

One major distinction to be made in the PEC flow battery field is frontside- versus backside-illuminated devices. Both configurations are shown in figure 2.13. Most current research is being done using front-side illumination, in which the light has to travel through the electrolyte before being absorbed by the semi-conductor. These two set-ups behave differently due to varying parasitic light loss and different technical challenges.

2.3.1 band-diagram throughout the PEC-device

A major part of the conceptual understanding of an SRFB is found in the band-diagram, energy levels, and equilibration processes throughout the device. A schematic representation of the band-diagram is shown in figure 2.14.

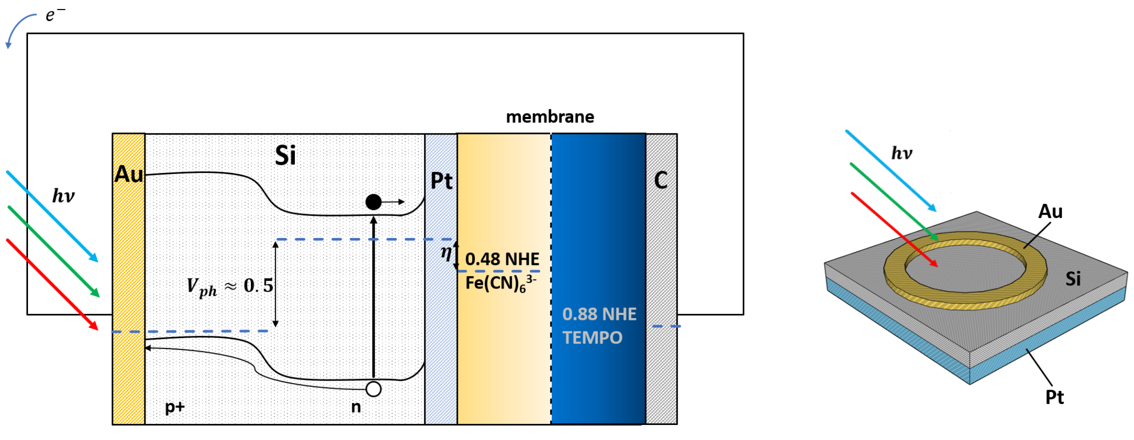

Figure 2.14: Schematic representation of the band-diagram throughout an example setup of a PEC redox flow battery

First of all, the silicon photo-absorber contains a p+/n junction (with p+ meaning highly doped p-type silicon), exhibiting the internal band-banding as explained in section 2.1. Furthermore, a platinum (Pt) conducting layer is shown, which equilibrates its Fermi level, with the redox potential of the $Fe(CN)_6^{3/4-}$ reaction. However, the fermi-level of the conducting layer and the redox potential of the adjoining electrolyte differ due to the kinetic overpotential (or kinetic barrier), η_k, as seen in the schematic. [29, 30] Due to the equilibration of the Fermi levels of the conducting layer and the semi-conductor, a Schottky barrier arises, as discussed in section 2.3.2, displayed as the upward band-bending close to the interface. In this work, a conducting ring (Au in figure 2.14) is deposited on the photo-absorber, to collect and transport the charge efficiently. The kinetic barrier at the counter-electrode (a carbon rod in this case), is assumed to have a negligible effect due to the large active area with respect to the photo-absorber.

2.3.2 Conducting layers

The conducting layer is one of the key components of the PEC flow battery. It serves as a catalyst and as a protective layer. As a catalyst, the conducting layer should improve reaction kinetics and result in an efficient electron transfer between the semi-conductor and the electrolyte. Therefore, a conducting layer should result in a high $j_{0,bv}$ and a beneficial α (see section 2.2.1), to minimize the overpotential for charging the electrolyte. Note that the discharging of the PEC is typically done with different electrodes, so the overpotential for the reversed (/discharge) reaction, performed with the photo-electrode, is of no interest. Furthermore, the conducting layer should exhibit low resistance to minimize dissipation.

As a protective component, the conductive layer should be stable under the device's operating conditions, submerged in the respective electrolyte at the operating pH and voltages. This, to protect the semi-conductor from chemical corrosion/oxidation, which would decrease performance.

As seen before in section 2.2, the fermi-level of a conductor in contact with the electrolyte, will equilibrate by adjusting its fermi-level to the redox potential. From solid-state physics, it is known that a semi-conductor in contact with a metal will create a Schottky barrier, schematically displayed in figure 2.15.

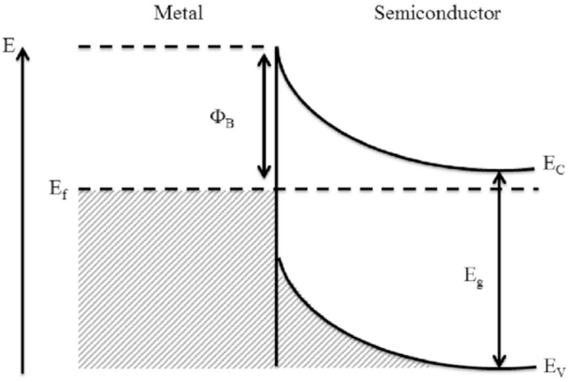

Figure 2.15: Schematic representation of a Schottky barrier [32], in which the semi-conductor band bends due to the fermi-level alignment between the two materials. In the plot, Φ_B is the barrier height, E_g is the band-gap energy and E_C and E_V are the conduction and valence band positions respectively. A space-charge region arises in the semi-conductor, yielding a certain space-charge capacity C_{SC}. This space-charge capacity can be examined using Mott-Schottky measurements. Via the same mechanism, band-bending also arises when a semi-conductor comes into contact with an electrolyte instead of a metal.

For a finite current to be able to occur, this barrier should be thin enough for the electrons to tunnel through. The maximum tunneling current is given by equation 2.18. The barrier height can be experimentally researched using Mott-Schottky measurements by determining the capacity of the space-charge region close to the interface, as seen in figure 2.15.

$$j_{tunnel} = QN_D v_{th} \exp\left(- 4/3 W_b \sqrt{\frac{2m_{eff}\Phi_b e}{\hbar^2}} \right) \tag{2.18}$$

in which N_D is the number of donors in the semi-conductor, v_{th} is the thermal carrier velocity ($\sim 10^7$), m_{eff} is the effective charge carrier mass, Φ_b and W_b are the barrier height and width respectively and $\hbar$ is the reduced Planck constant. The barrier height can be determined using Mott-Schottky measurements (see section 2.5.2.2), or theoretically, using material properties. In the same way the barrier width can be calculated.[17].

2.3.3 Parasitic light loss

Ideally, all incoming solar radiation with an energy higher than the semi-conductor bandgap is absorbed. However, in a practical system, parasitic light loss is unavoidable. There are three major sources of loss to be distinguished in a PEC flow battery device. Parasitic absorption by the electrolyte (in case of a front-side illuminated configuration), reflection by the semi-conductor, or any of the other layers present in the material and imperfect absorption by the semi-conductor, the last of which has been discussed in section 2.1.3.5. In the next paragraphs, the other two sources will be studied in more detail.

2.3.3.1 Electrolyte absorption

In the case of a front-lit configuration, the incoming solar radiation has to travel through the electrolyte to reach the semi-conductor. Due to the finite thickness and absorption of the electrolyte layer, some of the radiation is lost. This can be calculated using the Lambert-beer law:

$$I/I_0 = T_{electrolyte} = 10^{-\epsilon[c]d} \tag{2.19}$$

in which $[c]$ is the concentration of the electrolyte, d is the thickness of the electrolyte layer and ϵ is the molar absorption coefficient. ϵ can be obtained experimentally by normalizing a measured absorption/transmission spectrum with respect to concentration and thickness, or by means of literature data.

2.3.3.2 Reflection

The reflection in case of a back-lit configuration is found simply using the reflectance spectrum of the photo-absorber (which could be coated with an anti-reflection layer to reduce reflection). For a front-lit configuration, there are multiple reflective interfaces.

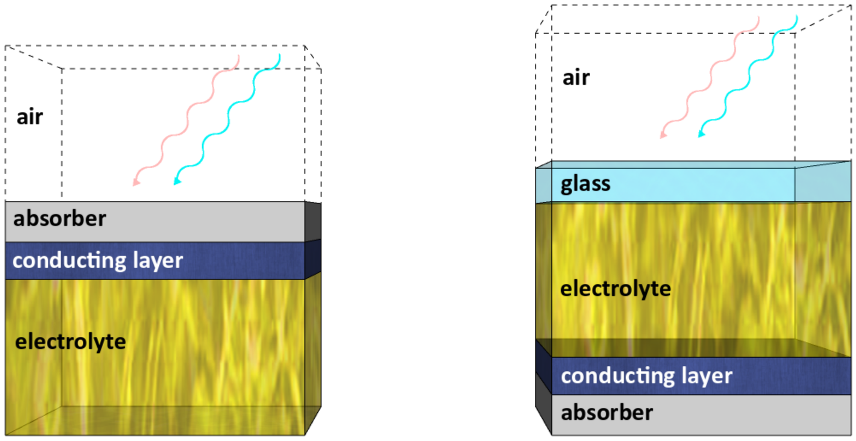

Figure 2.16: Schematic depiction of the different layers the incoming radiation has to cross to get to the (grey) photoabsorber. In case of a back-lit configuration (left), the ligth only crosses the air to get to it, while the radiation has to be transmitted through several more layers in case of front-side illumination (right)

At each interface the portion of reflected can be calculated using Fresnel coefficients:

$$R = \frac{|n_1 - n_2|^2}{|n_1 + n_2|^2}, \tag{2.20}$$

where n_1 and n_2 are the refractive indices of the materials at both sides of the respective interface. Note that to use equation 2.20, normal light incidence is assumed. Of course, this assumption does not always hold in practical solar cells, but in the experiments conducted in this research, the angle of incidence is always 0. The total reflectance is calculated by taking the product of the individual interfaces, as seen in equation 2.21

$$T_{tot,refl} = 1 - R_{tot} = \prod_i (1 - R_i) \tag{2.21}$$

This means the incoming spectrum for the silicon is defined as $I_{Si} = I_0 \cdot T_{tot}$. It is this spectrum, that should be used as an input spectrum to be integrated as seen in equation 2.1.

2.4 The performance estimating model

To find the performance trends of the PEC flow battery, influenced by the different discussed losses and compare these to experimental results, the total device should be captured in a model. In this case, the device is modeled as the electrical circuit, found in figure 2.17.

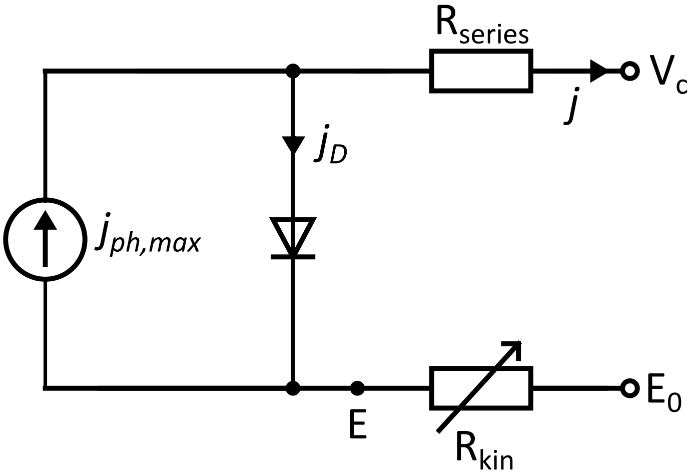

Figure 2.17: Schematic of the circuit representing the PEC flow-battery in the performance estimating model. Most components are already discussed in the earlier circuits, but the kinetic 'resistance' (R kin in the figure) is shown as a variable resistance, to account for the current-dependent kinetic overpotentials.

To find the IV-curve of the device, which is the most important characteristic of the system, the circuit is analyzed to find $V_c(j)$, the circuit voltage (in the figure, the voltage between the two open nodes).

$$V_c - E_0 = V_D + (E - E_0) + V_R, \tag{2.22}$$

where E_0 is the cell voltage, $E - E_0$ is the overpotential, as seen in equation 2.13 and V_R is the voltage drop due to the series resistance. $E - E_0$ can be numerically solved from equation 2.13, but in case of $\alpha = 0.5$, there is an analytic solution, increasing the speed of the calculations significantly. Since the two exponentials can be written as a sinh, the analytic solution can be found in equation 2.23.

$$j = 2j_{0,bv} \sinh\left(\frac{ne(E - E_0)}{2k_bT}\right) \Longrightarrow E - E_0 = \frac{2k_bT}{ne} \operatorname{arcsinh}\left(\frac{j}{2j_{0,bv}}\right) \tag{2.23}$$

V_D is found by using the diode equation, as seen in equation 2.2, where the current through the diode is given as a function of V_D. By solving for V_D, equation 2.24 is obtained (for the detailed derivation, see section A.5 in the appendix):

$$V_D \approx V_{oc} + \frac{k_bT}{e} \ln \frac{j_D}{j_0} \tag{2.24}$$

where V_{oc} is the open circuit voltage as discussed in section 2.1.1 and j_D is the current through the diode, which is equal to $j_{max,photo} - j$. Note that the ideal diode equation is used, since the series resistance is dealt with separately and the shunt resistance is assumed to be negligible, since recent shunt resistances are reported to be high (>2kΩ) [33], which leads to negligible losses as seen in figure 2.8.
Lastly, the voltage drop over the series resistance is simply found using $V_R = jR_{series}$. In this case, R_{series} has the dimensions of the specific resistance $[\Omega \cdot \text{cm}^2]$.

After this, the operating current is determined using the following condition:

$$E_{ph} \geq E_{redox} + E_{dev,loss} + \eta_k \tag{2.25}$$

where E_{ph} is the photovoltage derived by the photo-device, $E_{dev,loss}$ are the device losses due to factors mentioned earlier (electrical resistance, reflection, etc.), and η_k is the kinetic. E_{redox} is the thermodynamic potential which is equivalent to the difference between the redox potentials of redox couples (i.e., $|\phi_{red}-\phi_{ox}|$). The operating current j_{op} can be obtained as the maximum possible current density in the current-voltage characteristic, as modeled before at a voltage that also satisfies the condition in equation 2.25. It is worth noting that the experimental j_{op} ($j_{op,exp}$) is defined by photo-current at zero bias voltage using a two-electrode setup.

The solar-to-chemical efficiency is calculated using:

$$STC = \frac{P_{out}}{P_{in}} = \frac{j_{op}V_{cell}}{P_{in}} \tag{2.26}$$

analogous to the efficiency of a dry photovoltaic device in equation 2.5. Note that an implied assumption to this method, is that the overpotential of the counter-electrode (typically a carbon felt/rod electrode), is negligible, since its surface area is much larger than the photo-electrode. This assumption is verified experimentally and is shown in figure B.1 in the appendix.

2.4.1 Fitting tool

In sections 2.1 and 2.2, the dependencies of the IV curve on several parameters is shown. It is possible to apply these dependencies and fit real experimental data by varying the parameters and minimizing the error. The parameters varied to fit the experimental data are the series resistance (R_{series}), and the parameters $j_{0,bv}$ and α from 2.13. Furthermore, the open-circuit voltage is extracted from the experimental data by simply finding the voltage at which the current is zero. Lastly the mass transport limits and/or the saturation current density for both the cathodic and anodic reaction are found by averaging the experimental current density over the saturation region. The error is defined as:

$$E(\alpha, R_{series}, j_{0,bv}) = \sum_k (j_{model}(V_k) - j_{exp}(V_k))^2 \tag{2.27}$$

in which $j_{model}(V)$ and $j_{exp}(V)$ are the modeled and experimentally measured currents at a specific voltage V. The error is minimized by using the dual annealing method from the scipy.optimize toolbox. The average error per data point is given by the following equation:

$$E_{average} = \frac{1}{N}\sum_k |j_{model}(V_k) - j_{exp}(V_k)| \tag{2.28}$$

Note that the series resistance, found by fitting this model, is the total series resistance, originating from both internal resistance in the PV module, as well as the solution and membrane resistance in the electrochemical cell.

2.4.2 Temperature dependence & Heat Balance

A lot of the equations in chapter 2 depend on the photo-absorber temperature. It influences IV-curves, kinetic overpotentials and SOC effects, all having their own effect on the STC. Therefore, the photo-absorber temperature is varied, to examine its influence on the STC% Moreover, a practical model should calculate the photo-absorber temperature, based on situation-specific parameters. To just assume a photo-absorber temperature equal to the ambient air temperature would be too simplistic, due to part of the incoming solar radiation being dissipated into heat, thus increasing the absorber temperature. Therefore, a heat balance method is employed, to solve for the photo-absorber temperature and increase the accuracy of the performance estimations. The heat balance is a tool which uses radiative as well as convective heat fluxes, depending on the temperature of the several components and is given in equation 2.29:

$$\phi_{in} = \sigma(T^4 - T_{el}^4) + \sigma(T^4 - T_{air}^4) + h_{air\leftrightarrow abs}(T - T_{air}) + h_{el\leftrightarrow abs}(T - T_{el}) \tag{2.29}$$

in which T is the photo-absorber temperature, T_{air} and T_{el} are the ambient air and electrolyte temperature respectively, $h_{x\leftrightarrow y}$ is the heat transfer coefficient between component x and y (el, air and abs indicating the electrolyte, ambient air and photo-absorber respectively). Lastly, ϕ_{in} is the part of the incoming solar energy which is dissipated into heat. Note that the heat balance in equation in 2.29 is steady-state and thus assumes rapid photo-absorber temperature equilibration. This will be discussed in more detail in section 2.4.2.1.

To determine ϕ_{in}, the losses should be identified and included. An overview of the losses is schematically depicted in figure 2.18.

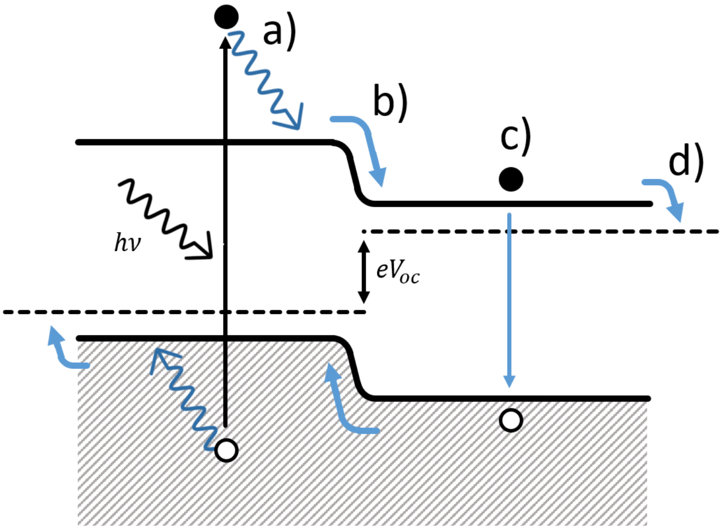

Figure 2.18: Schematic overview of losses in the semi-conductor. The energy $h\nu$ of the incoming photon is partially lost due to thermalization (a), the Joule effect, which is the energy lost due to the internal band bending (b), recombination (band to band and Auger)(c) and the Peltier effect, which takes into account the difference between the quasi-fermi levels and the band edges (d).

Several processes result in the dissipation of energy into heat, as explored more in-depth in literature [34]. Thermalization, the Joule and Peltier effect and recombination effects in general result in the electrons losing energy and dissipating the losses as shown in figure 2.18. In this model, the assumption is made that only the fraction of the photon energy which corresponds to eV_{oc} is used to effectively increase the electron energy, while the rest is dissipated into heat. In other words, of the photon energy E_{ph}, the part $E_{ph} - eV_{oc}$ is dissipated and fed into the heat balance as ϕ_{in}. In mathematical terms:

$$\phi_{in} = \int_0^{\lambda_g} H(E(\lambda) - eV_{oc}) \cdot (E(\lambda) - eV_{oc}) N(\lambda) d\lambda \tag{2.30}$$

where $H(x)$ is the Heaviside step function, which is defined to be zero for $x < 0$ and one for $x > 0$, to eliminate the non-physical negative contributions. Due to the high specific heat of water (assumed to be similar to the specific heat of the electrolyte), the electrolyte temperature T_{el} will in general not be equal to the ambient air temperature. Furthermore, the steady-state heat balance can not be used, due to the slow equilibration process caused by the high specific heat value. Therefore, the transient heat balance is needed to describe the heating and cooling of the electrolyte:

$$\sigma A(T_{el}^4 - T^4) + \sigma A_{el\leftrightarrow air}(T_{el}^4 - T_{air}^4) + h_{el\leftrightarrow abs} A(T_{el} - T) + h_{el\leftrightarrow air} A_{el\leftrightarrow air}(T_{el} - T_{air}) = -\rho V c_v \frac{dT_{el}}{dt} \tag{2.31}$$

in which the $A_{x\leftrightarrow y}$ is the contact area between component x and y, and V, ρ and c_v are the volume, density and specific heat of the electrolyte. As will be seen in section 2.4.3, the dynamic system parameters form complex dependencies, that can only be solved iteratively. Discretizing the transient heat balance in the same way gives:

$$T_{el}(t + dt) = T_{el}(t) + \frac{Q_{in,el}(t)}{\rho V c_v} dt \tag{2.32}$$

in which $Q_{in,el}$ is the incoming heat flux for the electrolyte, corresponding to the left hand side of equation 2.31. Using equations 2.30 and 2.32 and reasonable values for the heat transfer coefficients and ambient air temperature, the steady-state heat balance in equation 2.29 can be numerically solved for T.

Note that the open-circuit voltage depends on the temperature (due to the temperature dependence of j_0, as seen in section 3.2.2), while the temperature depends on the open-circuit voltage since the dissipated heat fraction depends on open-circuit voltage (see equation 2.30). The problem of this circular dependency is solved by iterating the temperature/V_{oc} calculations until convergence.

2.4.2.1 Assumptions and Limitations

In this method of determining the photo-absorber temperature, it is assumed that the photo-absorber is in thermal equilibrium. When including real data or other time-dependent processes, this means these processes need to be slow with respect to the simulated timescale, to ensure the steady-state heat balance can be used. This is the case when the absorber itself has a low effective specific heat such that the temperature equilibrates quickly, relative to the other time-dependent processes. Due to the very low thickness of a photo-absorber (approximately 100-1000 μm), this seems like a reasonable assumption.
Also, the geometry of the silicon absorber is not considered in this work. Spatial distribution of the temperature could arise, due to the non-uniform charge generation and charge collection probability (see section 2.1.1), however due to the high thermal conductivity of silicon [35] and low photo-absorber thickness, this effect is assumed to be negligible.
Moreover, the heat transfer coefficients are based on some reasonable general values, rather than on a fundamentally sound calculation. Forced convection by variable wind speed or high flow speeds inside the redox flow battery could increase these coefficients, while a layer of relatively static and hot air around the pec device could have the opposite effect.

The specific heat of the electrolyte is assumed to be close to that of water. As tested by Urban [36], the specific heat reduces slightly for a wide variety of electrolytes, due to the ions restricting the free movement of the water molecules. However, even at high concentrations (i.e. 1 Molal ($\approx$ 1 Molar in case of a water solvent)), this effect reduces the specific heat by a maximum of 1-2% (but in most cases around 0.5%), which is not considered to be a significant difference for the purpose of this model.
Furthermore, it is assumed that at the start of the simulation, the electrolyte has fully equilibrated with the electrolyte, so $T_{el} = T_{air}$ at $t = 0$. In case of using real data (see section 2.4.3), this means that the

electrolyte has equilibrated fully with the ambient temperature during the night.

Lastly, the positive effect of increasing temperature on the reaction kinetics (see equation 2.14) and on solution resistance is only considered for the well-documented hydrogen and oxygen evolution reactions, since the activation energy E_a and $j_{0,ref}$ are poorly documented for specific redox reactions and redox species.

2.4.3 Time-dependent processes

A major advantage of this model is, that situations beyond a perfect lab environment can be simulated. In practice, PEC-redox flow batteries are situated outside, where the incoming radiation fluctuates over the day and over the year. Furthermore, as seen in section 2.4.2, the photo-absorber temperature is dependent on this fluctuating incoming spectrum as well as on the ambient temperature. Therefore, measured incoming solar radiation and ambient air temperature can be used as an input for the model. Examples of real solar spectral data on a typical winter/summer day taken from NREL in Colorado [37] are shown in figure 2.19.

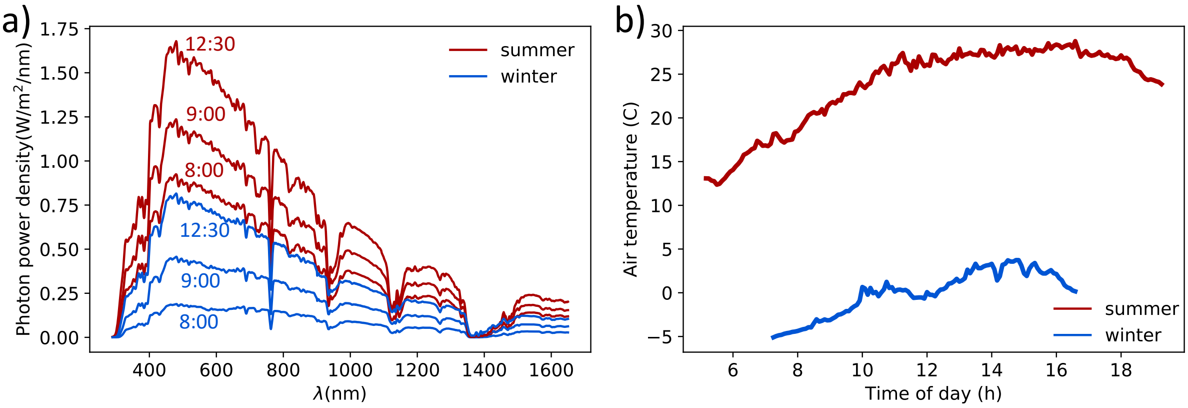

Figure 2.19: Time-dependent solar spectra (a) and ambient air temperature (b) for both a typical summer and winter day in Colorado.

Lastly, the battery charges over the course of the day, increasing the SOC, which influences the cell voltage, which in turn changes the STC. The SOC as a function of time can be approximated iteratively, using the following equation:

$$SOC(t + dt) = SOC(t) + \frac{j_{op}(t, SOC) \cdot A \cdot dt}{Q_{battery}}, \tag{2.33}$$

where A is the absorbing area of the semi-conductor, dt is the time-resolution and $Q_{battery}$ is the charge capacity of the battery in coulombs, which can be calculated as:

$$Q_{battery} = [c]VN_A ne \tag{2.34}$$

Note that the SOC can only be calculated iteratively since the increase in SOC depends on j_{op}, which in turn depends on the SOC. Using these practical and time-dependent inputs and effects, the performance of an SRFB in practical situations can be estimated. This part of the model is relevant since the optimum design parameters depend on the environment.

2.5 Experimental methods

2.5.1 Device fabrication

2.5.1.1 Photo-electrode

The photo-charging and LSV experiments with the back-side photo-cathode (BPC) and back-side photo-cathode are conducted using p^+/n and n^+/p silicon wafers, of which the fabrication is discussed in the following sections. The dark electrochemistry experiments are done using

p^+/n Silicon fabrication The thickness of the n-type CZ c-Si wafer was 350μm ([100]; Topsil, 1–20 ohm·cm). The shallow n/p^+-junction was produced in n-type Si wafer by thin p+ doping using an atmospheric pressure tube furnace in close proximity with BoronPlus planar diffusion sources. The temperature was ramped up to 950C at a rate of 10 C/min in 0.1 SLM oxygen and 8 SLM nitrogen. The boron phase-layer was removed by dipping the wafers in a buffered HF bath for 5 min. Then the dopant on the backside (unpolished) of the wafer was removed by etching in a reactive ion etching (RIE) process (Pegasus, SPTS Technologies). 3 μm tall mesas on the front of the wafer were defined by UV lithography followed by a 3 μm deep RIE etch. The fabrication of the n^+/p silicon is based on the same principles.

Conductive layers The conductive layers were attached to the created p^+/n and n^+/p Si-semiconductors using reactive sputter deposition at various pressures and deposition temperatures. The deposition rate was calibrated with an in-chamber QCM (quartz crystal microbalance). A ring-shaped Au layer was deposited on the p^+-Si(/n^+-Si) surface using a reactive sputtering with a home-made metallic mask at room temperature. The surface was cleaned with Ar-sputtering in vacuum to remove the native oxide layer.

For the electrochemical experiment under the dark, various conducting layers, including the Pt, C, and Ti were deposited onto highly-doped n+-Si substrates. The carbon was sputtered at room temperature or 400C. In the case of the TiO_2, a thin layer of titanium was sputtered on first to prevent silicon oxidation in the subsequent TiO_2 reactive sputtering step at 400C as described elsewhere.[17, 10]
The electrochemical measurements of the photoelectrodes were conducted using both three-electrode as well as two-electrode configurations. The solar charging has been done under simulated AM1.5 solar irradiation (100 mW cm^{-2}) for both back- and front-illuminated cases (figures 2.13 and 2.16). During the measurements, an electrolyte of 40 mL was continuously circulated by a peristaltic pump at 70 mL min^{-1}.

2.5.1.2 Electrolytes

The synthesis of TEMPO-4-sulfate was based on the previous study.[17] 4-Hydroxy- TEMPO (Henan Tianfu Chemical Co. LTD, >99%) was added to concentrated H_2SO_4 (Sigma Aldrich 97%) at a molar ratio of 0.044. The solution reacted at room temperature for 20 min and dripped slowly into a suspension of $NaHCO_3$ (Sigma-Aldrich) resulting in a neutral, yellow solution. The solution was shaken with ethyl acetate (Sigma-Aldrich) and the ethyl acetate phase was discarded, before concentrating the aqueous solution of the reaction product at 50C using a rotary evaporator. And then acetone was added to precipitate Na2SO4. The acetone phase was then evaporated using a rotary evaporator again, and the resulting red/orange salt was used without further purification. $K_3Fe(CN)_6$ (Sigma-Aldrich, >99%), $K_4Fe(CN)_6$ (Sigma-Aldrich, >99.5%) are used as received after mixing with 1M NH_4Cl to make a 0.4M $[Fe(CN)_6]^{3/4-}$ electrolyte depending on the usage of the ferri/ferrocyanide as anolyte or catholyte. For UV-Vis characterization of the SOC-trend, the ferri-/ferrocyanide are mixed to create 0.4M electrolytes with varying SOC.
To create the 0.4M Br^- anolyte, NH_4Br (Sigma-Aldrich, >99.99%) is mixed with 1M NH_4Cl. The Cu^{2+}-catholyte is made by mixing $CuSO_4 \cdot 5\ H_2O$ (Sigma-Aldrich, >99%) with 1M NH_4Cl.

After mixing, the pH of the electrolytes was controlled by adding an NH_4OH solution until neutral conditions were obtained. Especially due to the unstable nature of ferri-/ferrocyanide electrolytes at low pH, this is a crucial step.

2.5.2 PEC setup and characterization

Two PEC setups are used for the electrochemical experiments. The half-cell contains one electrolyte, for studying the photo-electrode performance for the half-reaction (in this work this is ferri-/ferrocyanide conversion) under dark and illuminated condition. The dual cell contains the two electrolytes, separated by the membrane to form the full battery, used to study the overall PEC flow battery performance, by means of battery cycling, photo-charging and CV/LSV experiments, which will be discussed in following sections. The two setups are schematically depicted in figure 2.20.

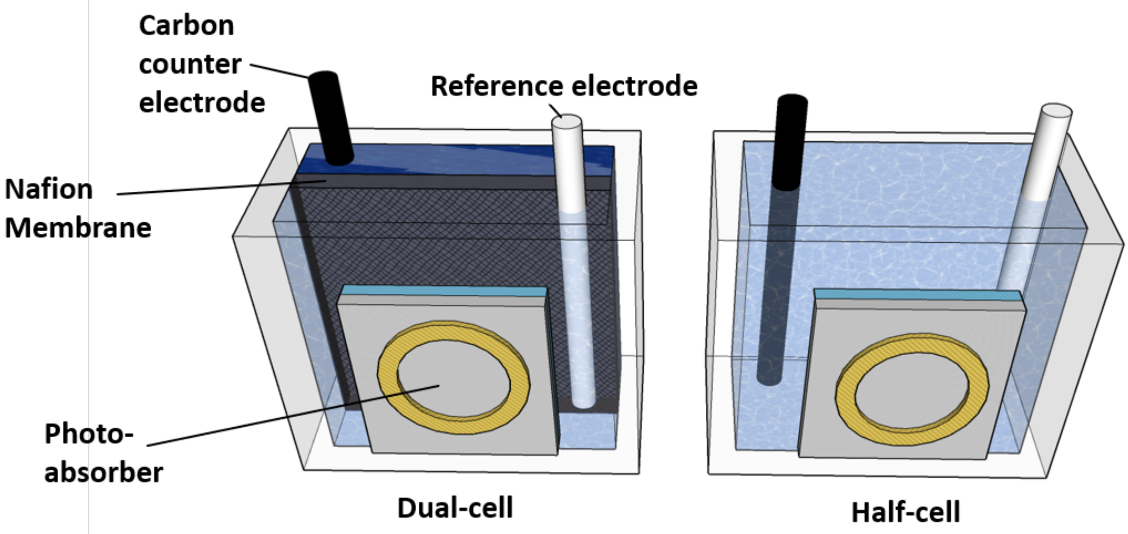

Figure 2.20: Schematic depiction of the setups used for electrochemical characterization of the photo-absorber as the working electrode. In both the dual-cell (left) and the half-cell (right), the carbon counter electrode and Hg/$HgSO_4$ reference electrode are submerged in the electrolyte. In the case of the dual cell, two electrolytes are separated by a Nafion charge selective membrane. The photo-absorber and counter electrode are placed in their separate respective electrolytes and the reference electrode (which is omitted in some experiments to obtain two-electrode measurements) is submerged in the same electrolyte as the photo-absorber). In the half-cell, all electrodes are submerged in the same electrolyte reservoir.

A PARSTAT MC potentiostat (Princeton Applied Research, AMETEK) and a Hg/$HgSO_4$ reference electrode were used for all electrochemical measurements. The solar charging and PEC experiments have been done under simulated AM1.5 solar irradiation (100 mW·cm^{-2}) using a Newport Sol3A Class AAA solar simulator with a 450W Xenon short-arc lamp. The solutions were purged with nitrogen before and during measurements.
Several methods are employed to characterize the photo-electrochemical redox flow battery experimentally, to both estimate performance, as well as to check the validity of the modeled results. In the next sections, these methods are discussed.

2.5.2.1 Cyclic voltammetry - Linear Scan Voltammetry

One of the main characteristics of the PEC redox flow battery is the IV-curve. Cyclic and Linear Scan Voltammetry (CV and LSV respectively) are electrochemical methods, in which the voltage between the two electrodes in the PEC-setup is varied, while measuring the output current, thus obtaining IV characteristics. To relate the relative voltages in two-electrode measurements to an absolute scale (e.g. NHE), a third

electrode (i.e. the reference electrode) is added to the system. The reference electrode contains a solution with a known constant redox potential (e.g. a saturated KCl solution). The potential between the working electrode (in this case the photo-electrode) and the reference electrode is varied in this case.
In an LSV the voltage is swept once over the desired voltage range, resulting in the IV-curve. In CV, however, the voltage is cycled multiple times. This allows for exploitation of hysteresis in the setup, which is used to experimentally determine the redox potential of active redox species. When performing a CV for a single-step reaction at low concentration, peaks arise, as seen in figure 2.21. When increasing the voltage from below E_0 (focusing on the first half of the cycle), the current increases when approaching the redox potential E_0, due to the conversion of active species. Due to the conversion, the local surface concentration of the active species decreases, in turn decreasing the current. Higher scan speeds result in more pronounced peaks. When increasing the voltage beyond the peak voltage, the current is limited by mass transfer to the electrode surface, thus resulting in a constant current.

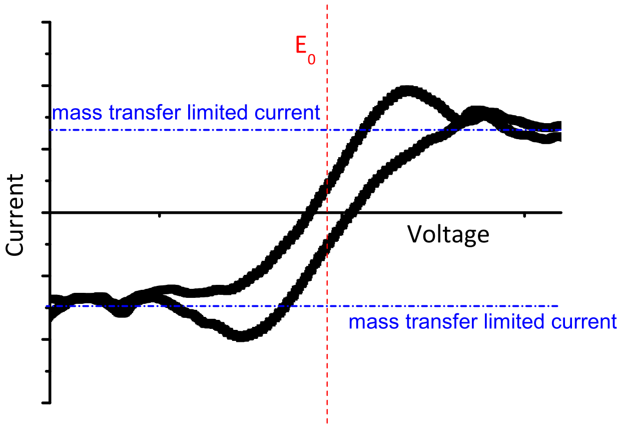

Figure 2.21: Typical cyclic voltammetry measurement, where the redox potential can be experimentally found as the average of the two peak voltages. Note that for voltages sufficiently high and low respectively, a constant current is reached, limited by mass transfer to the electrode surface.

When cycling in the opposite direction (focusing on the second half of the cycle), the exact opposite reaction takes place, resulting in an identical peaked shape, with negative currents. In general, the shape of this cyclic voltammogram (CV) is not symmetric, due to asymmetric kinetics (see section 2.2.1), or mass transfer limits (see section 2.2.2). The redox potential is experimentally defined as the average between the peak voltages. CVs are also used at slower scan-speeds to examine the stability of the IV-curve.

2.5.2.2 Mott Schottky

A Mott-Schottky analysis is done by measuring the capacitance of the space-charge region (see section 2.3.2) of the semiconductor in contact with the conducting layer (C_{SC}). The relation between C_{SC} and the applied voltage is given by the Mott-Schottky equation:

$$\frac{1}{C_{SC}^2} = \left(\frac{2}{e\epsilon\epsilon_0 N_D}\right)\left(V - E_{fb} - \frac{kT}{e}\right) \tag{2.35}$$

in which ϵ and ϵ_0 are the relative permittivity of the material and the absolute permittivity of the vacuum respectively, N_D is the donor concentration and E_{fb} is the flat-band potential. Plotting $1/C_{SC}^2$ and extrapolating the linear region to $1/C_{SC}^2 = 0$ yields the E_{fb}, which is the potential at which the band-bending due to the Schottky barrier is canceled by the applied bias potential, thus providing information about the barrier height. Moreover, the slope of the linear region can be used to determine the doping concentration N_D. In this work, the Mott-Schottky measurements are done at 0.3 kHz using the same setup as described in section 2.5.2, with the exception of the dark conditions for the Mott-Schottky measurements.

2.5.2.3 UV-Vis

The optical properties of several device components are measured using a PerkinElmer-Lambda 900 UV-Vis spectrometer. The focus is on measuring the transmission spectrum of the electrolyte. Since the optical properties of every (composition of) electrolyte(s) are unique, they can be used to establish a trend-line for increasing state of charge, allowing for an estimate of the SOC after charging the battery. Furthermore, it is used to examine the composition of electrolytes after charging (e.g. to identify ion cross-over during the experiment).
Prior to the UV-Vis measurements, a baseline calibration is conducted to account for fluctuations of the illumination source and other irrelevant properties (such as the transmission spectrum of the supporting electrolyte).

2.5.2.4 Chrono-amperometry

The long-term photo-charging performance and stability are researched experimentally by means of chrono-amperometry in a two-electrode setup, by applying zero bias-potential and measuring the photo-current. Moreover, the open-circuit voltage was measured at various points during the charging process, to examine the cell voltage over time (unfortunately a four-electrode setup is needed to allow for simultaneous photo-charging and continuous cell voltage measurements). Analogous to equation 2.26, the estimated STC% can be estimated from the chrono-amperometry using the following equation:

$$STC = \frac{V_{cell}(SOC) \cdot j_{photo,unbiased}}{100\text{mW/cm}^2} \tag{2.36}$$

in which the cell voltage V_{cell} depends on the SOC following the Nernst equation (equation 2.17) and $j_{photo,unbiased}$ is the unbiased photo-voltage, provided by the illuminated PV-module. The input power is 100 mW/cm^2 as discussed in section 2.5.2. The SOC is determined using the calculated input charge relative to the total capacity of the battery:

$$SOC(t) = \frac{Q_{acc}}{Q_{battery}} = \frac{\int_0^t j_{photo,unbiased}(t')dt'}{Q_{battery}} \tag{2.37}$$

with $Q_battery$ being the battery charge capacity, defined in equation 2.34 and Q_{acc} is the accumulated charge, calculated by the potentiostat software by integrating the current over time.

2.5.2.5 Active area measurement

The active photo-absorber area is measured using the image processing software ImageJ.

Chapter 3

Results

In this chapter, the experimental, as well as the modeling results and the comparison between the two is discussed. Since part of the modeling depends on the experimental results, the experiments will be discussed first.

The experiments are done in collaboration with Gerasimos Kanellos, who performed all photo-electrode fabrication, delivered the largest part of the experimental data, discussed in this work and assisted the experiments needed for the modeling validation and model fitting.

3.1 Experimental results

3.1.1 Conducting layer characterization

Electrochemical current-voltage measurements were performed (figure 3.1) in order to study the electrochemical reduction reactivity of the various conducting materials sputtered on highly-doped silicon (c-Si) substrate (see inset). The measurements were performed using the half-cell setup as seen in figure 2.20. For some samples TiO_2 protection layer was sputtered as described elsewhere [38, 39] prior to the conducting

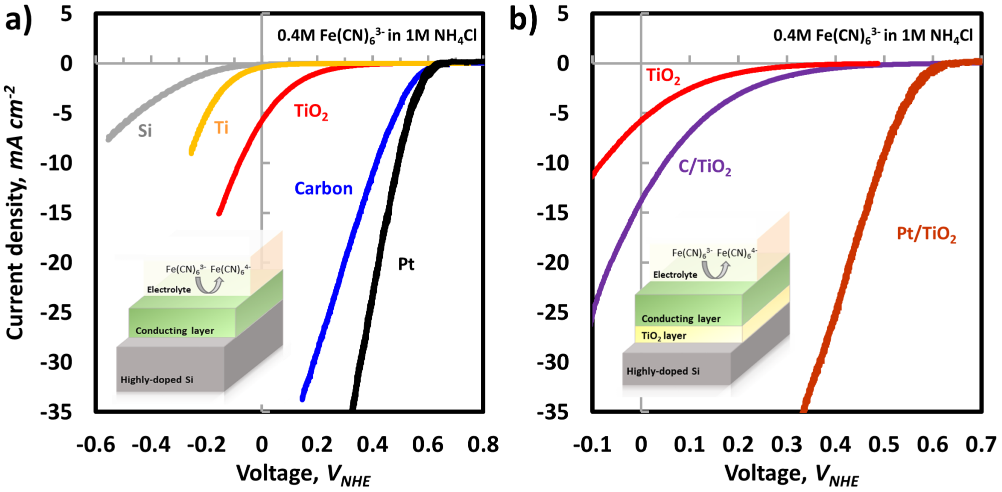

Figure 3.1: Electrochemical CV results for various conducting layers deposited directly on the degenerately doped Si (a) and samples with TiO_2 interlayer deposited on the same substrate (b). Both measurements were carried out in 0.4M $[Fe(CN)_6]^{3-}$ with 1M NH4Cl supporting electrolyte at pH 7 (adjusted by using NH_4OH).

layer deposition (figure 3.1b). Good performances with high onset potentials (V_{on} at 10 mA cm^{-2}) were observed for the as-deposited Pt and carbon films (figure 3.1a, black and blue) during the cathodic reduction of $[Fe(CN)_6]^{3-}$ (i.e., 0% SOC) in 1M NH_4Cl. The samples exhibit similar trend under anodic reaction conditions (as seen in the extended measurements in figure 3.2), indicating that it is not related to chemical affinity difference between the catholyte and anolyte.

As shown in figure 3.1, Pt shows outstanding kinetics, however, noble metals like Pt are not recommended for RFB applications since bubbling formation due to the concurrent hydrogen evolution reaction, which may lead to mechanical damage of the system. It has been accepted that conventional redox reactions in RFB are non-selective with respect to the electrode material[40] unless the intermediate catalytic reactions take a place, such as metal hydride in acidic supporting electrolyte.[41] Despite the fact that the redox reaction of the ferri-/ferrocyanide involves a simple single-electron transfer reaction, an obvious material-dependency was observed for both cases (with and without a protective layer). Particularly, a sample with metallic Ti thin film showed a huge overpotential ($\sim$ 0.7 V with respect to redox potential (E^0_{redox}) of the ferri-/ferrocyanide reaction). Poor reactivity of the bare c-Si sample (figure 3.1, grey) would be attributed to a deactivation of the surface by oxidation or silano-group formation as confirmed by previous studies.2,19 Interestingly, while the sample with Pt and TiO_2 interlayer showed almost unchanged result compared to the result from the sample without the TiO_2 in figure 3.1a the combination of the carbon with the TiO_2 resulted a huge negative shift in V_{on} ($\sim$ 0.9 V). TiO_2 film showed an efficient charge transfer performance proven for water reduction studies. [39, 17] Therefore, this unexpected poor activity in ferricyanide reduction cannot be explained by a conductivity investigation.

For an accurate utilization of the fit tool, described in section 2.4.1, extended range measurements at 50% SOC are needed, such that both the anodic, as well as the cathodic behavior of the photo-electrodes are considered. These extended dark measurements are shown in figure 3.2a. Note that in this case, no full photo-diode (with pn-junction) is used, as such a configuration does not conduct current in both positive and negative direction. The results displayed in figure 3.2, are obtained using n-type silicon, coated with platinum, carbon, and titanium conducting layers respectively.

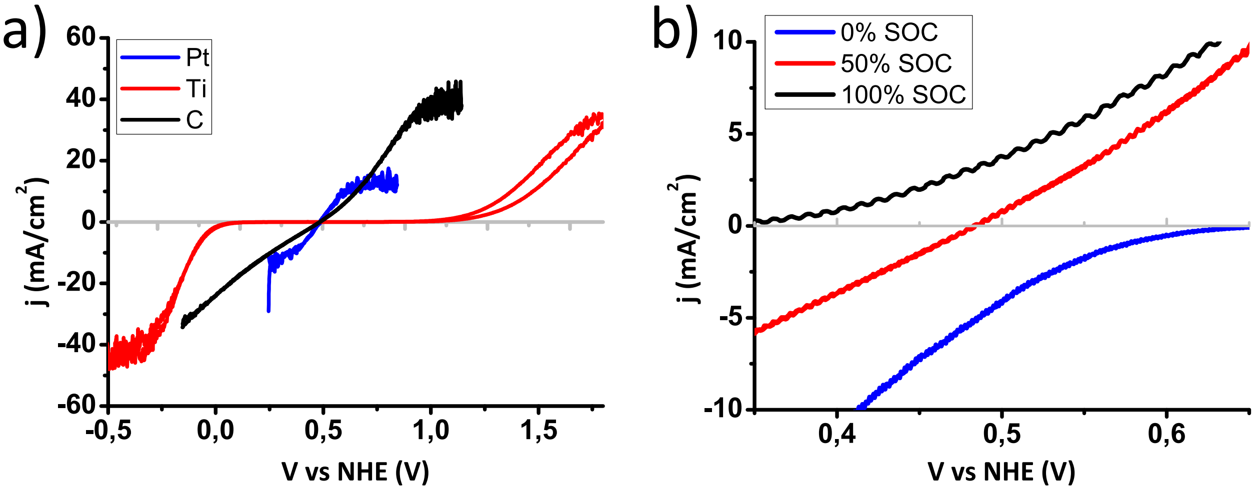

Figure 3.2: Dark electrochemical IV curves of n-type silicon, coated with platinum, carbon and titanium at a 50% SOC (a). The differences in overpotential barriers are clearly visible, ranging from substantial (Ti) to small (C) to negligible (Pt). In b the dark electrochemical curves of the carbon-coated photo-absorber are shown for different SOC, showing the shift in redox potential, as described by the Nernst equation.

As expected, the IV-curves in figure 3.2a follow the same trends for kinetic overpotentials (with the platinum-coated electrode having the best kinetics, followed by carbon and titanium having the worst kinetics), which is shown quantitatively in section 3.3.1. Figure 3.2b shows the SOC-dependence of the IV-curve of the half-reaction, by measuring the IV-curve at 0, 50 and 100% SOC for the carbon-coated electrode. It is seen that the onset potential shifts, indicating the redox potential increases with SOC according to the Nernst equation (see section 2.2.3).

3.1.2 Characterization redox species

The CV measurements for the characterization of the four electrolytes used in this work are shown in figure 3.6a. The found redox potentials are depicted as the dashed lines. As seen from the cyclic voltammograms (CVs) in figure 3.3, the redox couples are electrochemically reversible and the redox potentials are as expected from previous reports.[17, 42, 43]

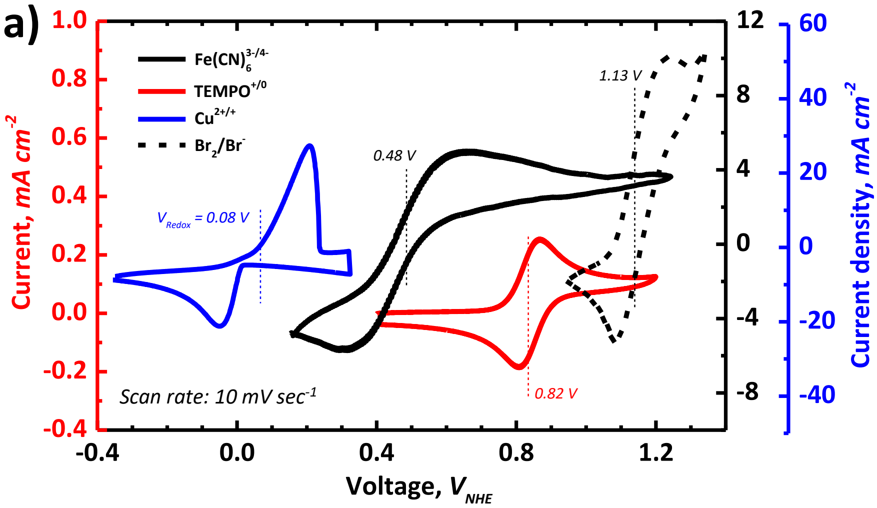

Figure 3.3: CVs of 2 mM solutions of TEMPO-sulfate (red), CuSO4 (blue solid), $K_3Fe(CN)_6$ (black) and NH4Br (blue dased) using a scan rate of 10 mV sec-1. For the TEMPO-sulfate, $K_3Fe(CN)_6$ and NH_4Br, NH_4Cl was used as a supporting electrolyte, and the pH was adjusted to 7. Note that pH of the Cu^{2+} electrolyte was adjusted to 2 (with H_2SO_4) in order to prevent the precipitation of copper.

In this work, ferri-/ferrocyanide is used as the electrolyte, which will be converted by the photo-cathode/-anode. To demonstrate the photo-charging behaviour and overall device performance for different cell potentials, TEMPO, copper-sulfate and NH_4Br are used as counter-electrolytes, resulting in cell potentials of 0.34V, 0.40V and 0.65V respectively.

3.1.3 Determining State-of-Charge

Since the efficiency calculations include the theoretical cell voltage at a certain SOC, the SOC should be determined accurately. In this work, UV-Vis spectra are used for this purpose. The UV-Vis absorption spectra for varying state of charge of a $[Fe(CN)_6]^{3/4-}$ electrolyte are shown in figure 3.4 (solid lines), to establish a trend. The dashed red line shows the absorption spectrum of the ferri-/ferrocyanide after charging.

In table 3.1, the SOC after photo-charging for the different electrolytes and photo-electrodes are shown. The theoretical SOC is determined using the accumulated input charge, as shown in equation 2.37. The second method, utilizing the UV-Vis absorption spectrum of the charged electrolyte, is used as verification, using the trend-line in figure 3.4. Note that the higher absorbance relates to lower SOC when considering the photo-cathodic ferri-cyanide conversion, while it corresponds to higher SOC in the case of the photo-anode. It is seen that although the two methods give similar results, the UV-Vis method gives (slightly) different results in general.

This can be explained by ion-crossover effects, where $Fe(CN)_6^{3-}$ crosses over to the other compartment (as seen in the appendix), resulting in lower UV-Vis peaks. Therefore the estimation using the theoretical accumulated charge, overestimates/underestimates the SOC, depending on which species is used at 0 SOC ($Fe(CN)_6^{3-}$ or $Fe(CN)_6^{4-}$). Moreover, side reactions, such as Prussian Blue formation, result in similar discrepancies. It is seen that experiments with lower volume (the first TEMPO and second Cu row in table

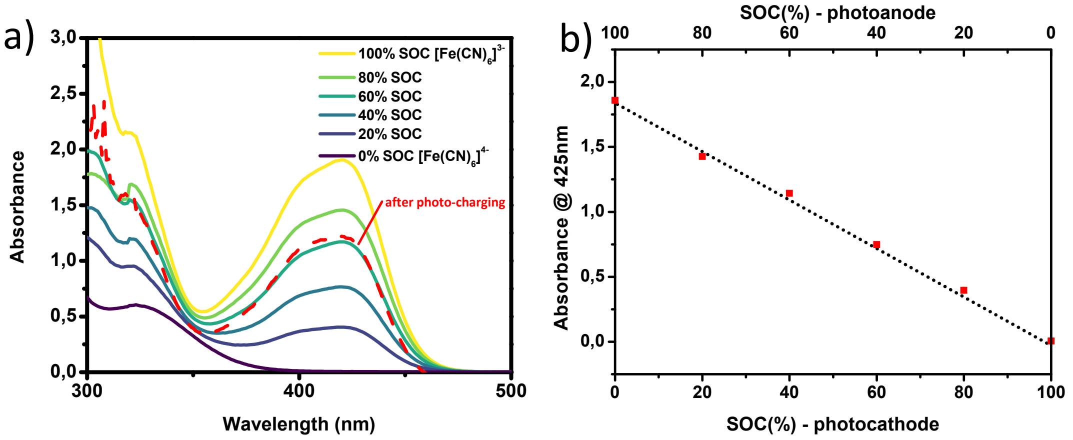

Figure 3.4: a) UV-Vis trend of the absorption spectra for ferri-/ferrocyanide at the varying state of charge (solid lines) and example absorption spectrum of one of the electrolytes after photo-charging, used to estimate the SOC after charging. b) Absorption at the characteristic peak of ferri-/ferrocyanide @425nm. The linear trend line is used to estimate the SOC of an electrolyte after photo-charging.

Couples	V_{cell} @ 50 SOC (V)	Cell volume (mL)	SOC (theoretical)	SOC (UV-Vis)
$Fe(CN)_6^{3-}$/TEMPO	0.34	10	0.23	0.32
$Fe(CN)_6^{3-}$/TEMPO	0.34	25	0.16	0.18
$Fe(CN)_6^{4-}/Cu^{2+}$ short-term	0.4	25	0.10	0.09
$Fe(CN)_6^{4-}/Cu^{2+}$ long-term	0.4	15	0.69	0.63

Table 3.1: SOC after charging for the different photo-charging setups. It is seen that the two different methods of determining the SOC after charging (using the input charge and using the UV-Vis spectrum of the charged electrolyte) give similar results. Discrepancies are explained by the uncertainties in the UV-Vis method and the ion-crossover effect.

3.1), have more pronounced differences between the two methods since the discrepancies mainly arise due to the stability issues.

Although both methods of determining the state-of-charge are imprecise due to stability problems in the SRFB and theoretical assumptions, the two separate methods result in similar state-of-charge, fortifying their combined credibility.

3.1.4 Mott-Schottky-analysis

The results of the Mott-Schottky measurements are shown in figure 3.5. Analysis of the plots is used to determine any impacts these conducting layers may have on the band structure (e.g., due to Fermi level shift). In the bare Si case, obtaining reliable results is quite challenging due to surface deactivation due to silane or oxide formation in the electrolyte (figure 3.5b) as described in previous studies.[13, 41]. It is noteworthy that the surface of the Si was chemically cleaned upon any electrochemical analysis by using 3M H_2SO_4 solution in order to remove the native oxide layer. Using a highly acidic supporting electrolyte, such as HF, can provide a reliable environment for the measurement,[44] but one cannot avoid a toxic HCN formation due to unstability of the ferro-/ferricyanide in low pH conditions.[20]

In the case of the semiconductor/liquid junctions, E_{fb} is found to be 0.32 V for the TiO_2. These results imply that upward band banding within the solid phase at the equilibrium can form a Schottky barrier with

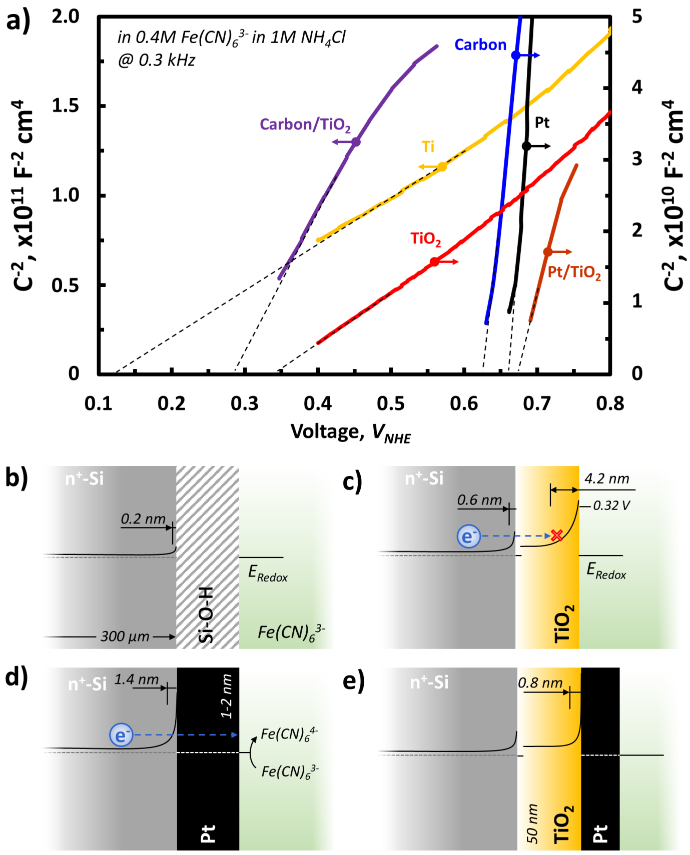

Figure 3.5: Mott-Schottky plots of prepared electrodes with various conducting layers measured at 0.3 kHz in 0.4 M $[Fe(CN)_6]^{3-}$ with 1 M NH_4Cl supporting electrolyte (a). Band alignment of the electrodes in the electrolyte (b-e) based on the Mott-Schottky measurement and calculation (detail calculation and material parameters can be found in the ESI of the original experimental paper, under submission).

a thick depletion width (4.2 nm, figure 3.5c) that electrons cannot tunnel through (detail calculation can be found in S3 of the ESI). In figure 3.5d and e the complete band diagram of the Pt conducting layer cases with and without the TiO_2 protective layer are schematically shown assuming an ohmic-like contact with very narrow depletion width of 1.4 and 0.8 nm within the n+-Si and TiO_2, respectively. Those assemblies allow a feasible electron transfer throughout the conduction band of TiO_2 and compact metal layer as illustrated. These feasible charge transfers were supported by the steep slopes of the Pt and TiO_2/Pt samples with onset potential (V_{on}) of ~0.5V vs NHE in figure 3.6b and c.

3.1.5 Photo-electrochemical charging performance

LSV measurements at 0% SOC under illumination were performed, using a three-electrode setup, for the half-reactions of ferri-/ferrocyanide reduction/oxidation, driven by the photo-cathode/anode, shown in figure 3.6b and d respectively.
It is seen that the onset potential is shifted with respect to the redox potential of the ferri-/ferrocyanide (of 0.48V vs NHE). For the photo-cathode (figure 3.6b) the onset potential of the Pt and C coated photo-electrodes (black and green) shifts towards ∼ 0.95V vs NHE, resulting in a photo-voltage of ∼ 0.47V. In case of the photo-anode, the onset potential shifted to ∼ 0 V vs NHE, resulting in a photo-voltage of ∼ 0.48V. The LSVs of half-reaction of the counter-electrolytes are overlapped with the photo-current in figure 3.6a and c. The intersection of the two curves is an indicator for the operating photo-current of the overall dual cell at 0% SOC.

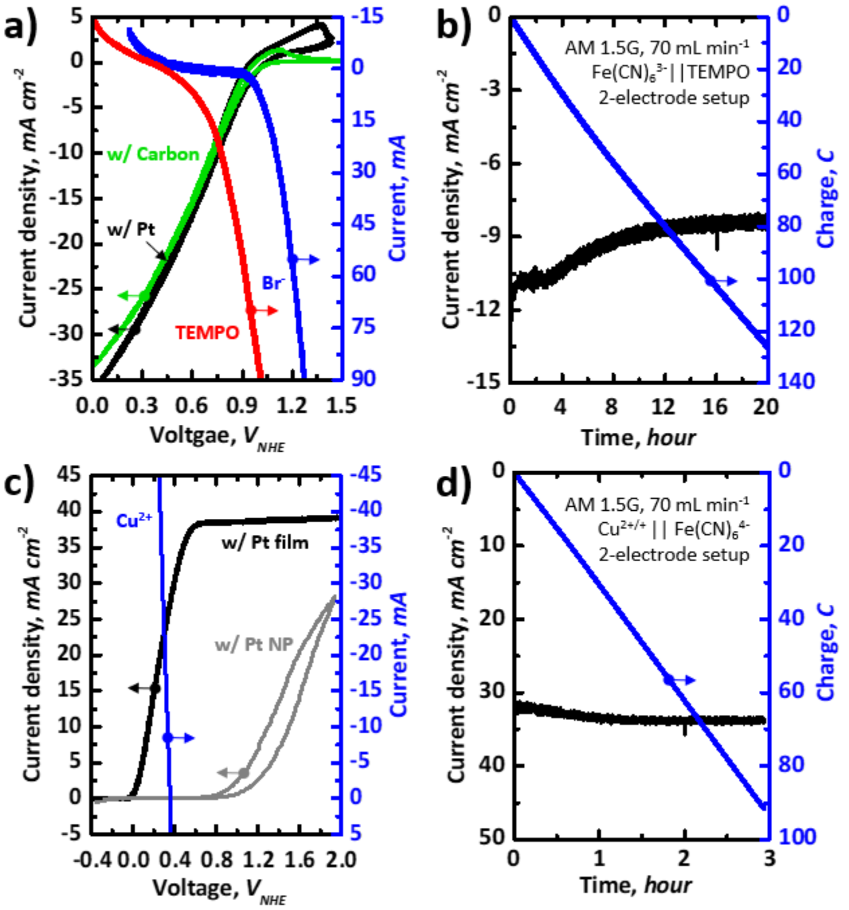

Figure 3.6: (a) Overlaid current-voltage curves measured in a three-electrode experiment for the individual photocathodes and anode (carbon felt). C/pn+-Si and Pt/pn+-Si in a 0.4M $Fe(CN)_6^{3-}$ + 1M NH_4Cl; while carbon felt anode in a 0.4M TEMPO- and 0.2M Br^- with an 1M NH_4Cl solution. (b) CA and accumulated charge of the photocathode with carbon, under the same electrolyte conditions, but with two-electrodes configuration. (d) Overlaid current-voltage curves (three-electrode configuration) for the individual photoanodes and carbon felt cathode. The pn+-Si photocathodes with a Pt thin film (1-2 nm) and Pt nanoparticles (200 ng cm-2) and carbon felt cathode for 0.4M Cu^{2+} in the same electrolyte condition used for the figure (c). (d) CA and accumulated charge of the photoanode with Pt with carbon felt anode under two-electrode configuration.

figure 3.6b illustrates the photo-charge profiles for the first 20 h using a C/np+-Si||Carbon-rod configuration with ferricyanide||TEMPO-sulfate. The charging photocurrent for the photocathode starts at 11.6 mA cm-2 and decreases to 8.7 mA cm^{-2}; the corresponding initial and final values for the ferricyanide||Br2/Br- cell are 2.0 and 0.4 mA cm^{-2}, (also seen in figure 3.7). In both photo-charging experiments, the photocurrents decrease over time, owing to the increasing cell potentials at higher SOC. Theoretically 0.51 V from the photocathode is insufficient to charge the ferricyanide||Br2/Br- battery without a bias potential. The low photo-charging current from the ferricyanide||Br^2/Br^- cell is only observable at low SOC% where required potential is low according to the Nernst equation.

In figure 3.6d, the same photo-charging curve is displayed for the ferrocyanide/Cu^{2+} dual cell configuration, using the photo-anode. A high photo-current of $\sim$ 33 mA/cm^{-2} is seen during the first three hours of charging. After the photo-charging experiments, UV-Vis measurements (discussed in section 3.1.3) were conducted to estimate the state of charge and verify the theoretical SOC, based on the inputted charge as seen in figure 3.6c and e.

The CA-data for the examined counter-electrolytes for the ferri-/ferrocyanide is shown in figure 3.7, for the backside-photoanode (BPA) and the C/np+-Si back-side photocathode (BPC) respectively.

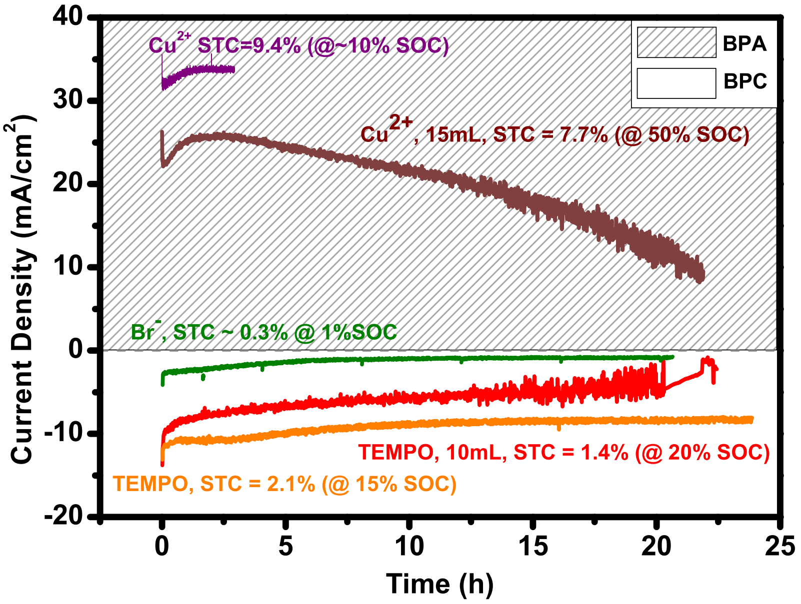

Figure 3.7: Chrono-amperometry-data of the long-term photo-charging experiments using the various electrolytes. When not mentioned, the electrolyte volume was 25 mL in each chamber.

The photo-charging performance varies significantly for the different electrolyte configurations. It is seen that the cell coupled with Br^-, has a low STC efficiency (∼0.3%), due to the high cell voltage at 50% SOC (0.65V), resulting in low photo-currents, and only at SOCs close to 0%.
The TEMPO and Cu^{2+} batteries have high performance due to the more favorable cell voltages at 50% (0.34V and 0.4V) respectively as confirmed in the modeling work in section 3.2.
The general trend of photo-current decreasing with time is explained by the increasing cell voltage due to increasing SOC, following the Nernst equation 2.17. Following the IV-curve of an illuminated PV-module (such as shown in figure 2.4), higher (cell) voltages always yield lower photo-current. This effect is most evident in the long-term, small-volume photo-charging experiments in figure 3.7.
It is also seen that higher volume of electrolyte, results in higher photo-currents in the case of the TEMPO and Cu^{2+}. This can be attributed to the lower series resistance, associated with the higher number of available paths for charge transfer since the distance between the electrodes is identical in every setup.

3.1.6 Front-side vs Back-side illumination

In figure 3.8, LSV measurements are shown for front- and backside-illuminated setups. The experimental

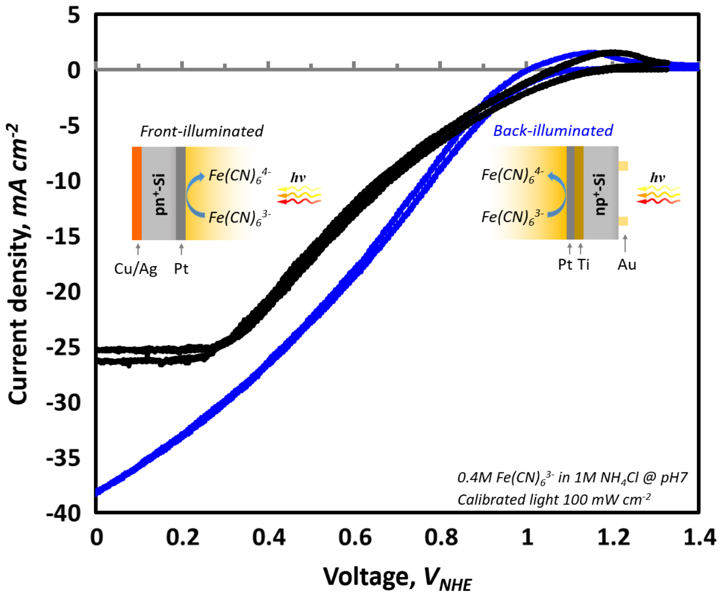

Figure 3.8: The experimental LSV curve shows that in case of a 0.4M ferricyanide electrolyte, a front-side illuminated configuration results in a significantly lower saturation photo-current, which concurs with the modeled trends.

LSVs in figure 3.8 support the modeled trends of the expected higher photo-currents (and thus efficiencies) for a back-illuminated configuration (see figure 3.10). The saturation current of the front-side illuminated device is significantly lower than the back-illuminated case, despite an otherwise almost identical setup.

3.2 Modeling

The objective of the modeling work is to estimate PEC redox flow battery performance, for which the solar to chemical (STC) efficiency is used as an indicator. When varying the cell voltage (i.e., thermodynamic potential to drive the redox reaction, defined at 50% SOC)) as well as the band-gap of the photo-absorber, a 2D contour-plot of the STC efficiency is obtained. This format will be used to assess several parameters. In figure 3.9, the ideal case is shown, in which no losses, for instance, due to parasitic light absorption, reflection or resistances are taken into account. The dark saturation current is calculated using the ideal black-body emission theory, expressed in equation 2.4. It is found that the theoretical maximum STC efficiency for a single-photo-absorber device is 32.4%, which concurs with literature estimations for PV solar cells.[45, 46]. However, the SRFB system allows a wider operational range than that of the PEC water splitting system which has a fixed thermodynamic energy barrier for driving the redox reaction (i.e., water oxidation at 1.23 V). The top left of the plot shows no efficiency data, due to the limited photovoltage with respect to E_{redox}. When moving towards higher bandgap energy, the STC% is limited by the number of incoming photons with an energy higher than E_g. This figure indicates that there is an optimum thermodynamic potential depending on the band-gap of the absorber material, and finding this optimum could drastically enhance the solar charging performance of SRFBs.

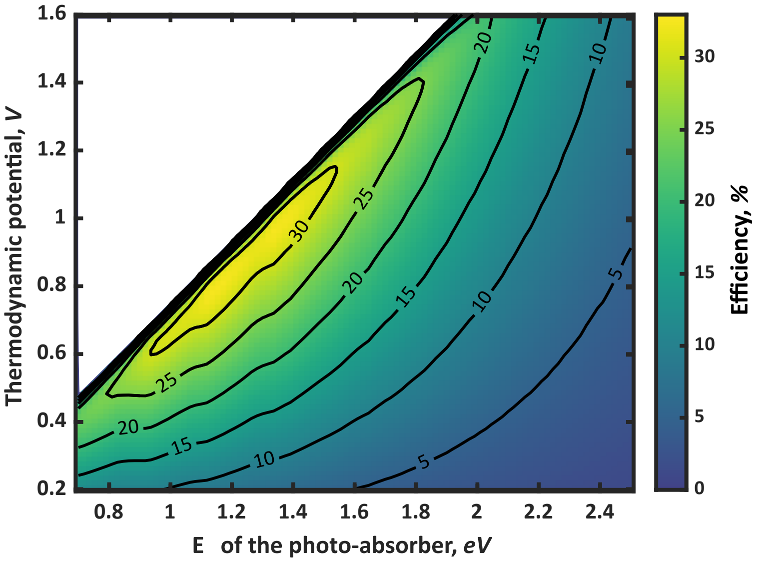

Figure 3.9: Efficiency plotted as a function of the thermodynamic potential and the bandgap of the photo-absorber in the ideal case without any kinetic, resistance, or parasitic light absorption/reflection losses.

3.2.1 Sensitivity on Losses

In this section, the effects of several of the discussed losses are shown on the ideal efficiency landscape, including parasitic light loss, series (and electrolyte) resistance, kinetic overpotential and SOC effects.

3.2.1.1 Parasitic light loss

In figure 3.10a and b, the effect of parasitic light absorption by the electrolyte $[Fe(CN)_6]^{3-}$ and V^{3+} (in 1M NH_4Cl and HCl, respectively) is shown for a concentration of 0.3M and path length of 1 cm. These figures mimic the working environment of a PEC compartment where the photo-electrode is directly immersed in the electrolyte. As shown in these figures, the maximum STC% decreases to 27.2% and 17.2% for the $[Fe(CN)_6]^{3-}$ and V^{3+} respectively. Moreover, the shape of the efficiency-landscape changes depending on the exact absorption spectrum of a given electrolyte (see also figure A.1 in the appendix for the AQS/$AQSH_2$ and

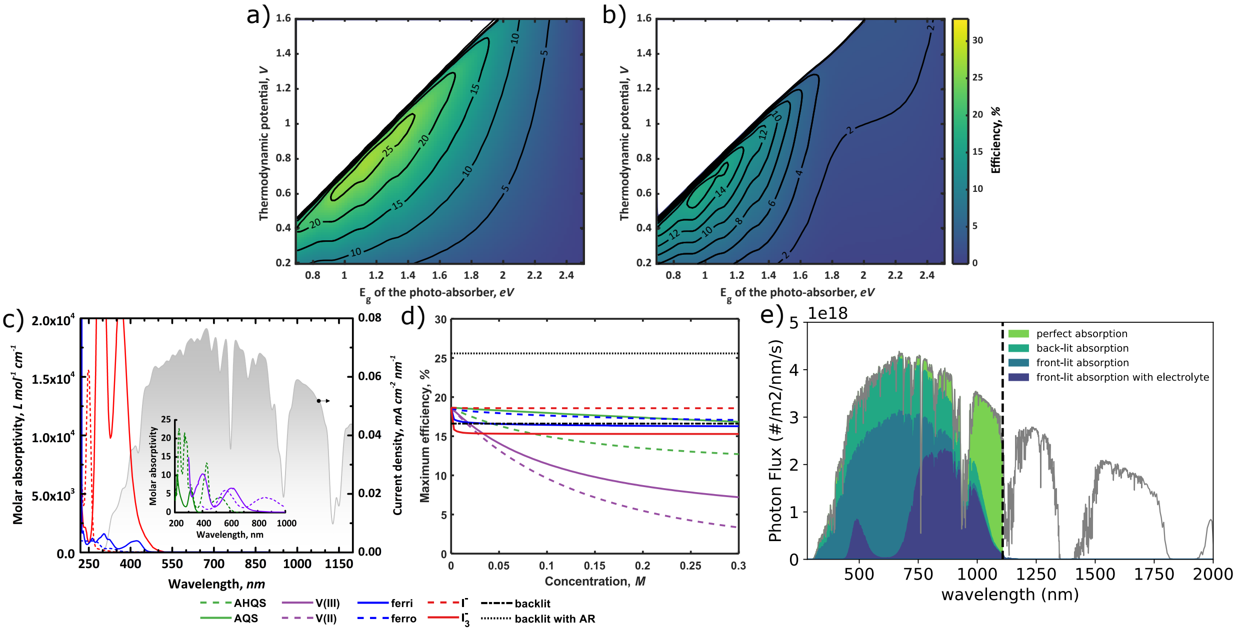

Figure 3.10: Efficiency plotted as a function of the thermodynamic potential and the bandgap of the photo-absorber. In a) and b), the reflection from the window and parasitic light absorption of 0.3M ferricyanide and V^{3+} (with an optical path length of 1 cm) respectively are taken into account. Kinetic and resistance losses are not considered. c) Experimental absorption spectra of several electrolytes overlapped with the photon flux of the AM1.5 spectrum (depicted by the shaded area). d) The concentration dependence of the maximum efficiency for a 350 μm c-Si photo-absorber. e) schematic overview of the parasitic light losses and their influence on solar absorption. Figure adapted from original paper [20]

I-/I3- cases). This makes finding the optimum E_{redox}/E_g combination extensively more complex. In figure 3.10c, the experimental absorption spectra, based on literature [47, 48, 49] and experimental measurements, are overlapped with the photon flux (in current density) converted from the standard AM1.5 spectrum, showing the impact of electrolyte selection on the incoming solar spectrum. Note that this result does not take into account the individual effect of the supporting electrolyte since there is no significant loss up to 10 cm of water thickness in the case of a single-photon device.[50] Overall, the reduced incoming-photon flux shifts the optimum E_{redox}/E_g combination towards a smaller value that requires an electrolyte with a high concentration for balancing the discharging capacity.

Another effect differentiating between the efficiency of the back- and front-side illumination configurations is the possibility of introducing an anti-reflective treatment (e.g., AR coating). In the case of the electrode being submerged in the electrolyte, some corrosion protective layers for photo-electrodes (e.g., TiO_2 with c-Si) show anti-reflective properties, however, typical AR treatments, such as MgF_2 and SiO_2 layers, are not applicable in this case due to their stability which is pH-dependent.[13] To account for this, the reflectance spectrum of c-Si with and without an AR coating is used for modeling the back-illuminated efficiency, while the (complex) refractive indices of air, glass, electrolyte and bare silicon are used to model the front-illuminated efficiencies. As shown by the dash-dot line in figure 3.10d, almost 8% efficiency loss is expected in the case of bare c-Si indicating the importance of having an AR treatment to minimize reflection losses. It is interesting to note that the back-illuminated bare c-Si case shows slightly lower charging efficiency than the front-illuminated cases in the low concentration range. According to the Fresnel equation (equation 2.20), the higher refractive index of the electrolyte with respect to air leads to a reduced reflection of bare silicon for a front-illuminated configuration (also see figure A.2 in the appendix) with respect to back illumination, resulting in higher efficiencies in the cases where this effect is more dominant than electrolyte absorption.

In figure 3.10e, the extent of each parasitic light-loss effect on the photo-absorption of a silicon PV-cell, where in case of perfect absorption all photons with $E < E_g$ are absorbed. It is seen that back-lit absorption (taking into account realistic silicon absorption spectra and reflection based on AR-treated silicon) already loses a significant portion. Front-lit absorption without taking into account electrolyte absorption has even lower photo-absorption due to the inability to apply an anti-reflective coating. When including parasitic electrolyte absorption, the advantage of back-lit over front-lit configurations becomes evident. The concentration dependence of the electrolyte on the STC% in figure 3.10d highlights that conventional vanadium-based redox couples with a front-illumination architecture cannot be considered as an efficient charging method for a high storage capacity system (i.e. high concentration) due to their high molar absorptivity in the high wavelength range (see inset of figure 3.10d). On the other hand, the STC% with iodide electrolyte is relatively less sensitive to the concentration while it showed a drastic molar absorptivity in the short wavelength region (figure 3.10c). This absorption spectra study is particularly important for the wide bandgap semiconductor-based device. For instance, GaP (2.24 eV) has a large absorption spectrum overlap with AQS electrolyte, leading to a drastic drop in $j_{ph,max}$ upon the addition of the AQS into H_2SO_4.

3.2.1.2 Kinetic overpotential

as the electron transfer between the photo-absorber and the electrolyte is never perfect. In general, an RFB presents facile kinetics, which can be several orders of magnitudes faster than water oxidation that requires high overpotential.12 In figure 3.11a and b, the effects on the efficiency-landscapes with fixed kinetic overpotentials (η_k) of 0.2 V and 0.6 V respectively are shown.

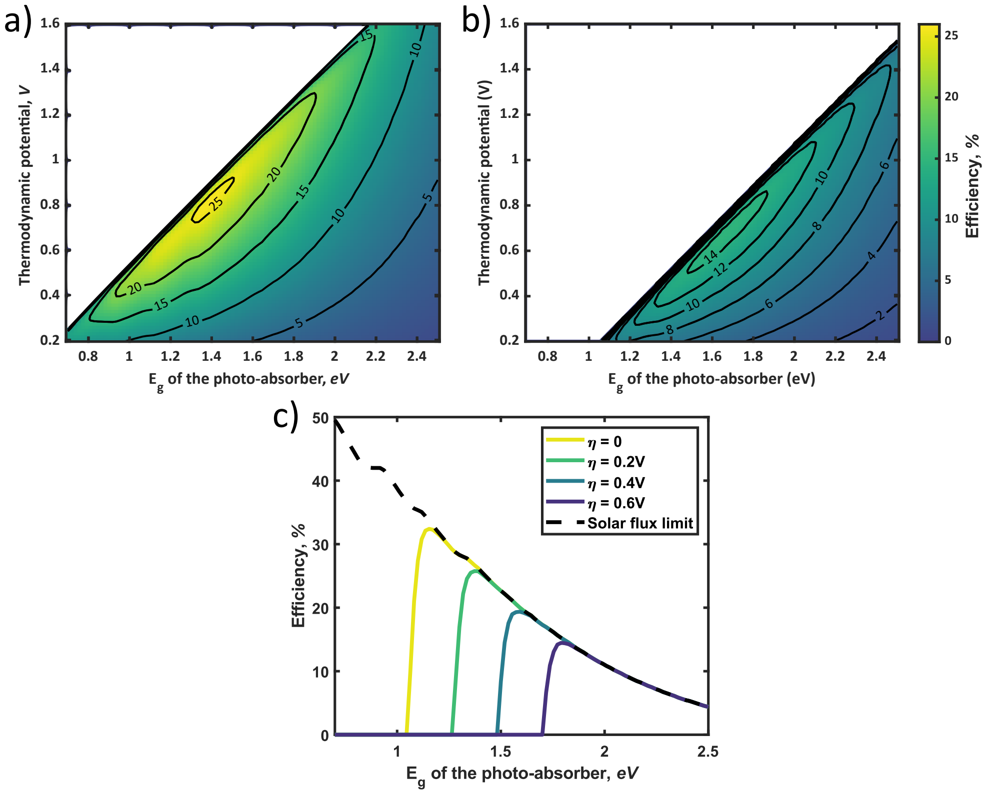

Figure 3.11: Efficiency plotted as function of the thermodynamic potential and the bandgap of the photo-absorber. a and b show the effect of 0.2V, 0.6V kinetic overpotential respectively. In c the STC% is plotted as function of the bandgap-energy for various overpotentials. The dashed black line shows the maximum theoretical efficiency based on the AM1.5 spectrum. Figure adapted from original paper [20]

First, it can be seen that the maximum STC%, as opposed to the previous electrolyte concentration-effect case in figure 3.10a-c, shifts to higher E_g and lower E_{redox}, due to the kinetic overpotential effectively increasing the voltage needed to drive the reaction (equation 2.25). Moreover, owing to the shift of the contour-plot to higher bandgap energies, the STC% decreases due to reduced absorbed solar flux (as shown more clearly in figure 3.11c). An important aspect is the selection of a conducting material at the solid/liquid interface. Conventionally, high overpotentials arise from the photoelectrode while the counter electrode shows quite fast kinetics. The experimental linear sweep voltammograms (LSVs) of n-type Si electrodes under dark conditions shown before in figure 3.1 shows how the overpotential varies with the type of conducting layer, stressing the importance of modeling kinetic overpotentials for accurate performance estimation. Unlike typical RFB systems where the metallic electrodes or carbon are directly connected to a wire, SRFBs require integration of semiconductors with the conducting layer that may form an energy barrier with unfavorable band-bending at the semiconductor/metal junction.

Note again the model used, implies that the overpotential of the counter-electrode (typically a carbon felt/rod electrode), is negligible since its surface area is much larger than the photo-electrode. This assumption is verified experimentally and is shown in figure B.1 in the appendix.

3.2.1.3 Series resistance

figure 3.12a and b display effects of overpotential and series resistance, respectively, on the photo charging efficiency landscape for the c-Si case ($E_g = 1.12$ eV). The dashed lines represent the efficiency curves for which surface reflection and shading by the front contact grid (i.e., the dead area of 4% of the total active area [51]) are taken into account. Note that the series resistance consists of the sum of the electrolyte resistance, the membrane resistance and the internal series resistance of the PV-module

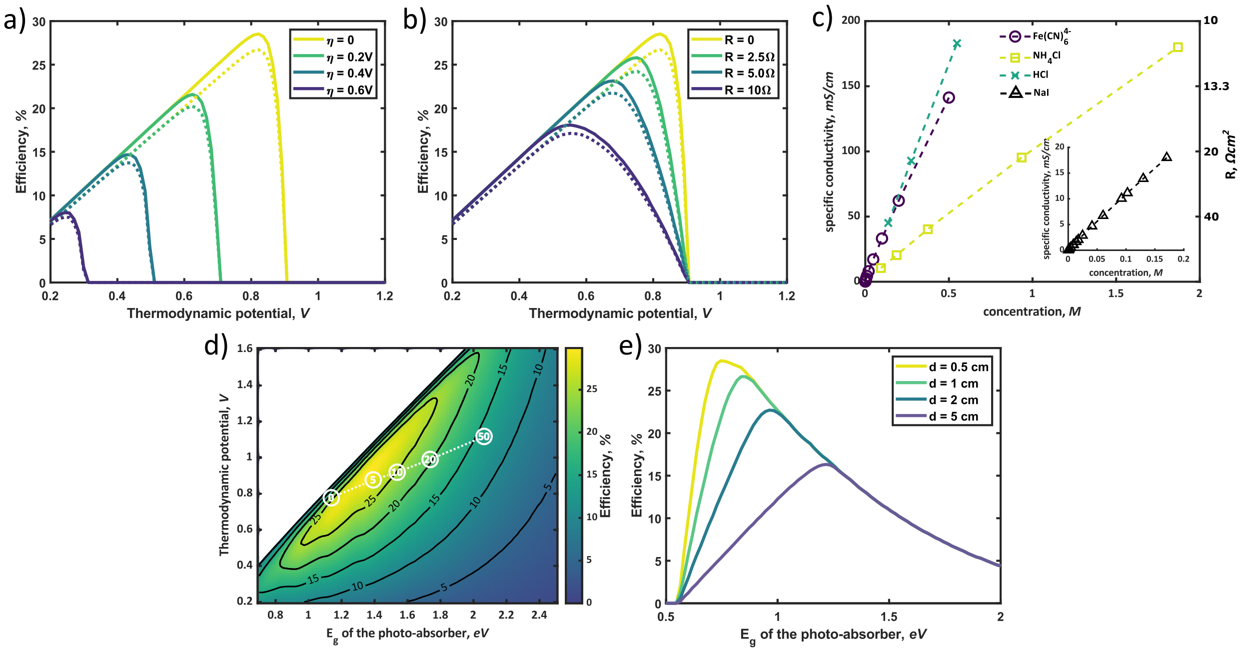

Figure 3.12: Sensitivity analysis for each type of loss. The charging efficiency is plotted as a function of the thermodynamic potential in back-lit configuration for different kinetic overpotentials (a) and solution resistance (b), respectively. The dashed line represents the case in which surface reflection (by AR treated silicon) and contact shading are taken into account. Data found in literature for the specific concentration is plotted versus concentration for various electrolytes (c). In (d), a contour-plot of the efficiency landscape for an electrolyte resistance of 2.5 Ω·cm^2 is shown. The white circles indicate the optimum location (i.e., the optimum bandgap-thermodynamic potential combination) for electrolyte resistances of 0, 5, 10, 20 and 50 Ω·cm^{2}2 respectively, showing a shift towards higher bandgap and higher thermodynamic potential for increasing resistance. The same trend is observed in (e), where the STC% is plotted versus the photo-absorber band-gap at a thermodynamic potential of 0.8V, for the varying distance between the electrodes, effectively increasing the electrolyte resistance. Figure taken from original paper [20]

Interestingly, the efficiency loss due to the reflection and shadowing in case of a photo-absorber with appropriate treatment (i.e., AR and optimized front grid) is limited. Figure 3.12 is a sensitivity analysis plotted against the thermodynamic potential. Naturally, it shows a similar trend as that found in figure 3.11c for overpotential variation; an increased overpotential greatly diminishes performance limit and threshold cell voltage (i.e., the potential differential between the catholyte and anolyte). As mentioned earlier, electrolyte resistance (R_{sol}) is one of the dominant contributors to the overpotential, and the plots in figure 3.12b were obtained from the calculations with various resistance overpotentials at zero kinetic overpotential.

The figure 3.12b shows a relatively low sensitivity of the STC% to the electrolyte resistance variation. While a negative shift of the optimum thermodynamic potential is seen along with a solution resistance increase, the threshold potential below which achievable STC% is observed remains almost constant. The solution resistance is often a significant factor in practical working conditions where ionic transfer pathways are on the order of centimeters. Generally, the resistance of an ionic solution depends on the ionic concentration, type of ions, temperature, and the geometry in which current is carried. This is made evident in figure 3.12c, where the conductivity of the electrolytes is highly dependent on electrolyte type and its concentration. For example, a system with a 1M NH_4Cl supporting electrolyte and an estimated conductivity of 75 mS/cm for the redox electrolyte, the total electrolyte resistance for a 2 cm path length (e.g., 1 cm each for catholyte and anolyte) is 11.35 $\Omega\cdot cm^2$ (see section A.3 in the appendix for explicit calculations), implying that the impact of the electrolyte resistance should not be neglected in practical models. The plots for the various electrolytes in the figure 3.12c were calculated based on data found in literature,[52, 53, 54, 55], where the measurements were conducted under precisely controlled conditions (e.g., temperature, electrode distance, purification treatment, etc.). As demonstrated in figure 3.12c, it is relatively easy to reduce the solution resistance simply via concentration control, whereas a reduction in kinetic overpotential requires careful conducting materials selection along with electrical and morphological design to provide sufficient conductivity and active sites over the whole surface.

As shown in figure 3.12d, the optimum point shifts towards lowered E_g with decreasing solution resistance (white circles). In the extremely low solution resistance case, a lowered optimum point (E_g of 1.2-1.6 eV with E_{cell} of ~0.6-0.9 V) makes the use of commercial PV materials (e.g., c-Si, CIGSe, GaAs)[13] promising. However, the high ionic strength condition may potentially lead to corrosion of the materials, which will most likely require an additional protection layer. For instance, solution resistance of 2.5 $\Omega\cdot cm^2$ corresponds to highly acidic supporting electrolytes (e.g., a 3M HCl solution). These extremely harsh conditions are not practical considering that most studies in the PEC water splitting field have been conducted in the pH range of 0~14, and still suffer from poor long term stability.[13] Alternatively, minimizing the distance between the electrodes also can be an option to decrease solution resistance. Figure 3.12e plots the STC versus the photo-absorber band-gap for which the distance between the electrodes decreases in magnitude, showing that a shorter electrode-electrode distance leads to a shift of the optimum band-gap towards lower values with a higher overall conversion efficiency. Again, we emphasize that this theoretical estimation has been conducted without consideration of possible photo-redox effect under the assumption that electrolytes are completely isolated from the light due to the back-side illuminated architecture (e.g., figure 2.16a).

3.2.1.4 SOC

In general, the standard redox potential (E^0_{redox}), is defined at 50% state of charge (SOC), but SOC-dependent changes in the cell voltage according to the Nernst equation (equation 2.17) should be taken into account for optimizing an SRFB.

Figure 3.13 displays the maximum practical STC efficiency for a set of parameters: $R_{sol} = 2.5\ \Omega\cdot cm^2$ (corresponding to a highly conductive, but usable electrolyte with optimized path length ~ 1 cm), an internal series resistance of 3 $\Omega\cdot cm^2$, η_{redox}=0.25V, a constant parasitic light loss at the photo absorber of 5% and a contact shading of 4% of the active area. This is done for 10% and 90% SOC to show the effect of charging on the efficiency landscape (figure 3.13a and b, respectively).

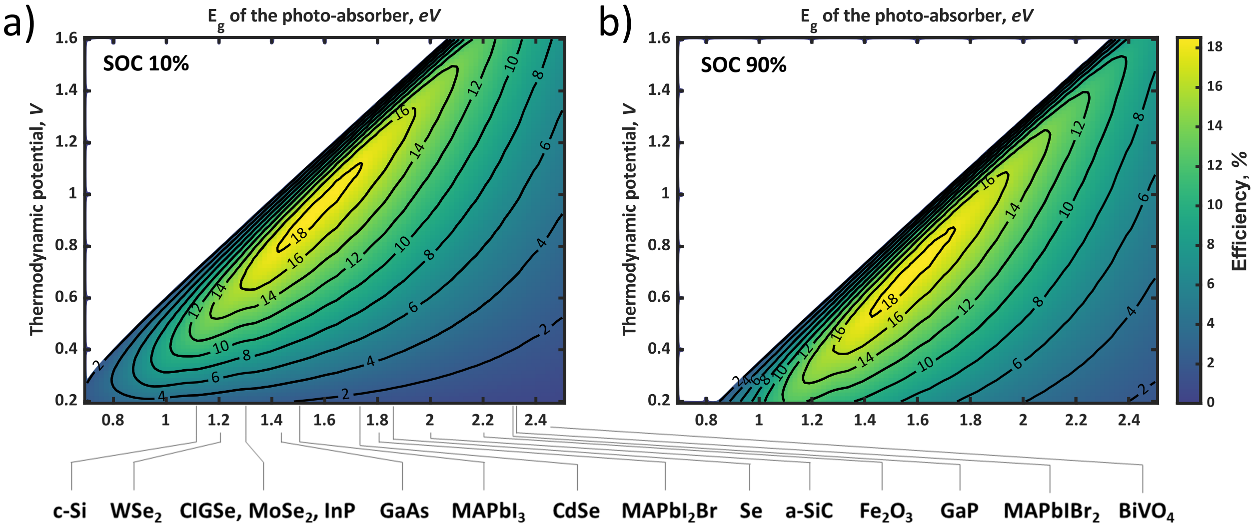

Figure 3.13: The efficiency landscape for a realistic set of parameters: R_{sol}=2.5 Ω·cm^2, η_k=0.25V with a constant parasitic light loss at the absorber of 5%, a contact shading of 4% of the active area, an internal series resistance of 3 Ω·cm^2 and a 10% SOC (a) and the same plot for similar parameters, but with an SOC of 90% (b). Both plots assume a back-lit configuration. Several photo-absorbers are indicated in (a) to point out the possibilities in choosing an optimal photo-absorber. Figure taken from original paper [20]

These plots highlight a shift of the entire STC shape towards a lower thermodynamic potential due to the potential polarization in accordance with the Nernst equation (equation 2.17). It is expected that an STC% of 16% can be obtained if the band-gap of the absorber material is within 1.6-1.8 eV and the thermodynamic cell voltage is around 0.9 V and 0.7 V for the SOC of 10% and 90%, respectively.

3.2.2 Temperature dependence

The temperature dependence of SRFB-operation might open doors towards higher performance through temperature optimization. Therefore, the modeled IV-curves for dry photo-voltaic silicon semi-conductors under illumination for a range of temperatures are shown in figure 3.14a). Note that for these simulations, the real absorption spectrum of silicon is used. It is seen that higher temperatures result in lower open-circuit voltages, due to higher recombination rates. Simultaneously, the maximum photo-current increases slightly due to higher photo-absorption, which in turn is caused by increased thermal fluctuations. These effects are well established in literature. [56, 57, 58]
However, as seen in equation 2.14, electrochemical reaction kinetics tend to improve with increasing temperature. In figure 3.14b), the IV-curves of an illuminated half-cell for a reaction with sluggish kinetics are shown. The parameters found by Haussener et al [31] for E_a and $j_{0,ref}$ are implemented to determine the temperature dependence of the kinetics (these parameters represent the oxygen evolution half-reaction). Due to the slow kinetics, the overpotential is a highly dominant loss factor in this device. Increasing the temperature, as shown in figure 3.14b), therefore increases the photo-current at high voltages (due to the decreased overpotential), despite the decreasing open-circuit voltage of the PV module.

In figure 3.15, it is seen that the IV-curve dependencies on temperature in figure 3.14a) and b) result in different efficiency trends with respect to temperature.

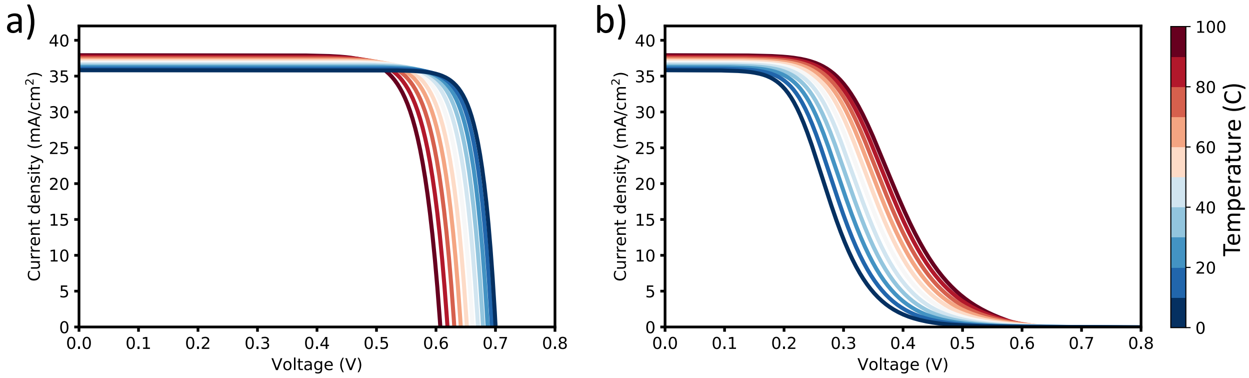

Figure 3.14: Temperature dependent current voltage characteristics of a silicon photo-absorber, modeled using its real temperature-dependent absorption spectrum[59] and realistic recombination rate, as calculated based on the absorption spectrum, in the paper by Tiedje and Yablonovic [26]. In a), no kinetic losses are taken into account, effectively showing the dry semi-conductor IV-curves under temperature variations. In b), the highly dominant kinetic overpotential losses of the oxygen evolution reaction are taken into account, which decrease strongly with increasing temperature.

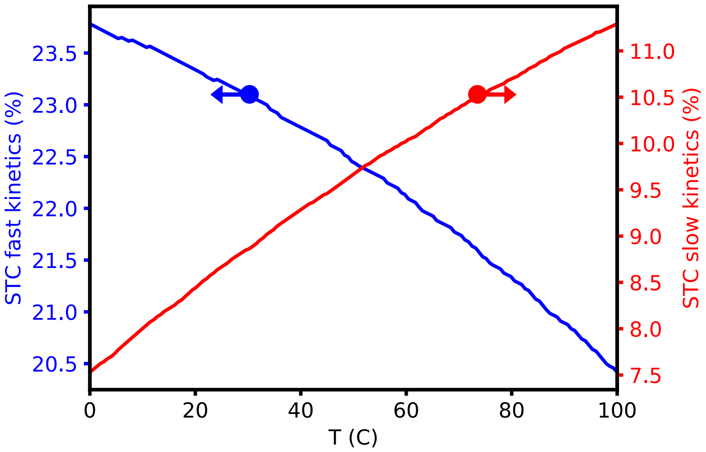

Figure 3.15: Modeled STC plotted versus temperature in case of redox reactions with a negligible catalytic loss and thus fast kinetics (left axis) and dominated by catalytic loss, meaning sluggish kinetics (right axis), using the example of HER and OER kinetics respectively. It is seen that the efficiency trends depend strongly on the type of reaction, as increasing temperature can either enhance, or decrease device performance.

In case of negligible kinetic overpotentials (the blue curve in figure 3.15 is made using the parameters of the rapid hydrogen evolution reaction, or HER), the performance decreases with temperature, due to the higher recombination as seen in figure 3.14. However, reactions in which the kinetic overpotential is the dominant effect (such as the OER used in figure 3.14b), performance improves as shown by figure 3.15. This is due to the temperature enhanced kinetics outweighing losses in the PV module.

3.2.3 Daily and seasonal variance

As seen in section 3.2.2, temperature has a significant impact on PEC flow battery kinetics. The seasonal dependence of the ambient air temperature, shown in figure 3.16, stresses the importance of the temperature-dependent performance of PEC-flow batteries [60]. Therefore, this section focuses on the daily and seasonal fluctuations and their consequences with respect to SRFB design principles.

When using the heat balance method in section 2.4.2, the photo-absorber temperature can be calculated

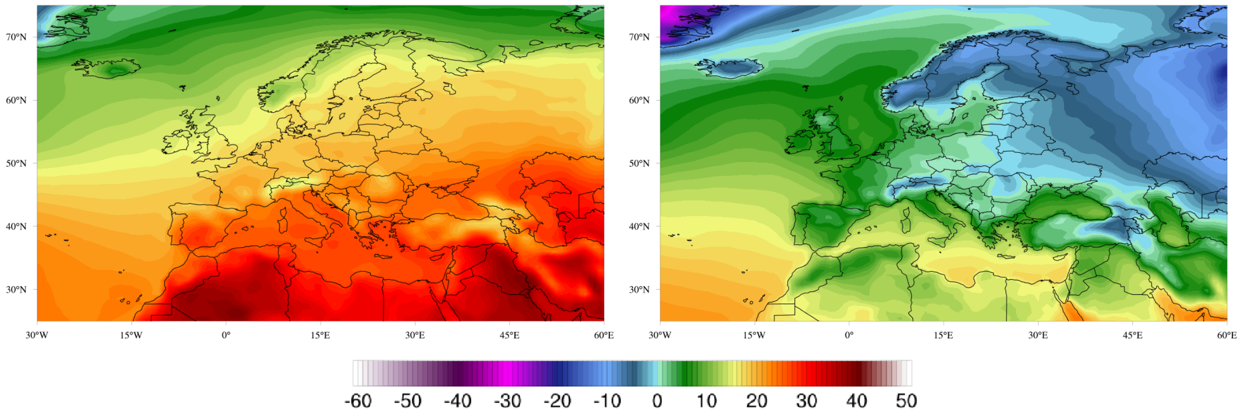

ClimateReanalyzer.org | Climate Change Institute | University of Maine

Figure 3.16: Temperature at 2m averaged from 2007-2017 [60] in July (left) and in December (right), providing motivation to conduct further research into temperature dependent PEC-flow battery performance, due to the significant temperature difference.

using three separate scenarios, to highlight the impact of the electrolyte in contact with the photo-absorber, on the temperature as well as on the STC. The first scenario is extreme: no convective heat transfer with either the ambient air or the electrolyte is assumed. In the second case, convective heat transfer with the air is included, which is comparable to a dry PV scenario. In the third case, the impact of a cooling electrolyte is shown as well.

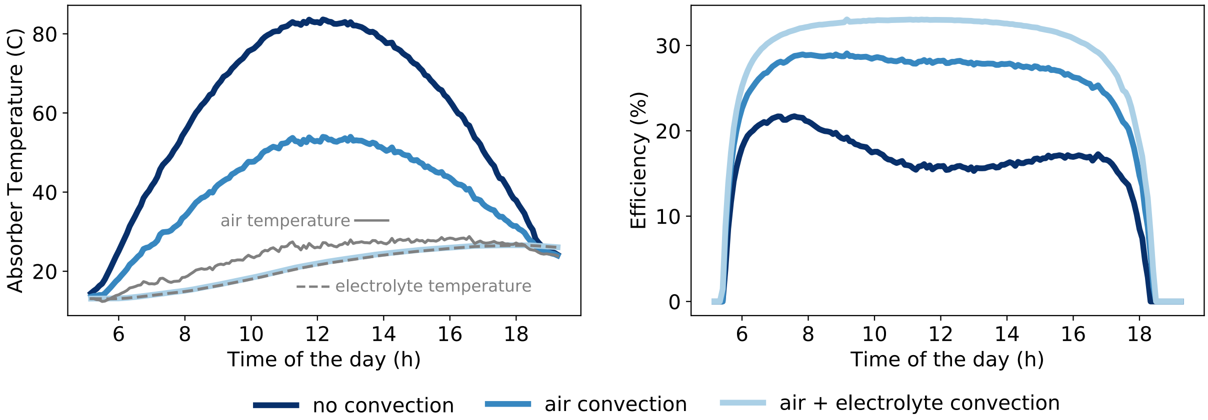

Figure 3.17: Absorber temperature (a) and STC% (b) over the course of a sunny summer day (31/07/2018), using the NREL data [37] for the three convective scenarios. The photo-absorber used is silicon, only considering ideal blackbody-emission and neglecting all other losses. The expected trend of lower photo-absorber temperature, with increasing convective heat transfer is seen in (a). (b) shows a strong increase in device performance (STC%), with increasing convection.

In figure 3.17a), the calculated photo-absorber temperature is plotted over the course of a day (31/07/2018), using the detailed data from the National Environmental Research Laboratory in Lakewood, Colorado[37], in case of the three proposed scenarios. It is seen that the photo-absorber temperature rises and falls with time as expected, due to the varying solar intensity and reaches >80C in the case of no convection. When considering convective heat transfer with respect to the air (~ 20 W/m^2/K), photo-absorber temperature follows the air temperature more closely as expected. The electrolyte temperature is seen to follow the air temperature with a delay, due to its high specific heat. When convective heat transfer between the absorber and the electrolyte is considered as well (~ 1000 W/m^2/K, meaning much more effective heat transfer), the

absorber temperature almost perfectly follows the electrolyte temperature.
Due to the temperature dependence of the device performance (see section 3.2.2), the STC% differs for these three cases of convection as seen in figure 3.17. It is seen that the cooling effect of the electrolyte has a positive effect on the STC%.
It is noteworthy that ~3 iterations (necessary due to the circular dependencies of temperature and open circuit voltage) of temperature/V_{oc} calculations suffice for the solution to converge (as discussed in section 2.4.2).

Moving on to seasonal dependence, the model is used to see whether there are variations in optimal cell voltage (meaning optimal redox-couple matching) when looking at different seasons. In figure 3.18, the NREL spectral and ambient temperature data is used to calculate the average output power P_{out} versus cell voltage for a silicon semi-conductor module, averaged over the entire month of December and July respectively. The output power is also calculated using the AM1.5 spectrum for reference. It is seen that the optimal cell voltage (depicted as the dashed vertical lines), varies seasonally. This can be attributed to the significant seasonal temperature and incoming solar radiation variation at the measurement station in Colorado. The lower temperature in December results in higher open-circuit voltages when no significant temperature catalytic losses are assumed (see figure 3.14a). It is seen that the difference between the optima is smaller when considering a reaction with sluggish reaction kinetics (in case of figure 3.18, OER).

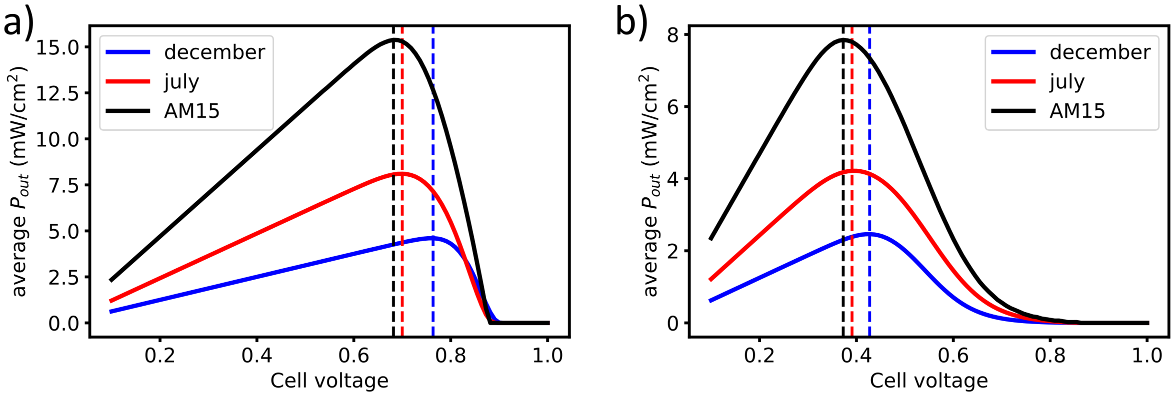

Figure 3.18: Averaged output power density (P_{out}) plotted versus cell voltage in case of no overpotentials (a) and in case of the OER kinetics (b) for the AM15 spectrum, the summer month July and the winter month December. The optima of the curves, depicted by the dashed vertical lines, shift significantly due to the monthly variation.

3.2.4 Dynamic SOC effects

Up until now, the state-of-charge is assumed to be static and with the exception of figure 3.13 is always assumed to be 50%. In practical terms, this means the capacity of the battery is assumed to be infinite. However, for batteries accounting for daily fluctuations, the state-of-charge varies considerably during the day. In figure 3.19, the output power is plotted over the course of a day, for practical batteries, charging from 5% to 80% on a sunny summer day for two different ΔE^0_{redox}. The dynamic SOC is implemented as described in section 2.4.3. The output power of the infinite battery at 50% SOC is plotted for reference.
It is seen that choosing different cell voltages 50% SOC (ΔE^0_{redox}), drastically changes the mean power output of the battery, when taking into account dynamic SOC effects, while the performance of 'infinite-capacity' batteries at these cell voltages are similar.
This problem can be mitigated by careful redox-couple selection, such that when accounting for a dynamic SOC, the output power still approaches the output power of a hypothetical battery with infinite capacity, as seen in figure 3.19b. The second possibility is careful battery capacity design. However, in this case, a

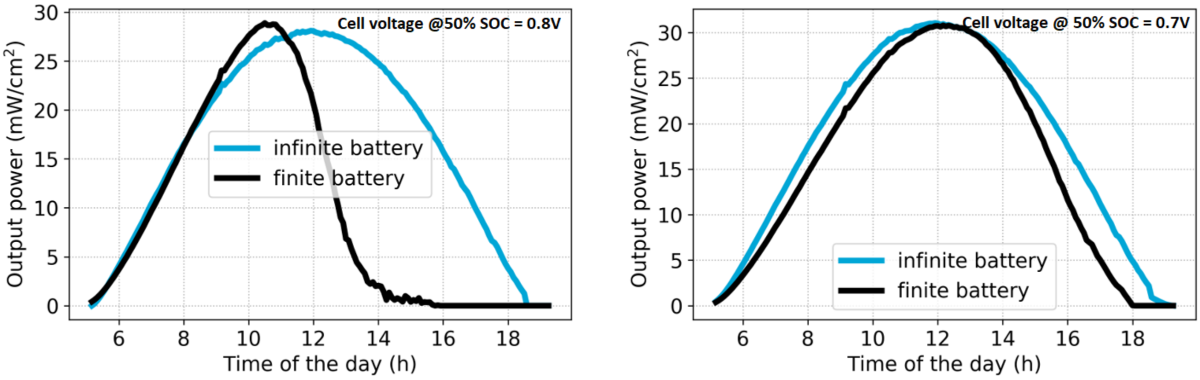

Figure 3.19: Modeled output power density versus time for an ideal silicon-based PEC flow battery at a thermodynamic potential of 0.8V (left) and 0.7V (right), comparing a finite battery, which dynamically charges to 80% during a day (black) and an infinite battery at 50% SOC (blue). It is seen that sensible redox-couple selection (effectively varying the thermodynamic potential), results in an output power curve, approaching the ideal case of an infinite capacity battery.

trade-off exists between optimizing charging efficiency and avoiding effectively unused electrolyte volume. Increasing the electrolyte volume enhances charging efficiency, but results in larger unused fractions of electrolyte (i.e. the battery is never charged/discharged to its full extent).

3.3 Comparing modeling with experiments

in the following two sections, the experimental results are compared with the modeled curves by means of the fit-tool, discussed in section 2.4.1 and by comparing the charging efficiencies (determined using the chrono-amperometry data in section 3.1.5) with modeled curves in section 3.3.2.

3.3.1 Fits

The dark electrochemistry results of figure 3.2 contain information on the losses in the system. Using the model described in section 2.4, excluding the photo-diode to mimic the dark-electrochemistry conditions and the numerical optimization, as described in section 2.4.1, the data is fitted to extract these losses. The fits are displayed in figure 3.20.

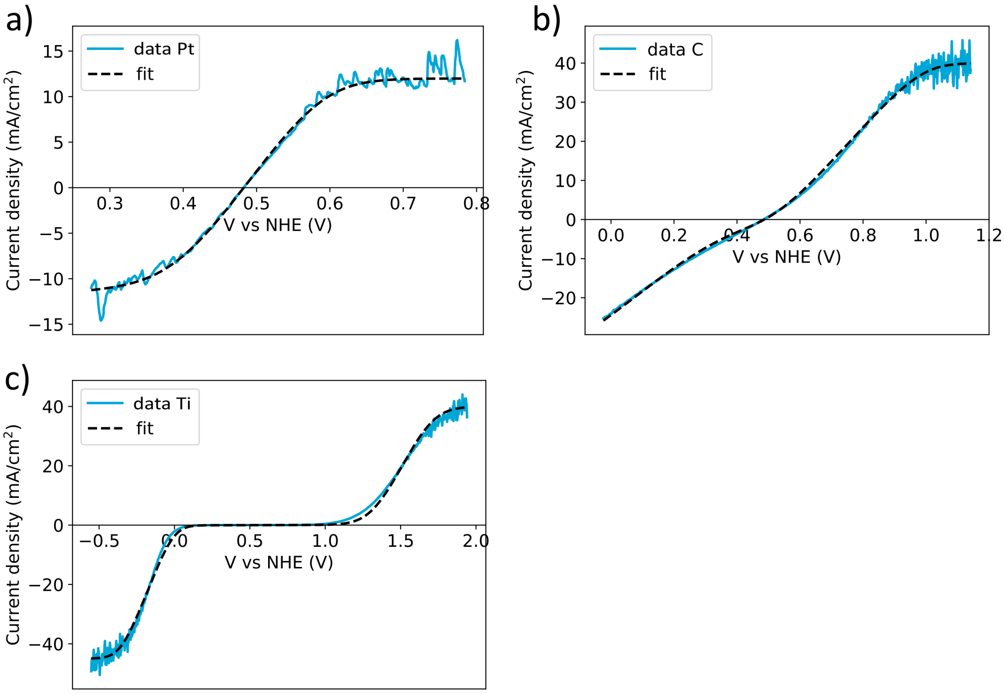

Figure 3.20: Dark electrochemistry fits of the experimental LSV curves obtained using n-type silicon coated with a platinum (a), carbon (b) and titanium (c) conductive layer respectively. The electrodes were immersed in a 0.2M $[FeCN_6]^{3-}$ + 0.2M $[FeCN_6]^{4-}$ (thus 50% SOC), added to a 1M NH_4Cl supporting electrolyte.

The results after fitting the dark experimental curves at 50% SOC are given in table 3.2. It is seen that the fits correspond qualitatively well with the experimental data, also reflected in the low quantitative errors as seen in table 3.2. This suggests the model used for the simulation of the electro-chemistry performance resembles the experimental setups for the dark electrochemistry experiments. Furthermore, it is seen that the platinum conducting layer exhibits the best kinetics and lowest series resistance. The fits for the IV-curves of the illuminated backside photo-cathode and backside photo-anode are shown in figure 3.21, whereas the fitted parameters are shown in table 3.3.

Note that for the BPA, the SOC is close to 0%, but not absolute, since the scanning starts from high voltages, already converting part of the electrolyte, allowing for the negative current seen. The Tafel slope for the cathode can be calculated using:

$$\text{Tafel Slope Cathode} = -\frac{2.303RT}{\alpha nF} \tag{3.1}$$

		j_0 (mA/cm^2)	α	Tafel slope (mV/decade)	R_{series} (Ω·cm^2)	u(j) mA/cm^2
Si/Pt	Anode	0.039	-	-	4.4	0.52
	Cathode			-		
Si/C	Anode	0.0019	0.69	86	7.6	0.75
	Cathode			-193		
Si/Ti	Anode	5.3e-8	0.37	162	4.06	0.93
	Cathode			-94		

Table 3.2: Fit results for the dark electrochemistry IV-curves for the different photo-electrodes, in which u(j) is the average error, defined as the absolute difference between the fitted and the experimental photocurrent at a certain voltage.

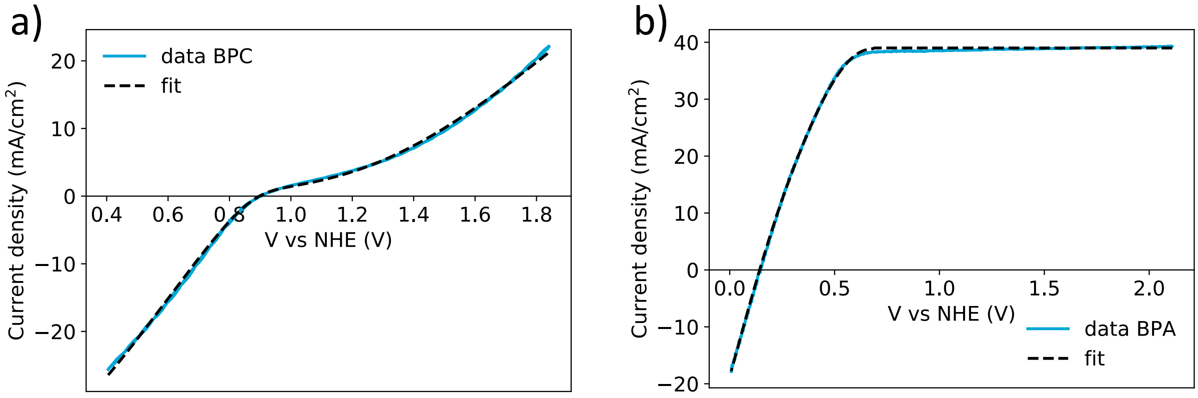

Figure 3.21: PEC fits of the experimental LSV curves obtained using the Back-side Photo Cathode (BPC) (a) and BPA (b). The BPC was immersed in a 0.2M [FeCN$_6$]$^{3-}$ + 0.2M [FeCN$_6$]$^{4-}$ (thus 50% SOC) solution, added to a 1M NH$_4$Cl supporting electrolyte. The BPA was immersed in a 0.4M [FeCN$_6$]$^{4-}$ (so close to 100% SOC) solution added to a 1M NH$_4$Cl supporting electrolyte.

which is derived from the butler-volmer equation for large voltages, where α is the symmetry parameter in the butler-volmer equation, and n is the number of electrons that partake in the reaction. Similarly, the Tafel slope for an anode is given by:

$$\text{Tafel Slope Anode} = \frac{2.303RT}{(1-\alpha)nF} \tag{3.2}$$

	j_0 (mA/cm^2)	α	Tafel slope (mV/decade)	R_{series} (Ω·cm^2)	u(j) mA/cm^2
BPA	0.0014	-	-	4.5	0.28
BPC	0.0010	0.13	69	12.1	0.27

Table 3.3: Fit results for the PEC IV-curves for the BPC and BPA, in which u(j) is the average error, defined as the absolute difference between the fitted and the experimental photocurrent at a certain voltage.

Due to the fast kinetics for the Pt electrode, changing the symmetry factor α (accounting for assymmetry in overpotential) does not influence the fit-error in any significant way. Therefore, the Tafel slopes in table 3.2 and 3.3 (as seen in equation 3.1 and 3.2) are uncertain as well.

3.3.2 Modeled versus Experimental charging efficiency

A selection of the STC% of the tested PEC flow batteries (as seen in figure 3.7) are compared to modeled curves in figure 3.22.

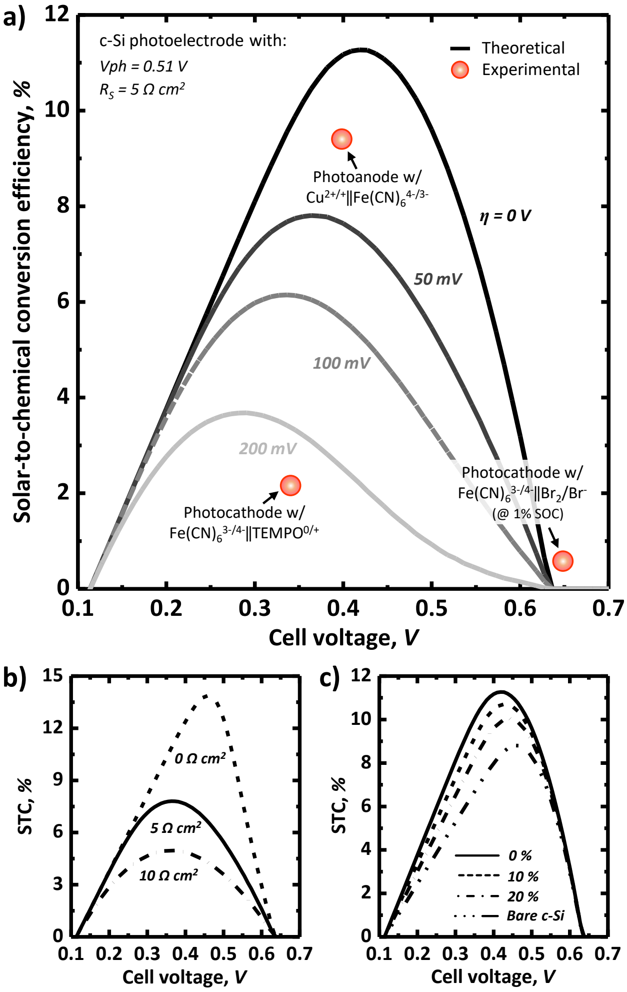

Figure 3.22: The photo-charging efficiency at 10% SOC is plotted as a function of the thermodynamic potential for different kinetic overpotentials (η_k = 0 V, 50mV, 100mV, 200mV at j = 10mA/cm^2). The system is modeled as a c-Si photoelectrode with a photovoltage (V_{ph}) of 0.51 V, a series resistance of 5 Ω·cm^2. The red circles indicate the experimentally measured value with various redox couples from the figure 3.6. (b) and (c) correspond to the model curves for different series/electrolyte resistance and reflection from the surface, respectively. The bare silicon reflection is implemented using the Fresnel coefficients (equation 2.20) and the bare-silicon complex indices of refraction. [59]

In figure 3.22, the solar conversion efficiencies at 10% SOC are shown to be 2.10% and 9.44% for the unbiased ferricynanide||TEMPO-sulfate and Cu-sulfate||ferrocyanide photo-charging cases, respectively. It is also worthwhile to note that the conversion efficiencies were calculated using a cell voltage at given SOC as shown in section 2.5.2.4. This photoelectrochemical charging efficiency for the Cu-sulfate||ferrocyanide cell is the highest among all the SRFBs with a single photon-device so far reported. Naturally, the ferricyanide||Br2/Br- combination case only showed 0.32% at 1% SOC (see figure 3.7) due to the gap between the photovoltage and cell voltage, necessary to drive the chemical reaction. Comparison of the experimentally measured results and theoretical estimation provided here in figure 3.22 reveals that the experimental results follow the predicted trend, and the overlap may serve as a guideline to further improvement. The discrepancy between the theoretical maximum at given cell potential and the experimental data indicates that there remains substantial room for improvement. Combining the LSV from the figure 3.6a (corresponding to the measured data point at 0.34V in the figure 3.22) and theoretical estimation with consideration of device configuration suggests that reducing the kinetic overpotential is the key for increasing the operating current density.

Chapter 4

Discussion

In this chapter, the results are reviewed in relation to the research question and device design principles. Moreover, recommendations for follow-up research are given.

4.1 Design Principles

Using the modeled and experimental results, several design principles are proposed for maximizing SRFB performance, which will be discussed in the following sections.

4.1.1 Front- versus backside illumination

In this work, both experimental results as well as modeled trends suggest backside-illuminated PEC redox flow batteries result in higher efficiencies and more stable performance. As seen in section 3.2, the parasitic light loss associated with electrolyte absorption in front-lit setups drastically decreases performance, especially in case of high electrolyte concentrations, which is the most important tool in acquiring the necessary high energy densities needed to compete with other electrical storage techniques. Even if there is little overlap between the spectra of electrolyte absorption and incoming solar radiation, the front-lit setup does not allow for effective conducting layer and anti-reflective optimization, as only a small set of materials, such as TiO_2, are suitable, i.e. transparent, anti-reflective as well as highly conductive. Since TiO_2 proved to induce poor device performance (see section 4.3), using back-lit configurations is highly recommended.

In some cases, electrolytes benefit from photon absorption, for example in the field of dye-sensitized solar cells, where photo-excitation of dye molecules on the photo-electrode aids the redox reaction for energy storage .[61, 62] In these cases the photo-activation, allows for better kinetics and more effective conversion. However, in general, photo-assisted side-reactions, like Prussian blue formation in ferri-/ferrocyanide electrolytes under illumination [63], decrease capacity and stability of the device.

4.1.2 Photo-absorber/redox-couple matching

As seen in section 3.2, the efficiency landscapes show optimal photo-absorber/redox-couple matching. Based on the loss mechanisms discussed, the optimal STC shifts around in the efficiency landscape. Since these losses are highly dependent on specific device parameters (for example the kinetic overpotentials depend strongly on redox-couples as well as the specific electrode/conducting layer used), the use of the modeled efficiency landscape is largely limited to establishing the general trends and dependencies. However, when specific parameters, such as the R_{series}, $j_{0,bv}$, α and V_{oc} are known (e.g. by using the fitting tool developed in this work), the efficiency landscape can be used to see where the optimum in the landscape resides and which losses, when reduced, have the biggest impact on the device performance. An example is shown in figure 4.1a, where the efficiency landscape is shown for the loss factors, derived from the BPC fit in section 3.3.1 (i.e. $j_{0,bv} = 0.001$ mA/cm^2, $\alpha = 0.13$ and $R_{series} = 12.1\Omega \cdot \text{cm}^2$)

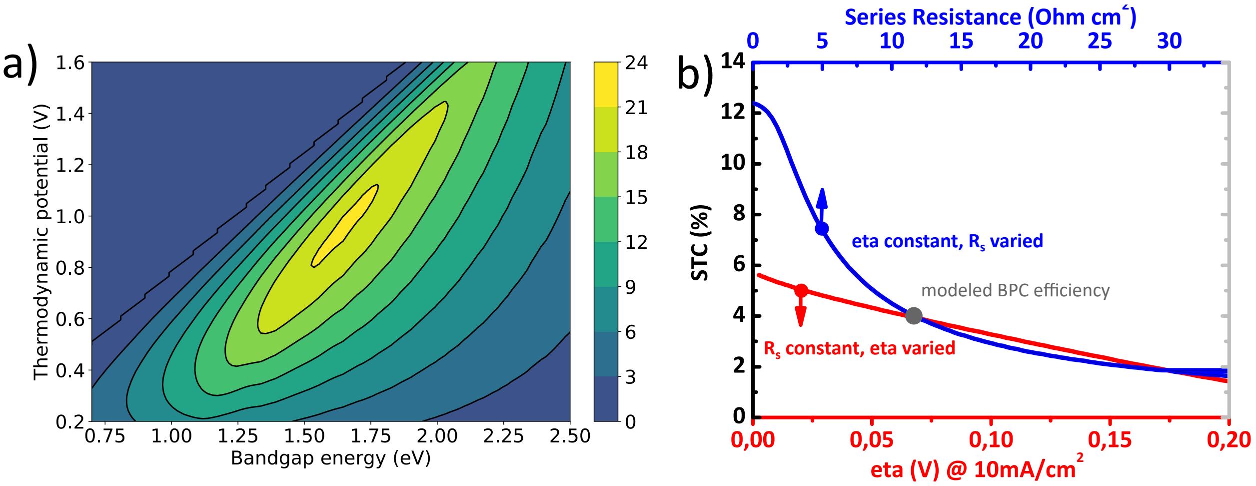

Figure 4.1: (a) shows the charging efficiency plotted for the loss parameters of the BPC-fit ($j_{0,bv} = 0.001$ mA/cm^2, $\alpha = 0.13$ and $R_{series} = 12.1\Omega \cdot cm^2$, see section 3.3.1). In (b), the sensitivities of the performance of a silicon-based SRFB on the same loss parameters are shown, by varying one of the two parameters and keeping the other constant. It is seen that reducing the series resistance results in performance enhancements to a larger extend than improving kinetics. Note that for clarity, the overpotential @ 10mA/cm^2 is plotted instead of the parameter $j_{0,bv}$.

As seen in figure 4.1b, the STC% has a strong dependency on series resistance, which could be exploited to improve device performance (e.g. by decreasing the charge carrier path length through the electrolyte), while improving kinetics (reducing the kinetic overpotential) has a relatively insignificant effect. Note that for clarity, the overpotential @ 10mA/cm^2 is plotted instead of the parameter $j_{0,bv}$. This example shows the utility of the sensitivity analysis in optimizing device design. Moreover, using figure 4.1a, it is seen that the optimum of the efficiency landscape is found at higher E_g and higher thermodynamic potentials (ΔE^0_{redox}).

4.1.3 SOC

To improve the STC%, averaged over the entire charging cycle, the SOC-dependent shift, as seen in figure 3.13 should be taken into account when choosing the optimal redox couples. Considering the fact that changing the redox couples during the operation is not realistic, these figures with SOC variance also imply that one should choose the photo-absorber material with a larger photovoltage than needed when just looking at a static SOC to allow operational flexibility. As discussed in a previous report, Wedege et al. demonstrated 95% SOC using a c-Si photocathode which exhibits a photovoltage exceeding the thermodynamic cell voltage by approximately 30%.[17]
This is illustrated clearly in figure 4.2, where the efficiency, averaged over a range between 1-99% SOC differs significantly from the case where only a static SOC of 50% is considered. When comparing figure 4.2a/b, it is seen that when considering the efficiency, averaged over an entire cycle, in general higher bandgap-energies and lower thermodynamic potentials are necessary, to keep high efficiencies.

The effect of a dynamic SOC, which changes during the course of a day (shown in figure 3.19) also influences the choice of suitable redox couples. Especially when considering the average charging speed is lower in winter than in the summer: for example, a battery which is charged up to 80% SOC in summer, only reaches ~ 40% in winter in the simulations of the present work. This phenomenon could diminish practical performance, especially since the optimum cell voltage in winter is expected to be higher (see figure 3.18), than in summer, but the average cell voltage in winter is lower (due to the lower SOC reached in winter).

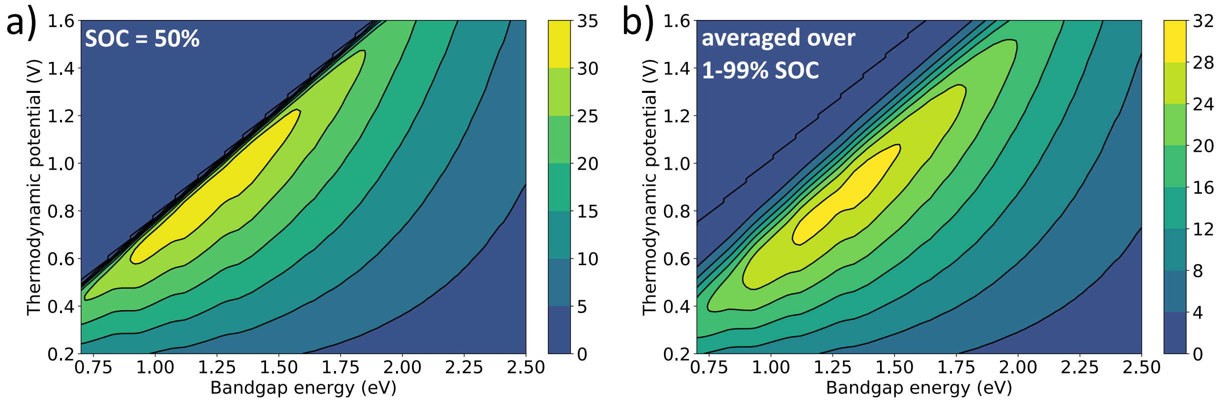

Figure 4.2: Efficiency landscape at 50% SOC (a) versus the efficiency landscape when averaged over 1-99% SOC to emphasize the difference in optimum photo-absorber/redox-couple matching.

4.1.4 Temperature regulation

As seen in section 3.2.2, the modeled STC efficiency depends strongly on the photo-absorber temperature. Depending on the type of redox species, the device performance either decreases or increases with temperature. This makes device temperature regulation a potentially promising technique for performance optimization. This is confirmed by the research of Zhang et al [64], where the peak power density of an all vanadium redox flow battery increased from 259.5mW/cm^2 to 349.8 mW/cm^2 when increasing temperature from 15 to 55 °C. However, higher cross-over effects, due to higher membrane permeability, result in capacity decay. Therefore, it is concluded that "thermal management of a real-world operating VRFB is essential in ensuring that the battery operates at the optimal thermal condition to achieve the most efficient and reliable operation." Adding the temperature dependence of the PV module when considering SRFBs only adds to this statement.

Since it is seen that the electrolyte functions as a natural coolant for the PV-module, there are two additional techniques of temperature regulation (apart from active regulation via external means):

- Flow speed control: Higher flow speeds yield higher forced convection, thus larger heat flows between the electrolyte and photo-absorber, resulting in more effective photo-absorber cooling and increasing the PV module performance. Lower flow speeds allow the electrolyte to heat up, during contact with the photo-absorber, which could improve kinetics and electrolyte conductivity. However, when adjusting flow-speeds, mass-transfer limits and the local SOC could change, which should also be taken into account. Insight in the extent of each of these trade-off effects could lead to improved performance via the simple method of flow speed control.
- Adjustment of photo-absorber area/total electrolyte volume ratio. A higher ratio would result in more electrolyte heating during a day of charging.

This work provides motivation for further research into temperature-controlled PEC redox flow batteries due to potentially significant performance improvement. However, experimental verification for the modeled trends is necessary to further research the significance of this topic and the feasibility of temperature regulation.

4.1.5 Accounting for seasonal/daily variance

As seen in section 3.2.3, the practical output power of a PEC device with realistic input and ambient temperatures, is significantly different from a device with the benchmark AM15 input. Using the model proposed

in this work and experimental results, such as IV-curves which can be used to fit the amplitude of the loss mechanisms, these 'lab-condition' efficiencies can be translated into practical output-power, which could be used in feasibility studies.
Moreover, the optimum cell voltage, as seen in figure 3.18, changes for different ambient conditions and solar inputs. Taking this into account could improve practical performance.

4.2 Model Accuracy

As seen in section 3.3.1, the modeled curves qualitatively describe the experimental IV-curves accurately. The fact that this is achieved only through variation of the model parameters (instead of e.g. fitting polynomials to mathematically describe the curves), shows that, although the analytical model is relatively simple, it is able to describe the processes inside a PEC device accurately.
This is reflected in the low average errors, as found in tables 3.2 and 3.3. The reason for the higher average errors in the case of the dark electrochemistry results is the higher amplitude of fluctuations in the mass-transfer limited regions (as seen in figure 3.20). Unfortunately, the average error u(j) in tables 3.2 and 3.3, is the sum of errors due to inaccuracies in the fit, as well as the quality of the data (e.g. a 'perfect' model curve, fitted through noisy data still yields an error). To accurately optimize and compare the accuracy of different fits, either high-quality data (such as seen in figure 3.21) or some method of compensating for the noise should be utilized.

Therefore the simplicity and accurate description of experimental data, strongly suggest the trends in the efficiency landscape in section 3.2.1, are accurate (under the assumption that the losses at the counter-electrode are negligible with respect to the losses at the photo-electrode, due to electrode optimization and large active areas with respect to the photo-electrode, as seen in section 2.4).

The temperature dependence of IV-curves and performance in the case of PEC-redox flow batteries have not been studied extensively. Because of this, the temperature dependence of several parameters (especially the temperature-enhanced kinetics and conductivity of the used electrolytes) is unknown for most reactions and setups. In this work, the well-documented reactions of oxygen an hydrogen evolution are used. Further experimental verification of the temperature dependence should be done to establish the shown trends with more certainty.

The application of the heat balance method, like the temperature dependence, is a work in progress. The values used for the convective heat transfer coefficients are reasonable but very general. For example, the convective heat transfer to air could be massively increased by considering finite wind speeds. However, the ambient temperature close to an extensive solar park is expected to be higher than its environment due to a large amount of solar-absorbing PEC flow batteries, having an opposite effect on the heat flux. Furthermore, flow-speeds inside the battery could influence heat flux flowing from the absorber to the electrolyte. These examples show a lot of possibilities for further research into enhanced PEC redox flow battery performance using temperature regulation.

4.3 Conducting layer performance

In this work, several conducting layers were tested for their catalytic performance and charge transfer. Figure 3.1 and 3.5, both suggest carbon and platinum conducting layers result in the highest kinetic performance. This is quantitatively verified when considering the fitted parameters for the dark-electrochemistry curves, where the exchange current density is orders of magnitudes higher for platinum and carbon when compared to titanium. The Mott-Schottky analysis support this trend, since it suggests a significant Schottky-barrier for the Ti layer (~ 0.4V)

Also this work shows that applying a TiO_2 layer has a significant negative impact on the onset potential (thus device performance), which can be attributed to a high Schottky-barrier at the TiO_2/electrolyte interface. Since TiO_2 is one of the few conducting layers with low impact on parasitic optical loss, a front-side illuminated device

Based on this, platinum and carbon are used as a thin conductive layer in the backside photo-anode and backside photo-cathode respectively. As seen in figure 3.6b, IV-curves for the Pt and C coated photo-cathodes are almost identical. Unfortunately, a C-coated photo-anode, similar to the Pt-coated photo-electrode is not fabricated in this work, due to time restrictions. However, the similar IV-curve for the photo-cathode, suggests a carbon photo-anode, fabricated in the same configuration as the high-performance, but highly expensive, Pt-coated photo-anode might be a feasible alternative. Moreover, using a carbon-coated photo-anode is expected to reduce mechanical damage to the system, since carbon has significantly lower selectivity towards hydrogen production (i.e. bubble formation) than platinum. [20]

4.4 SRFB performance

The backside photo-cathode and photo-anode both resulted in high solar to chemical efficiencies with respect to the field of single-junction SRFBs (as seen in figure 1.3). However, the BPA $Fe(CN)_6$/Cu battery proved superior to any of the BPC-batteries, with an STC efficiency of 9.4%, to our knowledge the best single-junction charging performance reported. This is attributed to the highly conducting platinum layer, precise band-alignment and careful redox couple selection (i.e. matching the cell voltage to the silicon band-gap). However, reversibility is a problem in this device, as copper-precipitation on the counter-electrode is seen when discharging the battery. This could be overcome using pH control, due to the pH-dependent stability of copper dissolution in ammonium chloride solution [65] or possibly be using an active copper electrode. [42]

Furthermore, it is seen that larger volume, results in higher photocurrent-densities, attributed to a lower electrolyte resistance, due to a larger number of charge-carrier-paths through the electrolyte.

Moreover, it is seen that the reported experimental values of the efficiencies resemble the modeled curves and follow the trends (see figure 3.22), verifying the performance estimation.

4.5 Recommendations

Due to the early stage of the SRFB-field, many aspects of the device have not been researched in detail. Therefore, several recommendations for further research follow from this research.

Due to the high solar-to-chemical efficiency of the silicon-based BPA $Fe(CN)_6$/Cu SRFB, further optimization of this device is recommended, to fabricate an SRFB with high round-trip efficiency and reversibility. Note that the RFB module (including the membrane, electrolyte concentration/conductivity, and flow-speed) of present work has not been optimized, meaning there is room for improvement, which is also reflected in figure 3.22, where optimum conditions could result in efficiencies exceeding these reported values.

Furthermore, the design principles discussed in the previous sections are expected to improve SRFB performance. Therefore, their application in the field is strongly suggested, to accomplish high efficiencies and ultimately economic feasibility of large-scale SRFB implementation.

To extend the performance estimation model and its use, the following ideas for further research are proposed. First of all, the microscopic chemical catalysis of the electrodes with various conducting layers (i.e. titanium, carbon, and platinum), resulting in the difference in kinetic performance is beyond the scope of this work. However, including numerical simulations of catalytic behavior could increase the value of this model, by predicting conducting layer performance. Following the same line of reasoning suggests the model would benefit from implementing a more realistic model for calculation of the solar absorber characteristics, using in-depth solid-state physics theory, like band-structure calculations.

Although the present work provides strong support for the validity of the modeled trends, more rigorous experimental research into these dependencies could be done. An example would be varying electrolyte concentration or the distance between electrodes and in turn varying electrolyte resistance to measure its impact on device performance experimentally.

As claimed before, the temperature dependence and impact of daily/seasonal variance, modeled in the present work is a work in progress. The following steps are suggested to improve the value of this model and to enhance SRFB performance by means of temperature regulation:

- Experimental validation of the modeled temperature dependence of IV-curves and performance (e.g. by varying electrolyte temperature using a hotplate)
- Experimental research regarding temperature regulation, using variable flow speeds and different area/volume ratios.
- Conduct a detailed experimental/theoretical analysis on temperature profiles and convective heat transfer in different environmental circumstances (e.g. varying illumination intensity), to increase the predictive value of the practical performance estimation.

Chapter 5

Conclusion

This work provides design principles for a PEC redox flow battery, to optimize the charging efficiency. Based on experiments and modeling the parasitic light losses, backside-illuminated devices are expected to outperform front-lit configurations. Moreover, a method for optimally matching the redox couples (i.e. the cell voltage) to the appropriate single-junction photo-absorber material (i.e. bandgap), is proposed based on device losses like series resistances, kinetic overpotential losses, and state-of-charge effects. This is done by modeling the solar-to-chemical efficiencies depending on the losses and cell voltage/bandgap matching and establishing general trends in the efficiency landscape (the efficiency as 2D-function of bandgap and cell voltage).
A tool is also developed to determine loss parameters in experimental setups, by fitting modeled IV-characteristics to experimental LSVs. Using the fitted loss parameters, the performance estimation can be used to find out which losses have the biggest impact when tackled.
Furthermore, the performance estimating model extends to include temperature dependence. In general, device performance decreases with increasing temperature. However, reaction kinetics and electrolyte conductivity improve with temperature, meaning in devices where these are the dominant limiting factors, overall device performance might improve with temperature. A heat balance method is employed to calculate photo-absorber temperature, based on real data for ambient temperature and incoming solar radiation and estimate practical performance PEC flow batteries. It showed that the cooling effect of the electrolyte has a large positive impact on device performance. Moreover, seasonal differences result in higher optimal cell-voltages during winter, with respect to summer, due to the temperature-induced photo-voltage increase.

Experimentally, it is found that a thin layer of carbon sputtered on the photo-absorber, results in high catalytic performance, close to a high-quality platinum catalyst, especially after optimizing deposition conditions (as seen in the thesis by Gerasimos Kanellos). Therefore, it could be a cheap and feasible alternative to expensive precious metals. Moreover, platinum is known to be a highly effective catalyst for hydrogen evolution, while carbon has poor HER-kinetics. Since hydrogen bubble formation is damaging to practical redox flow batteries, carbon conducting layers are favorable in this aspect.
Using a carbon-coated, silicon-based PEC flow battery with TEMPO-sulfate and ferricyanide as electrolytes, an STC efficiency of 2.1% was reached. Moreover, using a platinum-coated backside photo-anode, using $CuSO_4$ and ferricyanide as electrolytes, an STC of 9.4% was reached, the highest single-junction PEC flow battery charging efficiency reported until now, due to careful selection of the redox counter couple and a highly catalytic photo-anode. Although the battery faces issues with reversibility due to solid copper formation, this is a huge step forward. The 9.4% STC is close to the theoretical maximum, predicted by the realistically modeled curves, verifying the model experimentally.

Acknowledgements

From this place, I would like to thank a few people, without whom it would not have been possible to conduct this research and end up with the results reported in this work. First of all, my daily supervisor, dr. Dowon Bae, for the support, ideas, readiness to help, and the opportunities to publish original work in peer-reviewed journals. Also dr. Wilson Smith, for the enthusiasm and support during meetings. Furthermore, Gerasimos Kanellos, for showing a physicist the ropes of practical chemical research and for the various discussions on the many results and concepts involved in this work. I would also like to thank the assessment committee for taking time to process and discuss the results presented to you in this work. Lastly, the MECS group was very supportive, both in the positive atmosphere as well as the critical discussions during the various group meetings.

Bibliography

[1] European Commission. Roadmap 2050 - Imapct assessment and scenario analysis. pages 1–100, 2011.

[2] UNFCCC. Conference of the Parties (COP). ADOPTION OF THE PARIS AGREEMENT - Conference of the Parties COP 21. *Adoption of the Paris Agreement. Proposal by the President.*, 21932(December):32, 2015.

[3] John Paul Jones, G. K.Surya Prakash, and George A. Olah. Electrochemical CO 2 Reduction: Recent Advances and Current Trends. *Israel Journal of Chemistry*, 54(10):1451–1466, 2014.

[4] Key electricity trends 2017 based on monthly data. Technical report, 2018.

[5] Paul Denholm, Matthew O'Connell, Gregory Brinkman, and Jennie Jorgenson. Overgeneration from Solar Energy in California: A Field Guide to the Duck Chart. *Nrel*, (November):46, 2015.

[6] Perukrishnen Vytelingum, Sarvapali D. Ramchurn, Thomas D. Voice, Alex Rogers, and Nicholas R. Jennings. Trading agents for the smart electricity grid. *Proceedings of the International Joint Conference on Autonomous Agents and Multiagent Systems, AAMAS*, 2:897–904, 2010.

[7] Luis Oliveira, Maarten Messagie, Surendraprabu Rangaraju, Javier Sanfelix, Maria Hernandez Rivas, and Joeri Van Mierlo. Key issues of lithium-ion batteries - From resource depletion to environmental performance indicators. *Journal of Cleaner Production*, 108:354–362, 2015.

[8] Xiang Liu, Dongsheng Ren, Hungjen Hsu, Xuning Feng, Gui Liang Xu, Minghao Zhuang, Han Gao, Languang Lu, Xuebing Han, Zhengyu Chu, Jianqiu Li, Xiangming He, Khalil Amine, and Minggao Ouyang. Thermal Runaway of Lithium-Ion Batteries without Internal Short Circuit. *Joule*, 2(10):2047–2064, 2018.

[9] F. M. Mulder, B. M.H. Weninger, J. Middelkoop, F. G.B. Ooms, and H. Schreuders. Efficient electricity storage with a battolyser, an integrated Ni-Fe battery and electrolyser. *Energy and Environmental Science*, 10(3):756–764, 2017.

[10] Dowon Bae, Thomas Pedersen, Brian Seger, Mauro Malizia, Andrej Kuznetsov, Ole Hansen, Ib Chorkendorff, and Peter C. K. Vesborg. Back-illuminated Si photocathode: a combined experimental and theoretical study for photocatalytic hydrogen evolution. *Energy Environ. Sci.*, 8(2):650–660, 2015.

[11] Li Ji, Martin D. Mcdaniel, Shijun Wang, Agham B. Posadas, Xiaohan Li, Haiyu Huang, Jack C. Lee, Alexander A. Demkov, Allen J. Bard, John G. Ekerdt, and Edward T. Yu. A silicon-based photocathode for water reduction with an epitaxial SrTiO3 protection layer and a nanostructured catalyst. *Nature Nanotechnology*, 10(1):84–90, 2015.

[12] Jesse D. Benck, Linsey C. Seitz, Blaise A. Pinaud, Thomas F. Jaramillo, Arnold J. Forman, and Zhebo Chen. Modeling Practical Performance Limits of Photoelectrochemical Water Splitting Based on the Current State of Materials Research. *ChemSusChem*, 7(5):1372–1385, 2014.

[13] Dowon Bae, Brian Seger, Peter C.K. K Vesborg, Ole Hansen, and Ib Chorkendorff. Strategies for stable water splitting: Via protected photoelectrodes. *Chemical Society Reviews*, 46(7):1933–1954, 2017.

[14] Kristina Wedege, Dowon Bae, Wilson A. Smith, Adélio Mendes, and Anders Bentien. Solar Redox Flow Batteries with Organic Redox Couples in Aqueous Electrolytes: A Minireview. *Journal of Physical Chemistry C*, 122(45):25729–25740, 2018.

[15] Liyu Li, Xiaoliang Wei, Bin Li, Zhenguo Yang, Qingtao Luo, and Wei Wang. Recent Progress in Redox Flow Battery Research and Development. *Advanced Functional Materials*, 23(8):970–986, 2012.

[16] Kristina Wedege, João Azevedo, Amirreza Khataee, Anders Bentien, and Adélio Mendes. Direct Solar Charging of an Organic–Inorganic, Stable, and Aqueous Alkaline Redox Flow Battery with a Hematite Photoanode. *Angewandte Chemie - International Edition*, 55(25):7142–7147, 2016.

[17] Kristina Wedege, Dowon Bae, Emil Dražević, Adélio Mendes, Peter C.K. Vesborg, and Anders Bentien. Unbiased, complete solar charging of a neutral flow battery by a single Si photocathode. *RSC Advances*, 8(12):6331–6340, 2018.

[18] Gary Hodes, Joost Manassen, and David Cahen. Photoelectrochemical energy conversion and storage using polycrystalline chalcogenide electrodes. *Nature*, 261:403–404, 1976.

[19] Maheshwar Sharon, P. Veluchamy, C. Natarajan, and Dhananjay Kumar. Solar rechargeable battery-principle and materials. *Electrochimica Acta*, 36(7):1107–1126, 1991.

[20] Dowon Bae, Gerrit M. Faasse, Gerasimos Kanellos, and Wilson A. Smith. Unravelling the practical solar charging performance limits of redox flow battery based on the single photon device system. *Sustainable Energy & Fuels*, 3:2399–2408, 2019.

[21] Wenjie Li, Hui Chun Fu, Yuzhou Zhao, Jr Hau He, and Song Jin. 14.1% Efficient Monolithically Integrated Solar Flow Battery. *Chem*, 4(11):2644–2657, 2018.

[22] Félix Urbain, Sebastián Murcia-López, Nicole Nembhard, Javier Vázquez-Galván, Cristina Flox, Vladimir Smirnov, Katharina Welter, Teresa Andreu, Friedhelm Finger, and Joan Ramón Morante. Solar vanadium redox-flow battery powered by thin-film silicon photovoltaics for efficient photoelectrochemical energy storage. *Journal of Physics D: Applied Physics*, 52(4), 2019.

[23] Dowon Bae, Gerasimos Kanellos, Gerrit M. Faasse, Emil. Drazevic, Anirudh. Venugopal, and Wilson A. Smith. Design principles for efficient photoelectrodes in solar rechargeable redox flow battery applications. *Under submission.*

[24] Martin A Green. *Third Generation Photovoltaics - Advanced Solar Energy Conversion.* Springer, Heidelberg, 2008.

[25] Martin A Green and Low-injection Case. Limits on the Open-circuit Voltage and Efficiency. *IEEE Transactions on Electron Devices*, 31(5):671–678, 1984.

[26] Tom O M Tiedje, Eli L I Yablonovitch, George D. G.D. Cody, and Bonnie G. B.G. Bonnie G Brooks. Limiting Efficiency of Silicon. *IEEE transactions on electron devices*, 31(5):711–716, 1984.

[27] W Shockley and W T Read. Statistics of the Recombinations of Holes and Electrons. *Phys. Rev.*, 87(5):835–842, 9 1952.

[28] R N Hall. Electron-Hole Recombination in Germanium. *Phys. Rev.*, 87(2):387, 7 1952.

[29] A J Bard and L R Faulkner. *Electrochemical Methods: Fundamentals and Applications, 2nd Edition.* Wiley Textbooks, 2000.

[30] Yoshihiro Nakato, Keiichi Ueda, Hiroyuki Yano, and Hiroshi Tsubomura. Effect of microscopic discontinuity of metal overlayers on the photovoltages in metal-coated semiconductor-liquid junction photoelectrochemical cells for efficient solar energy conversion. *Journal of Physical Chemistry*, 92(8):2316–2324, 1988.

[31] Sophia Haussener, Shu Hu, Chengxiang Xiang, Adam Z. Weber, and Nathan S. Lewis. Simulations of the irradiation and temperature dependence of the efficiency of tandem photoelectrochemical water-splitting systems. *Energy and Environmental Science*, 6(12):3605–3618, 2013.

[32] Atousa Mehrani, Davoud Dorranian, and Elmira Solati. Properties of Au/ZnO Nanocomposite Prepared by Laser Irradiation of the Mixture of Individual Colloids. *Journal of Cluster Science*, 2015.

[33] Leikai Ma, Liang Xu, Kunpeng Zhang, Wei Wu, and Zhongquan Ma. The measurement of series and shunt resistances of the silicon solar cell based on LabVIEW. *2011 International Conference on Electrical and Control Engineering, ICECE 2011 - Proceedings*, pages 2711–2714, 2011.

[34] Romain Couderc, Mohamed Amara, and Mustapha Lemiti. In-Depth Analysis of Heat Generation in Silicon Solar Cells. *IEEE Journal of Photovoltaics*, 6(5):1123–1131, 2016.

[35] C J Glassbrenner and Glen A Slack. Thermal Conductivity of Silicon and Germanium from 3K to the Melting Point. *Phys. Rev.*, 134(4A):A1058–A1069, 1964.

[36] Frank Urban. The Influence of,Electrolytes,on,the,Specific,Heat,of,Water. *The Journal of Physical Chemistry*, 36(4):1108–1122, 2005.

[37] Afshin Andreas and Tom Stoffel. NREL Solar Radiation Research Laboratory (SRRL): Baseline Measurement System (BMS), 1981.

[38] Kristina Wedege, Dowon Bae, Wilson A Smith, Adélio Mendes, and Anders Bentien. Solar Redox Flow Batteries with Organic Redox Couples in Aqueous Electrolytes: A Minireview. *Journal of Physical Chemistry C*, 122:25729–25740, 2018.

[39] Dowon Bae, Brian Seger, Ole Hansen, Peter C.K. Vesborg, and Ib Chorkendorff. Durability Testing of Photoelectrochemical Hydrogen Production under Day/Night Light Cycled Conditions. *ChemElectroChem*, 6:106–109, 8 2019.

[40] Wenjie Li, Hui Chun Fu, Linsen Li, Miguel Cabán-Acevedo, Jr Hau He, and Song Jin. Integrated Photoelectrochemical Solar Energy Conversion and Organic Redox Flow Battery Devices. *Angewandte Chemie - International Edition*, 55(42):13104–13108, 2016.

[41] Cristina Flox, Sebastián Murcia-López, Nina M. Carretero, Carles Ros, Juan R. Morante, and Teresa Andreu. Role of Bismuth in the Electrokinetics of Silicon Photocathodes for Solar Rechargeable Vanadium Redox Flow Batteries. *ChemSusChem*, 11(1):125–129, 2018.

[42] Sergey S. Lemishko and Alexander S. Lemishko. Cu2+/Cu+ Redox Battery Utilizing Low-Potential External Heat for Recharge. *Journal of Physical Chemistry C*, 121(6):3234–3240, 2017.

[43] Amirreza Khataee, Kristina Wedege, Emil Dražević, and Anders Bentien. Differential pH as a method for increasing cell potential in organic aqueous flow batteries. *J. Mater. Chem. A*, 5(41):21875–21882, 2017.

[44] Farid A. Harraz, Junji Sasano, Tetsuo Sakka, and Yukio H. Ogata. Different Behavior in Immersion Plating of Nickel on Porous Silicon from Acidic and Alkaline Fluoride Media. *Journal of The Electrochemical Society*, 150(5):C277, 2003.

[45] Albert Polman, Mark Knight, Erik C. Garnett, Bruno Ehrler, and Wim C. Sinke. Photovoltaic materials: Present efficiencies and future challenges. *Science*, 352(6283), 2016.

[46] William Shockley and Hans J. Queisser. Detailed balance limit of efficiency of p-n junction solar cells. *Journal of Applied Physics*, 32(3):510–519, 1961.

[47] Nak Heon Choi, Soon-kwan Kwon, and Hansung Kim. Analysis of the Oxidation of the V(II) by Dissolved Oxygen Using UV-Visible Spectrophotometry in a Vanadium Redox Flow Battery. *Journal of The Electrochemical Society*, 160(6):A973–A979, 2013.

[48] X. T. Yang, X. S. Chai, Q. X. Hou, J. Y. Zhu, and L. G. Danielsson. Determination of anthraquinone-2-sulfonate in alkaline pulping liquor by spectrophotometry using a Nafion membrane interface. *Analytica Chimica Acta*, 474(1-2):69–76, 2002.

[49] James M. Gardner, Maria Abrahamsson, Byron H. Farnum, and Gerald J. Meyer. Visible light generation of iodine atoms and I-I bonds: Sensitized I - oxidation and I3- photodissociation. *Journal of the American Chemical Society*, 131(44):16206–16214, 2009.

[50] Henning Döscher, John F. Geisz, Todd G. Deutsch, and John a. Turner. Sunlight absorption in water – efficiency and design implications for photoelectrochemical devices. *Energy Environ. Sci.*, 7(9):2951–2956, 2014.

[51] M. F. Stuckings and A. W. Blakers. A study of shading and resistive loss from the fingers of encapsulated solar cells. *Solar Energy Materials and Solar Cells*, 59(3):233–242, 1999.

[52] Percival A. Lasselle and John G. Aston. The Conductivity of Sodium Iodide Solutions at 25° and the Limiting Conductance of the Iodide Ion. *Journal of the American Chemical Society*, 55(8):3067–3071, 1933.

[53] Grinnell Jones and Frederic C. Jelen. The Conductance of Aqueous Solutions as a Function of the Concentration. II. Potassium Ferrocyanide. *Journal of the American Chemical Society*, 58(12):2561–2565, 1936.

[54] William M. Haynes. *CRC Handbook of Chemistry and Physics, 95th Edition, 2014-2015*. CRC Press, 95th edition, 2014.

[55] C R C Handbook, C R C Press, Boca Raton, Aqueous Solutions, Body Fluids, and CRC Press. Electrical Conductivity of Aqueous Solutions. *Handbook of Chemistry and Physics, 95th Edition*, page 178, 1989.

[56] Artjom Maljusch, Félix Urbain, Wolfram Jaegermann, Friedhelm Finger, Uwe Rau, Bernhard Kaiser, Sascha Hoch, Vladimir Smirnov, Florent Yang, Jürgen Ziegler, and Jan-Philipp Becker. Influence of the operating temperature on the performance of silicon based photoelectrochemical devices for water splitting. *Materials Science in Semiconductor Processing*, 42:142–146, 2015.

[57] Priyanka Singh and N. M. Ravindra. Temperature dependence of solar cell performance - An analysis. *Solar Energy Materials and Solar Cells*, 101:36–45, 2012.

[58] Keerthi K Nair, Jitty Jose, and Ajith Ravindran. Analysis of temperature dependent parameters on solar cell efficiency using MATLAB. *2016 Ijedr |*, 4(3):536–541, 2016.

[59] Martin A. Green. Intrinsic concentration, effective densities of states, and effective mass in silicon. *Journal of Applied Physics*, 67(6):2944–2954, 1990.

[60] University of Maine Climate Change Institute. Climate reanalyzer. `https://ClimateReanalyzer.org`. Accessed: 13-09-2019.

[61] Ping Liu, Yu Liang Cao, Guo Ran Li, Xue Ping Gao, Xin Ping Ai, and Han Xi Yang. A solar rechargeable flow battery based on photoregeneration of two soluble redox couples. *ChemSusChem*, 6(5):802–806, 2013.

[62] Mingzhe Yu, William D. McCulloch, Damian R. Beauchamp, Zhongjie Huang, Xiaodi Ren, and Yiying Wu. Aqueous Lithium-Iodine Solar Flow Battery for the Simultaneous Conversion and Storage of Solar Energy. *Journal of the American Chemical Society*, 137(26):8332–8335, 2015.

[63] Torn Ozeki, Koichi Matsumoto, and Seiichiro Hikime. Photoacoustic Spectra of Prussian Blue and Photochemical Reaction of Ferric Ferricyanide. *Analytical Chemistry*, 56(14):2819–2822, 1984.

[64] C. Zhang, T. S. Zhao, Q. Xu, L. An, and G. Zhao. Effects of operating temperature on the performance of vanadium redox flow batteries. *Applied Energy*, 155:349–353, 2015.

[65] Hirokazu KONISHI, Takashi BITOH, Hideki ONO, Tetsuo OISHI, Kazuya KOYAMA, and Mikiya TANAKA. Behavior of Copper Dissolution in an Ammonia Solution Containing Ammonium Chloride or Sulfate. *Journal of the Japanese Society for Experimental Mechanics*, 14(Special_Issue):s205–s209, 2014.

Appendix A

Supporting modeling information

A.1 Parasitic absorption by various electrolytes

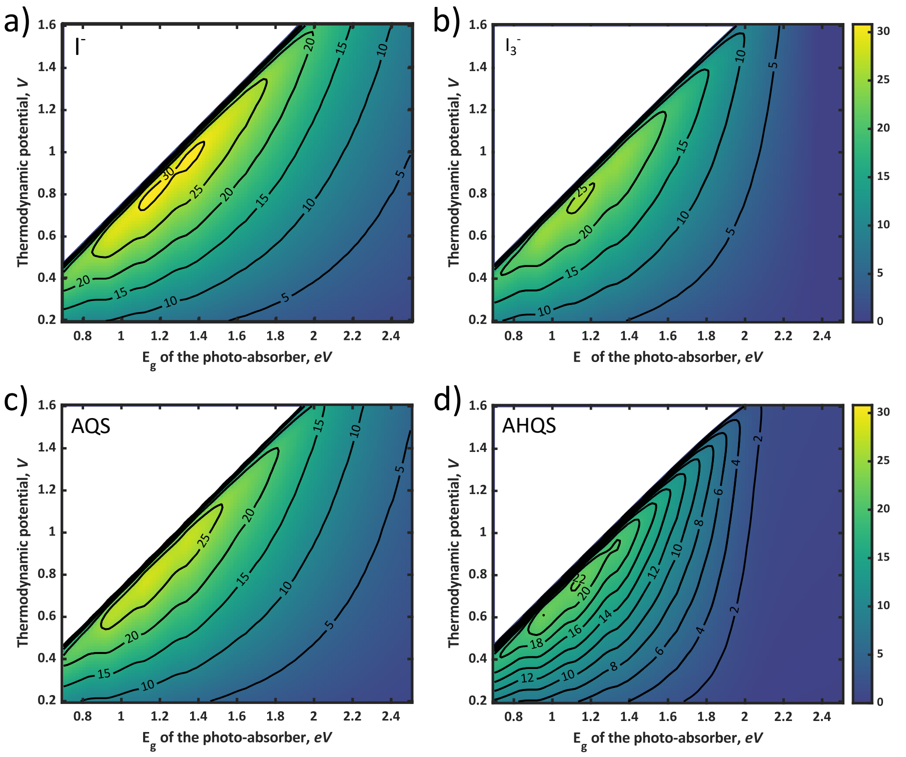

Figure A.1: Contour-plots for I^- (a), I^{3-} (b), AQS (c) and AHQS (d) in front lit configuration, showing the sensitivity of the STC for the electrolyte absorption. Note that in general the absorption spectrum of the redox species in the couples (e.g., I^-/I^{3-}) are different, meaning that the parasitic electrolyte absorption (and thus the STC) depends on the SOC of the battery.

A.2 Reflection spectra for silicon photo absorber in different cases

In figure A.2a and b, the schematic depictions of the front- and backlit setups and the reflection spectra of silicon in different cases, show an explanation as to why there are situations in which front-side illumination outperforms back-side illumination, as seen in Figure 3e of the main paper (which is counter-intuitive at first glance). It is seen that the reflection of the silicon is higher when the light is coming from the air, as opposed to when it is coming from an electrolyte. In this way, the electrolyte acts as an antireflective layer, as seen in Figure S2c), and this effect could outweigh the electrolyte absorption. This results in some front-lit configurations outperforming back-side illumination.

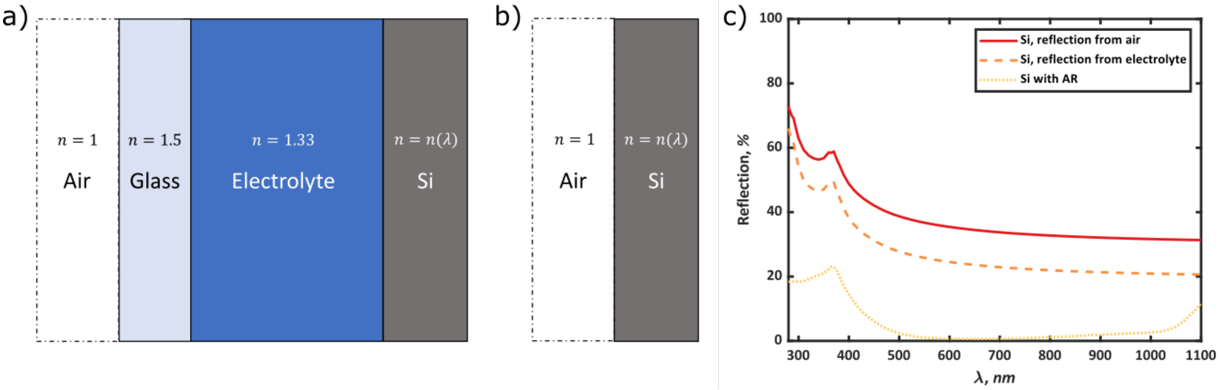

Figure A.2: In a and b, schematic representations of the reflection interfaces are shown in case of front-lit (a) and back-lit (b) configurations. In c, three reflection spectra of silicon are shown: reflection of bare silicon when lighting from air, reflection of bare silicon when lighting from an electrolyte and the reflection of AR-treated silicon. Since the refractive index of the electrolyte is closer to that of the silicon than the refractive index of air, the reflection is reduced for light coming through the electrolyte

A.3 Electrolyte resistance example calculation

To calculate the total resistance of an electrolyte, consisting of a 1M NH4Cl supporting electrolyte and an active redox electrolyte with an estimated specific conductivity of 75 mS/cm, the NH4Cl curve in Figure 5c) of the original paper is linearly interpolated to find a specific conductivity of 101.2 mS/cm. Using the specific conductivity of 75mS/cm for the active electrolyte, the total conductivity is approximated by $75+101.2 = 176.2$ mS/cm (Kohlrausch's law of independent ionic migration). In this work, interionic interactions are not considered. The resistance can be calculated using:

$$R \cdot A = \frac{l}{\kappa} = \frac{2}{0.1762} \approx 11.35\ \Omega \cdot cm^2 \tag{A.1}$$

with l the path-length, A the area and κ the conductivity. The other resistances are calculated in the same manner.

A.4 Collection probability & Surface recombination

In figure A.3, the collection probability $C_p(z)$ is plotted for varying surface recombination velocity, S. The equation for the collection probability is given in equation A.2, based on the paper by Bae et al [10]:

$$C_p(z) = \left(\cosh \frac{L-z}{L_e} + \sinh \frac{L-z}{L_e} \cdot \frac{\sinh \frac{z}{L_e} + SL_e \cosh \frac{z}{L_e}}{\cosh \frac{z}{L_e} + SL_e \sinh \frac{z}{L_e}} \right)^{-1} \tag{A.2}$$

in which L is the photo-absorber layer thickness, z is the spatial coordinate along the depth axis, L_e is the minority carrier diffusion length and S is the surface recombination velocity, normalized by the diffusivity ($S = v_s/D$, where v_s is the surface recombination velocity and D is the diffusivity). With this equation, only the first half of figure A.3 and figure 2.7 (from 0 to 100μm) is described, whereas the latter halve (100-350μm) is found by mirroring equation A.2

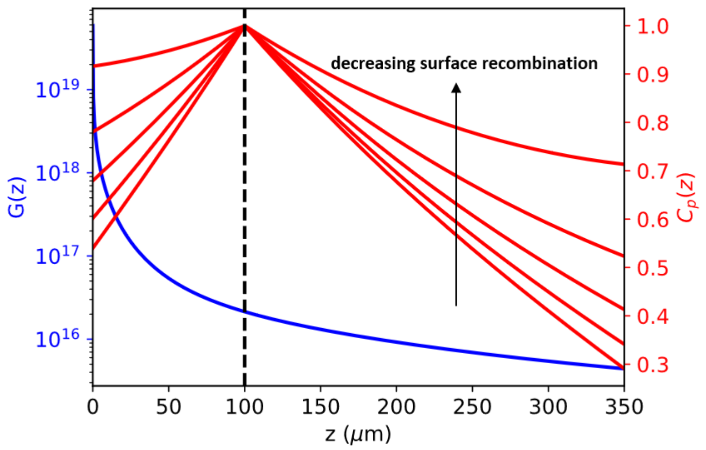

Figure A.3: Charge generation and collection probability, plotted as function of the spatial coordinate (z) perpendicular to the plane of the absorber (along the depth-axis), for varying surface velocities S

A.5 Performance model detailed derivation

When solving equation 2.2 for V_D, one obtains:

$$V_D = \frac{k_b T}{e} \ln \frac{j_D + j_0}{j_0} = V_{oc} + \frac{k_b T}{e} \ln \frac{j_D + j_0}{j_{max,photo} + j_0} \approx V_{oc} + \frac{k_b T}{e} \ln \frac{j_D}{j_{max,photo}} \tag{A.3}$$

since $j_0 \ll j_{max,photo}$ and $j_0 \ll j_D$. Then V_{oc} is given by:

$$V_{oc} = \frac{k_b T}{e} \ln \frac{j_{max,photo} + j_0}{j_0} \approx \frac{k_b T}{e} \ln \frac{j_{max,photo}}{j_0} \tag{A.4}$$

since again $j_0 \ll j_{max,photo}$

Appendix B

Supporting experimental information

B.1 Counter-electrode overpotential

Experimental linear sweep voltammograms (LSVs) of n-type Si electrodes under dark conditions for the cathodic charging of $Fe(CN)_6^{3-}$ in figure B.1, shows how the overpotential varies with the type of conducting layer. The inset shows LSV's for a carbon felt electrode submerged in an anolyte (NaI and TEMPO-sulfate in this case) that exhibits a negligible overpotential owing to sufficient active area of the carbon felt.

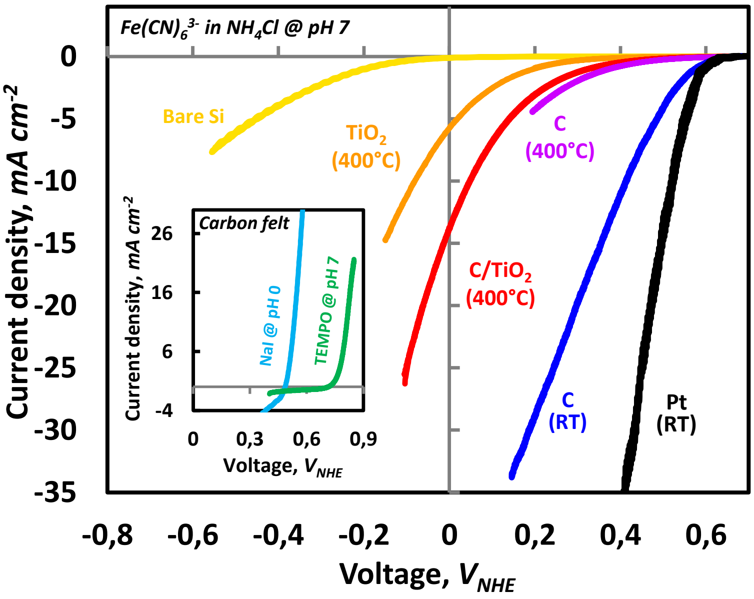

Figure B.1: Experimental LSV data is plotted for a single silicon photo absorber with various conducting layers, submerged in a $[Fe(CN)_6]^{3-}$ electrolyte (in NH_4Cl at pH7), showing overpotential is strongly dependent on the type of conducting material. The inset depicts LSV data for a carbon felt electrode, immerged in anolytes (NaI and TEMPO-sulfate at pH 0 and 7, respectively).

B.2 Detailed photo-charging data

	V_{cell} **@50 SOC (V)**	**STC% @ SOC%**	**Cell volume (mL)**	**Accumulated Charge (C)**	**Charge Capacity (C)**
BPC					
$Fe(CN)_6^{3-}$/Br-	0.65	0.32 @ ∼1	25	20	965
$Fe(CN)_6^{3-}$/TEMPO	0.34	1.4 @ 20	10	88	385
$Fe(CN)_6^{3-}$/TEMPO	0.34	2.1 @ 15	25	155	965
BPA					
$Fe(CN)_6^{3-}$/Cu^{2+} - short-term	0.4	9.44 @ 10	25	93	965
$Fe(CN)_6^{3-}$/Cu^{2+} - long-term	0.4	7.7 @ 50	15	398	578

B.3 Electrolyte reactions

The electrolytes, their reactions and redox potentials vs NHE are found in this section. **Back-side photo-anode:**

$$[\mathrm{Fe(CN)_6}]^{4-} \xrightleftharpoons[\text{discharging}]{\text{charging}} [\mathrm{Fe(CN)_6}]^{3-} + \mathrm{e}^- \qquad 0.48\text{V vs NHE} \tag{B.1}$$

$$\mathrm{Cu}^{2+} + \mathrm{e}^- \xrightleftharpoons[\text{discharging}]{\text{charging}} \mathrm{Cu}^+ \qquad 0.08\text{V vs NHE} \tag{B.2}$$

Back-side photo-cathode:

$$[\mathrm{Fe(CN)_6}]^{3-} + \mathrm{e}^- \xrightleftharpoons[\text{discharging}]{\text{charging}} [\mathrm{Fe(CN)_6}]^{4-} \qquad 0.48\text{V vs NHE} \tag{B.3}$$

$$\text{TEMPO}-\text{sulfate}^0 \xrightleftharpoons[\text{discharging}]{\text{charging}} \text{TEMPO}-\text{sulfate}^+ + \mathrm{e}^- \qquad 0.82\text{V vs NHE} \tag{B.4}$$

$$2\,\mathrm{Br}^- \xrightleftharpoons[\text{discharging}]{\text{charging}} \mathrm{Br_2(aq)} + 2\,\mathrm{e}^- \qquad 1.1\text{V vs NHE} \tag{B.5}$$

Appendix C

Python Code

In the next sections, the python code, used in this work to model the SRFB performance is shown. The first three files consist of the input parameters for the model, such that several dependencies, loss effects etc can be switched on and off conveniently. The next files are the actual simulation and fit tool, followed by a file with functions used in the simulation and fit tool. Lastly, a file for general data-processing is added, to conveniently visualize/animate the results obtained by the simulation file.

C.1 Input parameters

The input parameters are divided into three python files. The first is model_settings.py, the second losses.py and the third physical constants.py.

C.1.1 Model settings

```
# -*- coding: utf-8 -*-
"""
Created on Mon Aug 26 14:44:43 2019

@author: Richard
"""

# ==============================================================================
# Define the settings
# ==============================================================================
REAL_SOLAR_DATA = False           # True if you want real NREL data, in that
                                  # case fill in a date in simulation.py, False
                                  # if you want the AM15 spectrum

REAL_ABSORBER_DATA = False        # Choose if you want to use the real silicon
                                  # Absorption spectra, or just absorption cal-
                                  # culated using the band-gap

DYNAMIC_SOC = False               # Choose if you want an SOC that changes du-
                                  # ring the day

TEMP_DEPENDENT_J0 = False         # If you want a temperature dependent J0,
                                  # check whether the J0_BV_ref and E_a are
                                  # well defined

AUGER_RECOMBINATION = False       # Using Auger recombination is only accurate
                                  # if REAL_ABSORBER_DATA = True

save_fit_progression = False      # Choose True if you want to save the para-
```

```
                                  # meters the fit-tool varies throughout the
                                  # fitting process

charge_collection_method = False  # Choose True if you want to use the charge
                                  # collection method, False if you don't


# ============================================================================
# Define the resolutions of the model inputs
# ============================================================================
NUM_IV_POINTS = 1000              # Number of datapoints used for the iv-curve

NUM_E_G = 100                     # Number of band-gap energies (will be
                                  # changed to 1 if REAL_ABSORBER_DATA = True)

NUM_E_THERM = 100                 # Number of thermodynamic potentials, set
                                  # the range in simulation.py

NUM_TIME_STEPS = 1                # Set number of time-steps in case of para-
                                  # meter dependent simulation
```

C.1.2 Definition of the losses

```
# -*- coding: utf-8 -*-
"""
Created on Mon Aug 26 14:56:47 2019

@author: Richard
"""


# ============================================================================
# Define the losses
# ============================================================================

R_SERIES = 5            # Includes both PV resistance as well as     [Ohm*cm2]
                         # electrolyte/membrane resistance

JLIM_ANODE = 0.05       # Mass transfer limited anodic current       [mA/cm2]
JLIM_CATHODE = -0.05    # Mass transfer limited cathodic current     [mA/cm2]

J0_BV = 0.001            # Exchange current density (bv equation)     [mA/cm2]

J0_BV_ref = 6420         # Reference exchange current density for temperature
                         # dependence                                  [mA/cm2]
E_A = 48000
ALPHA = 0.5              # Symmetry factor bv equation                [-]
```

C.1.3 Definition of the physical constants

```
# -*- coding: utf-8 -*-
"""
Created on Mon May 13 15:43:31 2019

@author: Richard Faasse
"""
Q = 1.602E-19                   # Elementary charge :           [C/electron]
N_A = 6.022E23                  # Avogadro's number             [-/mol]
F = Q*N_A                       # Faraday constant:             [C/mol]
R = 8.314                       # Gas constant:                 [J/mol/K]
H = 6.626E-34                   # Plancks constant:             [m2 kg/s]
K_B = 1.38E-23                  # Boltzmann constant:           [m2 kg/s2/K]
C = 3E8                         # Speed of light:               [m/s]
SIGMA = 5.67E-8                 # Stefan Boltzmann constant:    [J/s/m2/K4]
```

C.2 simulation

```
# -*- coding: utf-8 -*-
"""
Created on Mon May  6 13:44:07 2019

@author: Richard Faasse
"""

import sys
import time
import numpy as np
import numpy.matlib
from physical_constants import Q, F, R, H, K_B, C
from device_parameters import VOLUME, CAPACITY, SOC, RHO, C_ELECTROLYTE, A, \
THICKNESS, AREA_ABSORBER
from model_settings import REAL_ABSORBER_DATA, REAL_SOLAR_DATA, \
TEMP_DEPENDENT_J0,  NUM_E_G, NUM_IV_POINTS, NUM_E_THERM, DYNAMIC_SOC, \
NUM_TIME_STEPS, charge_collection_method

from losses import J0_BV, J0_BV_ref, R_SERIES, E_A, ALPHA


from functions import calculate_flux_balance, calculate_iv_curve, IV_with_Auger
import datetime as dt
sys.path.insert(0,’..\input_data’)
input_data_path = ’..\input_data\\’
#import 20180731.csv


# ==============================================================================
# Define the device parameters
# ==============================================================================
if REAL_ABSORBER_DATA:
    NUM_E_G = 1
    E_G = np.array([1.12])*Q
else:
    # Choose number of bandgap energies and the range or specific bandgap
    # energy
    if NUM_E_G > 1:
        E_G = np.linspace(0.7, 2.5, NUM_E_G)*Q
    elif NUM_E_G == 1:
        E_G = np.array([1.12])*Q

# Choose the number of thermodynamic potentials and the range or specific
# thermodynamic potential
if NUM_E_THERM > 1:
    E_THERM = np.linspace(1.6, 0.2, NUM_E_THERM)
elif NUM_E_THERM == 1:
    E_THERM = np.array([0.4])


SOC = SOC*np.ones((NUM_E_G, NUM_E_THERM))




# ==============================================================================
# Load the spectrum and temperature
# ==============================================================================
if not isinstance(REAL_SOLAR_DATA, bool):
    sys.exit("Choose␣boolean␣value␣for␣REAL_SOLAR_DATA␣")
elif REAL_SOLAR_DATA:
    DATE = ’20180731’
```

```
    # Load real time solar spectra
    SPECTRAL_DATA = np.genfromtxt(input_data_path + DATE
                                  + '.csv', delimiter=',')
    LABDA_SPECTRUM = np.arange(SPECTRAL_DATA[0, 4],
                               SPECTRAL_DATA[0, 5] + 1, SPECTRAL_DATA[0, 6])
    POWER_SPECTRUM = SPECTRAL_DATA[:, 7:len(LABDA_SPECTRUM)+7]


    DAYTIME = np.floor(SPECTRAL_DATA[:, 3]/100) \
              + np.remainder(SPECTRAL_DATA[:, 3], 100)/60
    DT = DAYTIME[1]-DAYTIME[0]

    #Load temperature data
    OPEN_DATA = open(input_data_path + 'temperature_data_'
                     + DATE + '.txt', 'r')
    COUNT = 0
    day_in_the_year = np.zeros((45000*12,))
    T_AIR = np.zeros((45000*12, 2))

    keep_temperature = np.ones((45000*12,), dtype=bool)

    LINE = 0
    for LINE in OPEN_DATA:
        # Extract temperature data
        stripped = LINE.strip()
        columns = stripped.split(',')
        T_AIR[COUNT, :] = columns[1:3]

        # Match temperature data with spectral data, by matching both date as
        # well as time
        date_string = columns[0]
        date_list = (date_string.split('/'))
        month = int(date_list[0])
        day = int(date_list[1])
        year = int(date_list[2])
        day_in_the_year[COUNT] = (dt.date(year, month, day)
                                  - dt.date(year, 1, 1)).days + 1
        times_in_day_spectral_data = SPECTRAL_DATA[SPECTRAL_DATA[:,2] ==
                                                   day_in_the_year[COUNT],3]
        keep_temperature[COUNT] = np.any(np.round(times_in_day_spectral_data)
                                         == (np.round(T_AIR[COUNT, 0]*100)))

        COUNT = COUNT + 1

    T_AIR = T_AIR[keep_temperature,:]
    day_in_the_year = day_in_the_year[keep_temperature]
    day_in_the_year[-2:-1] = day_in_the_year[np.sum(day_in_the_year>0)-1]

    #delete empties
    day_in_the_year = day_in_the_year[day_in_the_year>0]
    T_AIR = T_AIR[(T_AIR[:, 0] > 0)]
    T_AIR[:, 0] = np.round(T_AIR[:, 0]*100)
    T_AIR[:, 1] = T_AIR[:, 1]+273.15
    NUM_TIME_STEPS = np.size(POWER_SPECTRUM, 0)

    del COUNT, columns, stripped, OPEN_DATA, LINE
elif not REAL_SOLAR_DATA:
    # Load AM15 spectrum

    SOLAR_SPECTRUM = np.transpose(np.load(input_data_path
                                          + 'solar_spectrum.npy'))
    POWER_SPECTRUM = np.zeros(np.shape(
            SOLAR_SPECTRUM[:, SOLAR_SPECTRUM[0, :] >= 290]))
    POWER_SPECTRUM[0, :] = SOLAR_SPECTRUM[1, SOLAR_SPECTRUM[0, :] >= 290]
    LABDA_SPECTRUM = SOLAR_SPECTRUM[0, SOLAR_SPECTRUM[0, :] >= 290]
```

```
    T_AIR = 300*np.ones((NUM_TIME_STEPS, 2))
    DT = 1

# =============================================================================
# Load absorbance data
# =============================================================================
if REAL_ABSORBER_DATA:
    SI_DATA = np.load(input_data_path + ’SI_DATA.npy’)
    B = SI_DATA[:, 5] * 1E-4 * 300
    ALPHA_SI = SI_DATA[:, 1]
    ALPHA_SI = np.interp(LABDA_SPECTRUM, SI_DATA[:, 0], ALPHA_SI)
    ABSORBANCE = 1 - np.exp(-ALPHA_SI*THICKNESS)



T_ELECTROLYTE = T_AIR[0, 1]
# =============================================================================
# Initialize arrays
# =============================================================================
input_power = np.zeros((NUM_TIME_STEPS, ))
soc_correction = np.zeros((NUM_E_G, NUM_E_THERM))
current_limit = np.zeros(NUM_E_G)
iv_curve = np.zeros((2, NUM_E_G, NUM_IV_POINTS, NUM_TIME_STEPS))
sufficient_photovoltage = np.zeros((NUM_E_G, NUM_IV_POINTS, NUM_E_THERM))
operating_current = np.zeros((NUM_E_G, NUM_E_THERM))
efficiency = np.zeros((NUM_E_G, NUM_E_THERM, NUM_TIME_STEPS))
output_power = np.zeros((NUM_E_G, NUM_E_THERM, NUM_TIME_STEPS))
output_temperature = np.zeros((NUM_TIME_STEPS,))
output_temperature_electrolyte = np.zeros((NUM_TIME_STEPS,))
tmp = np.zeros((NUM_TIME_STEPS,))
current_plot = np.zeros((NUM_TIME_STEPS,))
ETA = np.linspace(0, 0.6, NUM_TIME_STEPS)
jlim_array = -np.linspace(0.1,0.01,NUM_TIME_STEPS)

START_TIME = time.time()
#%%
# =============================================================================
# Use one of the following parameter arrays if you want to vary them, make
# sure NUM_TIME_STEPS > 1
# =============================================================================

R_series_array = np.linspace(0,34.3,NUM_TIME_STEPS)
#SOC_array = np.l1inspace(0.01,0.99, NUM_TIME_STEPS)
T_ARRAY = np.linspace(273.15, 373.15, NUM_TIME_STEPS)
j0_bv_array = np.logspace(-1,-5, NUM_TIME_STEPS)
alpha_array = np.linspace(0.25,0.75, NUM_TIME_STEPS)
#j0_bv_array = np.array((1000000000000, 4.45E-3, 1.46E-3, 2.1E-4 ))
#j0_bv_array[0] = 100000
REFL_ARRAY = np.array((0, 0.05, 0.1, 0.2))

# =============================================================================



for kk in range(NUM_TIME_STEPS):

    # If you want a varying parameter, and uncommented one of the lines above,
    # uncomment the adequate line below:

#    SOC = SOC_array[kk]*np.ones((NUM_E_G, NUM_E_THERM))
    J0_BV = j0_bv_array[kk]
    R_SERIES = R_series_array[kk]
#    ALPHA = alpha_array[kk]

    if REAL_SOLAR_DATA:
        INCOMING_SPECTRUM = np.array((LABDA_SPECTRUM, POWER_SPECTRUM[kk, :]))
```

```
    else:
        INCOMING_SPECTRUM = np.array((LABDA_SPECTRUM, POWER_SPECTRUM[0, :]))

    INCOMING_SPECTRUM = np.transpose(INCOMING_SPECTRUM)
    for ii in range(NUM_E_G):
        if REAL_ABSORBER_DATA:
            current_limit[ii], temp_absorber, input_power[kk], q_in = \
            calculate_flux_balance(INCOMING_SPECTRUM, E_G[ii], T_AIR[kk, 1],
                                   ABSORBANCE, T_ELECTROLYTE, 0.6)
#            temp_absorber = T_ARRAY[kk]

            ALPHA_SI = SI_DATA[:, 1] * (temp_absorber/300)**B
            ALPHA_SI = np.interp(LABDA_SPECTRUM, SI_DATA[:, 0], ALPHA_SI)
            N = np.interp(LABDA_SPECTRUM, SI_DATA[:, 0], SI_DATA[:, 2])
            K = np.interp(LABDA_SPECTRUM, SI_DATA[:, 0], SI_DATA[:, 3])
#           REFL = ((N-1) + K)**2/((N+1) + K)**2
            REFL = 0
            ABSORBANCE = (1 - np.exp(-ALPHA_SI*THICKNESS)) * (1-REFL)
            ABSORBANCE[LABDA_SPECTRUM>1440] = 0

            E_photon = H*C/(LABDA_SPECTRUM*1E-9)

            dE = np.zeros(np.shape(E_photon))
            dE[0:-1] = np.abs(E_photon[0:-1] - E_photon[1:])
            dE[-1] = dE[-2]
            J_photon = POWER_SPECTRUM[0, :]/E_photon*(1-REFL)
            dlabda = np.zeros((len(LABDA_SPECTRUM),))
            dlabda[0:-1] = np.abs(LABDA_SPECTRUM[0:-1]
                             - LABDA_SPECTRUM[1:])
            dlabda[-1] = dlabda[-2]

            v_oc = 0.7   #Initialize v_oc, to converge to it later

            # Iterate the temperature/v_oc calculations a few times, to
            # obtain convergence
            for i in range(3):
                current_limit[ii], temp_absorber, input_power[kk], q_in = \
                calculate_flux_balance(INCOMING_SPECTRUM, E_G[ii],
                                       T_AIR[kk, 1], ABSORBANCE, T_ELECTROLYTE,
                                       v_oc)

                b1 = (2/H**3*1**2/C**2*E_photon**2
                      *np.exp(-E_photon/K_B/temp_absorber))
                integral = np.sum(b1*ABSORBANCE*dE)
                dark_saturation_current = Q*np.pi*integral/10**4

                v_oc = (K_B * temp_absorber/Q
                        * np.log(current_limit[ii] / dark_saturation_current))

                if charge_collection_method:
                    L_E = 350E-4
                    S = 80
                    THICKNESS = 350E-4
                    THICKNESS_N = 100E-7
                    THICKNESS_P = THICKNESS-THICKNESS_N
                    N_Z = 1000
                    z = np.linspace(0, THICKNESS, N_Z)
                    G = np.zeros(np.shape(z))
                    dz = z[1]-z[0]
                    for zz in range(N_Z):
                        G[zz] = np.sum(ALPHA_SI*J_photon
                                       *np.exp(-ALPHA_SI*z[zz])*dlabda,0)/10**4
                    CP = 1/(np.cosh((THICKNESS_N-z)/L_E)
                            + np.sinh((THICKNESS_N-z)/L_E)*(np.sinh(z/L_E)
                            + S*L_E*np.cosh(z/L_E))/(np.cosh(z/L_E)
                            + S*L_E*np.sinh(z/L_E)))
```

```
                    CP_2 = 1/(np.cosh((THICKNESS_P-z)/L_E)
                              + np.sinh((THICKNESS_P-z)/L_E)*(np.sinh(z/L_E)
                              + S*L_E*np.cosh(z/L_E))/(np.cosh(z/L_E)
                              + S*L_E*np.sinh(z/L_E)))
                    CP_2 = np.flipud((CP_2))
                    CP[z>THICKNESS_N] = 0
                    CP_2[z<THICKNESS_N] = 0
                    CP_tot = CP + CP_2
                    current_limit[ii] = Q*np.sum(G[0:N_Z]*CP_tot[0:N_Z]*dz)

                # Implementing the Tiedje-Yablonivich method for dark
                # saturation current determination
                b1 = (2/H**3*1**2/C**2*E_photon**2
                     *np.exp(-E_photon/K_B/temp_absorber))
                integral = np.sum(b1*ABSORBANCE*dE)
                dark_saturation_current = Q*np.pi*integral/10**4

                v_oc = (K_B * temp_absorber/Q
                        * np.log(current_limit[ii] / dark_saturation_current))








        else:
            ABSORBANCE = (LABDA_SPECTRUM*1E-9 < H*C/E_G[ii])
            REFL = 0
            v_oc = 0.7   #Initialize v_oc, to converge to it later
            E_photon = H*C/(LABDA_SPECTRUM*1E-9)

            dE = np.zeros(np.shape(E_photon))
            dE[0:-1] = np.abs(E_photon[0:-1] - E_photon[1:])
            dE[-1] = dE[-2]
            J_photon = POWER_SPECTRUM[0, :]/E_photon*(1-REFL)
            dlabda = np.zeros((len(LABDA_SPECTRUM),))
            dlabda[0:-1] = np.abs(LABDA_SPECTRUM[0:-1]
                            - LABDA_SPECTRUM[1:])
            dlabda[-1] = dlabda[-2]

            # Iterate a few time to converge to a solution
            for i in range(3):
                current_limit[ii], temp_absorber, input_power[kk], q_in = \
                calculate_flux_balance(INCOMING_SPECTRUM, E_G[ii],
                                       T_AIR[kk, 1], ABSORBANCE, T_ELECTROLYTE,
                                       v_oc)

                dark_saturation_current = (Q*A*2*K_B*temp_absorber/H**3/C**2
                                           * (E_G[ii]**2
                                              + 2*K_B*temp_absorber*E_G[ii]
                                              + 2*(K_B*temp_absorber)**2)
                                           * np.exp(-E_G[ii]/K_B/temp_absorber)
                                           / 10**4)

                v_oc = (K_B * temp_absorber/Q
                        * np.log(current_limit[ii] / dark_saturation_current))
                # Uncomment the next line if you want to fix the temperature
#                temp_absorber = T_ARRAY[kk]


        if TEMP_DEPENDENT_J0:
            J0_BV = J0_BV_ref*np.exp(-E_A/R/temp_absorber)
```

```
        iv_curve[:, ii, :, kk], overpotential = \
        calculate_iv_curve(current_limit[ii], v_oc, J0_BV, temp_absorber,
                           dark_saturation_current, R_SERIES, ALPHA)

        soc_correction[ii, :] = (R * temp_absorber / F
                                 * np.log(SOC[ii, :]**2/(1 - SOC[ii, :])**2))

    soc_correction[SOC >= 0.999999999] = 1000
    for jj in range(NUM_E_THERM):
        condition = numpy.matlib.repmat(E_THERM[jj] + soc_correction[:, jj],
                                        NUM_IV_POINTS, 1)
        condition = np.transpose(condition)
        sufficient_photovoltage = iv_curve[0, :, :, kk] > condition
        operating_current[:, jj] = (np.max(iv_curve[1, :, :, kk]
                                           * sufficient_photovoltage, 1))
        efficiency[:, jj, kk] = (operating_current[:, jj]
                                 * (E_THERM[jj] + soc_correction[:, jj])
                                 / input_power[kk]*100)
        output_power[:, jj, kk] = (operating_current[:, jj]
                                   * (E_THERM[jj]+soc_correction[:, jj])*1000)
        if DYNAMIC_SOC:
            SOC[:, jj] = (SOC[:, jj] + AREA_ABSORBER
                          * operating_current[:, jj]
                          * DT / CAPACITY)
            SOC[SOC >= 1] = 0.999999999


    dT_electrolyte = q_in/(RHO*VOLUME*C_ELECTROLYTE)
    # Equilibrate the electrolyte temperature to the morning air tempearature
    # if the day changes
    if REAL_SOLAR_DATA:
        if int(day_in_the_year[kk+1] - day_in_the_year[kk]) == 0:
            T_ELECTROLYTE = T_ELECTROLYTE + dT_electrolyte * DT
        elif int(day_in_the_year[kk+1] - day_in_the_year[kk]) == 1:
            T_ELECTROLYTE = T_AIR[kk+1, 1]
        else:
            print(int(day_in_the_year[kk+1] - day_in_the_year[kk]))
            T_ELECTROLYTE = T_AIR[kk+1, 1]




    output_temperature[kk] = temp_absorber
    output_temperature_electrolyte[kk] = T_ELECTROLYTE
    print("\r {}".format(np.round((kk+1)/NUM_TIME_STEPS * 100)), end="")
del ii, jj, kk
ELAPSED_TIME = time.time() - START_TIME
print('\n The elapsed time = ', ELAPSED_TIME)
test = np.squeeze(efficiency)
```

C.3 Fit tool

```
# -*- coding: utf-8 -*-
"""
Created on Tue May 14 09:16:21 2019

@author: Richard Faasse
```

```
"""
import scipy.optimize as opt
import time
import numpy as np
import matplotlib.pyplot as plt
from functions import butler_volmer
from physical_constants import Q, K_B
from model_settings import save_fit_progression
import sys

#sys.path.insert(0,’..\input_data’)
input_data_path = ’..\input_data\\’

#%% Load data
#exp_IV = np.load(’BPA_ferro.npy’)
#exp_IV = -exp_IV[1000:1620, :]

#exp_IV = np.transpose(np.load(’CV_20190514.npy’))
#exp_IV = np.load(’BPC_PtSi.npy’)
#exp_IV = np.load(’50SOC_SiC_lowSS.npy’)
#exp_IV = np.transpose(np.load(’CV_20180417_sheet3.npy’))

exp_IV = np.load(input_data_path + ’BPC_ferri.npy’)
exp_IV = exp_IV[200:1000, :]

exp_IV[:, 1] = exp_IV[:, 1]/1000

#plt.plot(exp_IV[:, 0], exp_IV[:, 1])
#plt.show()


#%%
if save_fit_progression:
    fit_progression = np.zeros((3000, 3))
    np.save(’fit_progression.npy’, fit_progression)

JLIM_ANODE = 0.1
JLIM_CATHODE = -0.03
temp_absorber = 300
V_oc = exp_IV[np.argmin(np.abs(exp_IV[:, 1])), 0]
current_limit = 0.04

def IV_error(x):
    """
    Description:
    ------------
    This function calculates error between experimental data and modeled curves
    using three parameters: ALPHA, R_SERIES and J0_BV, taken together in the
    array x

    INPUTS:
    ------------
    x: array (3,)
        Array containing ALPHA, R_SERIES and J0_BV as variable parameters

    OUTPUTS:
    ----------
    error_IV: float
        average squared error between the experimental data and modeled curve
    """


    ALPHA = x[0]
    R_SERIES = x[1]
    J0_BV = 10**(x[2])
```

```
    j_fit = np.linspace(JLIM_CATHODE+0.00001,
                        JLIM_ANODE-0.00001, 1000)
    overpotential = np.zeros((np.size(j_fit, 0), ))
    error_small_enough = np.zeros((np.size(j_fit, 0)), dtype=bool)
    error = np.zeros((np.size(j_fit, 0), ))
    j_D = current_limit + j_fit


    # Find the overpotential as function of current density
    for ii in range(np.size(j_fit, 0)):
        sol = opt.root_scalar(butler_volmer, args=(J0_BV, temp_absorber,
                                                   j_fit[ii], ALPHA)
                              , bracket=[-10, 10], x0=0, method=’brenth’)
        overpotential[ii] = sol.root

        # Check whether overpotential solution is correct:
        error[ii] = np.abs(butler_volmer(overpotential[ii], J0_BV,
                                         temp_absorber, j_fit[ii], ALPHA))

        error_small_enough[ii] = error[ii] < 10**(-8)

    V_D = V_oc + K_B*temp_absorber/Q*np.log((j_D)/(current_limit))
    PV = V_D + overpotential + j_fit*R_SERIES

    j_interp = np.interp(exp_IV[:, 0], PV[error_small_enough == 1],
                         j_fit[error_small_enough == 1])
    j_interp[np.isnan(j_interp)] = -current_limit


    error_IV = (np.sum(np.abs(np.power(1000*exp_IV[:, 1] - 1000*j_interp, 2))))

    print(’total␣squared␣error␣=␣’, str.format(’{0:.2f}’, np.sqrt(error_IV)),
          ’mA/cm2,␣ALPHA␣=␣’, str.format(’{0:.2f}’, ALPHA),
          ’,␣R_SERIES␣=␣’, str.format(’{0:.1f}’, R_SERIES),
          ’,␣J0_BV␣=␣10␣^␣’, str.format(’{0:.1f}’, x[2]))

    if save_fit_progression:
        fit_progression = np.load(’fit_progression.npy’)
        fit_progression[np.sum(fit_progression[:, 0] > 0), :] = \
                                            np.array((ALPHA, R_SERIES, J0_BV))
        np.save(’fit_progression.npy’, fit_progression)
    return error_IV

START_TIME = time.time()


bounds = [(0.1, 0.9), (0, 40), (-8, 0.5)]
x = opt.dual_annealing(IV_error, bounds, initial_temp=100, maxfun = 100)
ELAPSED_TIME = time.time() - START_TIME

fitted_parameters = x.x


#%% Plot the modeled and experimental curves

ALPHA = fitted_parameters[0]
R_SERIES = fitted_parameters[1]
J0_BV = 10**(fitted_parameters[2])


j_fit = np.linspace(JLIM_CATHODE+0.00001,
                    JLIM_ANODE-0.00001, 1000)
overpotential = np.zeros((np.size(j_fit, 0), ))
error_small_enough = np.zeros((np.size(j_fit, 0)), dtype=bool)
error = np.zeros((np.size(j_fit, 0), ))
j_D = current_limit + j_fit
```

```
# Find the overpotential as function of current density
for ii in range(np.size(j_fit, 0)):
    sol = opt.root_scalar(butler_volmer, args=(J0_BV, temp_absorber,
                                                j_fit[ii], ALPHA)
                          , bracket=[-10, 10], x0=0, method='brenth')
    overpotential[ii] = sol.root

    # Check whether overpotential solution is correct:
    error[ii] = np.abs(butler_volmer(overpotential[ii], J0_BV, temp_absorber,
                                     j_fit[ii], ALPHA))

    error_small_enough[ii] = error[ii] < 10**(-8)

V_D = V_oc + K_B*temp_absorber/Q*np.log((j_D)/(current_limit))
PV = V_D + overpotential + j_fit*R_SERIES

j_interp = np.interp(exp_IV[:, 0], PV[error_small_enough == 1],
                     j_fit[error_small_enough == 1])
j_interp[np.isnan(j_interp)] = -current_limit



error_IV = np.sum(np.abs(exp_IV[:, 1] - j_interp))/np.size(exp_IV, 0)*1000
print('The␣elapsed␣time␣=␣', ELAPSED_TIME)
print('average␣error␣(mA/cm2)␣=␣', error_IV)
print('Alpha␣=␣', ALPHA)
print('R_SERIES␣=␣', R_SERIES)
print('J0_BV␣=␣', J0_BV )
print('V_oc␣=␣', abs(V_oc), 'vs␣NHE')
fig,ax = plt.subplots()

plt.plot(exp_IV[:, 0],exp_IV[:, 1]*1000, label = 'experimental␣data',
         linewidth = 2, color = (0,166/255,214/255))
plt.plot(exp_IV[:,0],j_interp*1000, linestyle = '--', label = 'fit', \
         color = 'black', linewidth = 2)

ax.spines['bottom'].set_position('zero')

plt.legend()
plt.ylabel('Current␣density␣(mA/cm$^2$)')
plt.xlabel('V␣vs␣NHE␣(V)')
plt.tight_layout()
plt.rcParams.update({'font.size': 14})
plt.savefig('fit_BPC_PEC.svg', format='svg')
plt.show()
```

C.4 functions

```
# -*- coding: utf-8 -*-
"""
Created on Mon May  6 13:35:23 2019

@author: Richard Faasse
"""
import scipy.optimize as opt
import numpy as np
from device_parameters import C_AUGER, N_I, THICKNESS, H_AIR, H_ELECTROLYTE, \
H_ELECTROLYTE_AIR, AREA_ABSORBER
from physical_constants import Q, H, K_B, C, SIGMA
from model_settings import REAL_ABSORBER_DATA, AUGER_RECOMBINATION, \
                           NUM_IV_POINTS
from losses import JLIM_ANODE, JLIM_CATHODE
```

```
def calculate_flux_balance(INCOMING_SPECTRUM, E_G, T_AIR,
                           ABSORBANCE, T_ELECTROLYTE, v_oc):
    """
    Description:
    ------------
    This function solves the flux balance based on the incoming solar
    radiation, black-body emission and convective heat transferto calculate
    the limiting photo-current, the temperature of the photo-absorber and the
    total input power of the incoming spectrum

    INPUTS:
    ----------
    INCOMING_SPECTRUM: array (N,2)
        Contains the incoming power spectrum in [:,1]
        and corresponding wavelengths in [:,0]
    E_G: float
        Bandgap of the photo-absorber (J)
    T_AIR: float
        Temperature of the surrounding air
    ABSORBANCE: array (N,)
        absorbance (number between 0 and 1) for every wavelength
    T_ELECTROLYTE:
        Electrolyte temperature


    OUTPUTS:
    --------
    current_limit: float
        limiting photo-current produced by the photoabsorber with bandgap E_G
        under the influence of the incoming radiation stored in
        INCOMING_SPECTRUM
    temp_absorber: float
        Temperature of the photo-absorber, calculated using the heat balance
    input_power: float
        Total input power of the incoming solar spectrum
    q_in: float
        Incoming solar flux for the electrolyte
    """
    labda_g = H*C/E_G
    labda = INCOMING_SPECTRUM[:, 0]*1E-9
    E_photon = H*C/labda
    J_photon = INCOMING_SPECTRUM[:, 1]/E_photon
    dlabda = np.zeros((len(INCOMING_SPECTRUM),))
    dlabda[0:-1] = np.abs(INCOMING_SPECTRUM[0:-1, 0]
                          - INCOMING_SPECTRUM[1:, 0])
    dlabda[-1] = dlabda[-2]
    E_dissipated = E_photon-v_oc*Q

    if REAL_ABSORBER_DATA:
        current_limit = np.sum(J_photon * ABSORBANCE * dlabda) * Q / 10**4
        solar_heat_flux = np.sum(E_dissipated * J_photon
                                 * ABSORBANCE * dlabda) / 10**4
    elif not REAL_ABSORBER_DATA:
        current_limit = np.sum(J_photon[labda <= labda_g]
                               * dlabda[labda <= labda_g]) * Q / 10**4
        solar_heat_flux = np.sum(E_dissipated * J_photon
                                 * (labda <= labda_g) * dlabda) / 10**4

    sol = opt.root_scalar(heat_balance, args=(solar_heat_flux, T_AIR,
                                              T_ELECTROLYTE),
                          bracket=[200, 600], x0=300, method='brenth')
    temp_absorber = sol.root

    q_in = AREA_ABSORBER * (SIGMA*(temp_absorber**4-T_ELECTROLYTE**4)
```

```
                            + H_ELECTROLYTE_AIR*(T_AIR - T_ELECTROLYTE)
                            + H_ELECTROLYTE*(temp_absorber -
                                             T_ELECTROLYTE))/10**4



    input_power = np.sum(E_photon*dlabda*J_photon)/10**4

    return current_limit, temp_absorber, input_power, q_in



def heat_balance(temp_absorber, solar_heat_flux, T_AIR, T_ELECTROLYTE):
    """
    Description:
    ------------
    This function describes the heat balance, using the incoming solar heat
    flux, as calculated in calculate_heat_balance and the respective
    temperatures of the absorber, electrolyte and ambient air and the
    convective heat transfer coefficients (H_AIR/ELECTROLYTE etc)

    INPUTS:
    ----------
    temp_absorber: float
        Temperature of the photo-absorber
    solar_heat_flux: float
        the disspated incoming solar radiation
    T_AIR: float
        Temperature of the surrounding air
    T_ELECTROLYTE:
        Electrolyte temperature


    OUTPUTS:
    --------
    y: float
        output of the function that should be 0 in the assumed steady state
        heat balance, such that it is used for root finding in the function
        calculate_heat_balance
    """
    y = (-solar_heat_flux + SIGMA*(temp_absorber**4-T_AIR**4)/10**4
         + H_AIR*(temp_absorber-T_AIR)/10**4
         + H_ELECTROLYTE*(temp_absorber-T_ELECTROLYTE)/10**4)
    return y
def butler_volmer(overpotential, J0_BV, temp_absorber, j_fit, ALPHA):
    """
    Description:
    ------------
    This function describes the heat balance, using the incoming solar heat
    flux, as calculated in calculate_heat_balance and the respective
    temperatures of the absorber, electrolyte and ambient air and the
    convective heat transfer coefficients (H_AIR/ELECTROLYTE etc)

    INPUTS:
    ------------
    overpotential: float
        overpotential, which needs to be solved
    J0_BV: float
        Exchange current density as defined in the butler-volmer equation
    temp_absorber: float
        Temperature of the photo-absorber
    j_fit: float
        current density at which we want to solve for V
    ALPHA: float
        asymmetry factor from the butler-volmer equation
```

```
    OUTPUTS:
    --------
    y: float
        output of the function that should be 0 to solve for the overpotential,
        such that it is used for root finding in the function
        calculate_iv_curve
    """
    y = J0_BV*(np.exp(ALPHA*Q*overpotential/K_B/temp_absorber)
               - np.exp(-(1-ALPHA)*Q*overpotential/K_B/temp_absorber)) - j_fit
#    y = J0_BV*((1-j_fit/JLIM_ANODE)
#              * np.exp(ALPHA * Q * overpotential / K_B / temp_absorber)
#              - (1-j_fit/JLIM_CATHODE)
#              * np.exp(-(1-ALPHA)*Q*overpotential/K_B/temp_absorber)) - j_fit
    return y


def IV_with_Auger(V, dark_saturation_current, current_limit, j, temp_absorber):
    """
    Description:
    ------------
    This function describes the heat balance, using the incoming solar heat
    flux, as calculated in calculate_heat_balance and the respective
    temperatures of the absorber, electrolyte and ambient air and the
    convective heat transfer coefficients (H_AIR/ELECTROLYTE etc)

    INPUTS:
    ------------
    V: float
        voltage, which needs to be solved
    dark_saturation_current: float
        dark saturation current of the photo-absober
    current_limit: float
        Saturation current of the photo-diode
    j: float
        current density at which we want to solve for V
    temp_absorber: float
        Temperature of the photo-absorber

    OUTPUTS:
    --------
    y: float
        output of the function that should be 0 to solve for the voltage,
        such that it is used for root finding in the function
        calculate_iv_curve
    """
    x = V*Q/K_B/temp_absorber
    y = (- dark_saturation_current*np.exp(x)
         - Q*THICKNESS*C_AUGER*N_I**3*np.exp(3*x/2) + current_limit - j)
    return y


def calculate_iv_curve(current_limit, v_oc, J0_BV, temp_absorber,
                       dark_saturation_current, R_SERIES, ALPHA):
    """
    Description:
    ------------
    This function calculates the IV-curve of the PEC-flow battery, using
    various loss inputs and device parameters

    INPUTS:
    ------------
    current_limit: float
        Saturation current of the photo-diode
    v_oc: float
        open circuit voltage as calculated
```

```
    J0_BV: float
        Exchange current density as defined in the butler-volmer equation
    temp_absorber: float
        Temperature of the photo-absorber
    dark_saturation_current: float
        dark saturation current of the photo-absober
    R_SERIES: float
        Total series resistance of the SRFB
    ALPHA: float
        Asymmetry factor in the butler volmer equation.
    ----------

    OUTPUTS:
    iv_curve: array (2, NUM_IV_POINTS)
        current-voltage characteristic, current is found in iv_curve[1, :],
        voltage is found in iv_curve[0, :]
    overpotential: array (NUM_IV_POINTS,)
        kinetic overpotential as a function of current (the current is found
        in j_fit, or iv_curve[1, :])
    """

    j_fit = -np.linspace(-0*0.999999*current_limit,
                         current_limit, NUM_IV_POINTS)
#    j_fit = -np.linspace(0.9999*JLIM_CATHODE,
#                         0.9999*JLIM_ANODE, NUM_IV_POINTS)
    j_D = current_limit + j_fit
    V_D = np.zeros(np.shape(j_fit))
    j_D[j_D == 0] = 1E-15
    if ALPHA == 0.5:
        overpotential = 2*K_B*temp_absorber/Q*np.arcsinh(j_fit/2/J0_BV)
    else:
        overpotential = np.zeros((np.size(j_fit, 0), ))
        for ii in range(np.size(j_fit, 0)):
            sol = opt.root_scalar(butler_volmer, args=(J0_BV, temp_absorber,
                                                       j_fit[ii], ALPHA),
                                  bracket=[-10, 10], x0=0, method='brenth')
            overpotential[ii] = sol.root
    if AUGER_RECOMBINATION:
        for ii in range(np.size(j_fit, 0)):
            sol = opt.root_scalar(IV_with_Auger,
                                  args=(dark_saturation_current,
                                        current_limit, -j_fit[ii],
                                        temp_absorber),
                                  bracket=[-1000, 1000], x0=0, method='brenth')
            V_D[ii] = sol.root
    else:
        V_D = v_oc + K_B*temp_absorber/Q*np.log((j_D)/(current_limit))

    PV = V_D + overpotential + j_fit*R_SERIES
#    j_fit[np.isnan(PV)] = -current_limit
    j_fit = np.abs(j_fit)
    iv_curve = np.squeeze(np.array([[PV], [j_fit]]))
    return iv_curve, overpotential
```

C.5 Data processing

```
# -*- coding: utf-8 -*-
"""
Created on Fri Sep  6 09:39:50 2019

@author: Richard

general_data_processing can be used to visualize many of the data created by
simulation.py. Therefore, this file can only be run, when first simulation.py
```

```
is used and created the data.
"""
import numpy as np
import matplotlib.pyplot as plt
from matplotlib import cm
from matplotlib.colors import ListedColormap, LinearSegmentedColormap
from mpl_toolkits.axes_grid1.inset_locator import inset_axes
import matplotlib.colors
from matplotlib import cm
from matplotlib.colors import ListedColormap, LinearSegmentedColormap
from mpl_toolkits.axes_grid1 import make_axes_locatable
from matplotlib.animation import FuncAnimation
import matplotlib.animation as animation
import matplotlib.colors

#%%
# ==============================================================================
# Plot a single contour plot
# ==============================================================================
def plot_contour(x, y, f_xy):
    # Editing the colormap
    cmap = plt.cm.viridis
    cmaplist = [cmap(i) for i in range(cmap.N)]
    cmaplist[0:50] = []
    cmap = matplotlib.colors.LinearSegmentedColormap.from_list('mcm', cmaplist,
                                                                cmap.N)
    fig, ax = plt.subplots(figsize=(10, 7))
    div = make_axes_locatable(ax)
    cax = div.append_axes('right', '5%', '5%')


    contour_opts = {'lw': 2, 'colors':'k'}
    ax.contour(x, y, np.transpose(f_xy),
                     **contour_opts)
    mappable = ax.contourf(x, y, np.transpose(f_xy),
                           vmin=0, vmax=np.max(f_xy), cmap=cmap)

    cax.cla()

    fig.colorbar(mappable, cax = cax)
    plt.rcParams.update({'font.size': 20})
    ax.set_xlabel('Bandgap␣energy␣(eV)')
    ax.set_ylabel('Thermodynamic␣potential␣(V)')
    plt.draw()

plot_contour(E_G/Q, E_THERM, efficiency[:, :, 0])

# ==============================================================================
#%% Plot a (parameter-dependent) IV-curve, make sure you only have one E_G
# ==============================================================================
cmap = cm.get_cmap('RdBu', NUM_TIME_STEPS)
fig = plt.figure()
ax = fig.add_subplot(111)
for i in range(NUM_TIME_STEPS):
    plt.plot(np.squeeze(iv_curve[0, :, :, i]),
             np.squeeze(iv_curve[1, :, :, i])*1000,
             label='IV␣curve', color = cmap(i),lw = 3)

plt.xlim((0,1))
plt.ylim((0,45))
plt.rcParams.update({'font.size': 12})
plt.xlabel('Voltage␣(V)')
plt.ylabel('Current␣density␣(mA/cm$^2$)')
plt.tight_layout()
for axis in ['top','bottom','left','right']:
  ax.spines[axis].set_linewidth(2)
```

```
ax.xaxis.set_tick_params(width=2)
ax.yaxis.set_tick_params(width=2)
plt.show()


# =============================================================================
#%% Plot a (parameter-dependent) STC vs E_THERM graph,
# make sure you only have one E_G
# =============================================================================
cmap = cm.get_cmap('Blues', NUM_TIME_STEPS)
fig = plt.figure()
ax = fig.add_subplot(111)
for i in range(NUM_TIME_STEPS):
    plt.plot(E_THERM,
             np.squeeze(efficiency[:, :, i]),
             label='IV␣curve', color = cmap(i),lw = 3)

plt.xlim((0,0.7))
plt.ylim((0,30))
plt.rcParams.update({'font.size': 12})
plt.xlabel('Voltage␣(V)')
plt.ylabel('Current␣density␣(mA/cm$^2$)')
plt.tight_layout()
for axis in ['top','bottom','left','right']:
  ax.spines[axis].set_linewidth(2)
ax.xaxis.set_tick_params(width=2)
ax.yaxis.set_tick_params(width=2)
plt.show()

# =============================================================================
#%% Plot a (parameter-dependent) STC vs Daytime graph,
# make sure you only have one E_G and one E_THERM
# =============================================================================
plt.plot(DAYTIME, np.squeeze(output_power))

#plt.xlim((0,0.7))
#plt.ylim((0,30))
plt.rcParams.update({'font.size': 16})
plt.xlabel('Time␣of␣day␣(h)')
plt.ylabel('Output␣power␣(mW/cm$^2$)')
plt.tight_layout()
for axis in ['top','bottom','left','right']:
  ax.spines[axis].set_linewidth(2)
ax.xaxis.set_tick_params(width=2)
ax.yaxis.set_tick_params(width=2)
plt.show()

#%%
# =============================================================================
# Animate a parameter/time-dependent iv_curve (make sure to use only one E_G)
# If you want to plot multiple bandgaps, the contour animator below is recom-
# mended
# =============================================================================
fig, ax = plt.subplots(figsize=(8, 6))
plt.xlabel('Voltage␣vs␣NHE␣(V)')
plt.ylabel('j␣(mA/cm$^2$)')
plt.grid()

ax.set(ylim=(-20,20))
ax.set(xlim=(0.5, 1.8))
ax.spines['bottom'].set_position('zero')
plt.rcParams.update({'font.size': 16})
plt.tight_layout()

V = np.squeeze(iv_curve[0, :, :, 0])
line = ax.plot(np.squeeze(iv_curve[0,:,:,0]),
```

```
               1000*np.squeeze(iv_curve[1,:,:,0]), lw=3)[0]

plt.legend()
def animate(i):
    line.set_ydata(1000*np.squeeze(iv_curve[1,:,:,i]))
    line.set_xdata(np.squeeze(iv_curve[0,:,:,i]))
    print("\r␣{}".format(np.round((i+1)/NUM_TIME_STEPS*100,decimals=2)),
          '%', end="")


    plt.rcParams.update({'font.size': 16})

anim = FuncAnimation(fig, animate, interval=100, frames = NUM_TIME_STEPS)
anim.save('tmp.mp4', writer='ffmpeg', fps = 20, dpi = 300)
plt.draw()
plt.show()




#%%
# ===========================================================================
# Animate a parameter/time-dependent contourplot. If you want to animate the
# output power instead of the efficiency, replace efficiency with output_power
# ===========================================================================
fig, ax = plt.subplots(figsize=(10, 7))
div = make_axes_locatable(ax)
cax = div.append_axes('right', '5%', '5%')
# Change the levels to your own convenience for clearer contour-plots
contour_opts = {'levels': np.linspace(0, 36, 13), 'lw': 2, 'colors':'k'}
contour_opts2 = {'levels': np.linspace(0, 36, 13)}

plt.rcParams.update({'font.size': 14})
plt.xlabel('Bandgap␣energy␣(eV)')
plt.ylabel('Thermodynamic␣potential␣(V)')

START_TIME = time.time()
cmap = plt.cm.viridis
cmaplist = [cmap(i) for i in range(cmap.N)]
cmaplist[0:50] = []
cmap = matplotlib.colors.LinearSegmentedColormap.from_list('mcm',
                                                           cmaplist, cmap.N)
def animate(i):
     ax.collections = []
     cax2 = ax.contour(E_G/Q, E_THERM,
                       np.transpose(efficiency[:, :, i]), **contour_opts)

     ax.set_xlabel('Bandgap␣energy␣(eV)')
     ax.set_ylabel('Thermodynamic␣potential␣(V)')
     mappable = ax.contourf(E_G/Q, E_THERM,
                            np.transpose(efficiency[:, :, i]), vmin=0,
                            vmax=np.max(efficiency), cmap=cmap,
                            **contour_opts2)
     cax.cla()
     fig.colorbar(mappable, cax = cax)

     print("\r␣{}".format(np.round((i)/NUM_TIME_STEPS
                          * 100,decimals=2)),'%', end="")


anim = FuncAnimation(fig, animate, interval=100, frames=NUM_TIME_STEPS)
anim.save('temporary.mp4', writer='ffmpeg', fps = 20, dpi = 300)
ELAPSED_TIME = time.time() - START_TIME
plt.rcParams.update({'font.size': 14})
print('\n␣Done!␣The␣elapsed␣time␣=␣', ELAPSED_TIME)
```